Title
Mercury Detection with Gold Nanoparticles

Author
Crosby, Jeffrey

Publication Date
2013

Peer reviewed|Thesis/dissertation

Mercury Detection with Gold Nanoparticles: Investigating Fundamental Phenomena and Expanding Applications

By

Jeffrey Scott Crosby

A dissertation submitted in partial satisfaction of the

requirements for the degree of

Doctor of Philosophy

in

Engineering - Mechanical Engineering

in the

Graduate Division

of the

University of California, Berkeley

Committee in charge:

Professor Catherine P. Koshland, Co-Chair
Professor Chris Dames, Co-Chair
Professor Carlos Fernandez-Pello
Professor Costas P. Grigoropoulos
Professor S. Katharine Hammond

Spring 2013

Abstract

Mercury Detection with Gold Nanoparticles:
Investigating Fundamental Phenomena and Expanding Applications

by

Jeffrey Scott Crosby

Doctor of Philosophy in Engineering-Mechanical Engineering

University of California, Berkeley

Professor Catherine Koshland, Co-Chair

Professor Chris Dames, Co-Chair

Mercury is a pollutant of grave concern with well documented neurological and developmental health impacts. Better sensing methodology would improve detection and control of mercury and thus reduce its health burden. Gold nanoparticles provide a sensing medium with potential advantages in sensitivity, selectivity, robustness, and cost over established techniques. Mercury readily adsorbs onto the surface of the gold changing the localized surface plasmon resonance which is measured as a shift in the peak optical absorbance wavelength. This shift is dependent on the mercury concentration and predictable with classical electromagnetism.

This work investigates some of the fundamental relationships driving sensor response. The effects of mass transfer and surface kinetics on mercury/gold nanoparticle adsorption are determined with analytical models and experimental results based on impinging flow geometry. To decouple mass transfer and surface kinetics adsorption, electrical analogy models are constructed and fit to the experimental data. The models can account for variations in flow conditions and surface coatings on the nanoparticles. These models are generalizable to other systems.

Results from these fundamental investigations are used to improve and extend sensor performance. The time response or collection efficiency is optimized depending on system requirements. Using the knowledge gained, the applicability of gold nanoparticle mercury sensors is extended to a fiber optic based system and aqueous detection. Nanorods deposited on the surface of a fiber optic cable have a linear response with concentration and are able to detect mercury down to 1.0 $\mu g/m^3$. The modification of an established oxidation/reduction scheme for use with the sensor allows for the detection of ionic and organic mercury from water samples which ordinarily would not be reactive with gold nanoparticles. The aqueous sensor was able to detect mercury below the EPA's drinking water limit.

This work is dedicated to my mother and father.
The best teachers I ever had.

Table of Contents

1. Introduction on mercury and noble metal nanoparticle sensors 1
1.1 Health effects of mercury 1
1.1.1Historical background of mercury toxicity 1
1.1.2 Mercury's physiological effects 2
1.1.3 Epidemiological basis for dose-response 2
1.1.4 Mercury exposure assessment 5
1.2 Mercury cycle and fate and transport 5
1.2.1 Mercury sources 5
1.2.2 The mercury cycle 7
1.2.3 Bioaccumulation of methylmercury 9
1.3 Regulation and detection of mercury 11
1.3.1 Regulatory background 11
1.3.2 Current mercury detection methods 12
1.4 Gold nanoparticles as mercury sensors 13
1.4.1 Noble metal nanoparticles background 13
1.4.2 Noble metal nanoparticle synthesis and assembly 14
1.4.3 Nanoparticles as sensors 16
1.4.4 Interaction of mercury with gold nanoparticles 17
1.4.5 Prior gold nanoparticle mercury sensors 21
2. Mass transfer, surface kinetics and thermodynamics of mercury adsorption on gold nanoparticles 24
2.1 Background 24
2.1.1 Mass transfer and gas sensors 24
2.1.2 Adsorption 31
2.2 Adsorption of mercury on gold nanospheres 42
2.2.1 Experimental methods 42
2.2.2 Results 45
2.2.3 Application of adsorption models to data 49
2.3 Combined mass transfer and surface kinetics model 52
2.3.1 Theoretical background (RC circuit analogy) 52
2.3.2 Applying the RC model to mercury-gold nanosphere data 56
2.3.3 RC model results 58

2.3.4 Conclusion 62
3. Detection of air borne elemental mercury concentration with gold nanorod decorated fiber optic sensors 65
3.1 Background 65
3.1.1 Fiber optic based sensing 65
3.1.2 Evanescent waves 68
3.1.3 Application of the Mie and Gans solutions to gold nanoparticles 70
3.2 Experimental procedure 75
3.2.1 Materials and methods: 75
3.2.2 Fiber optic sensor results 78
3.3 Discussion: temperature effects and selectivity of fiber optic sensors 82
3.4 Concluding remarks on fiber optic sensors 83
4. Detection of mercury in aqueous samples with gold nanoparticles 85
4.1 Introduction 85
4.1.1 Motivation 85
4.1.2 Challenges of mercury measurement in aquatic environments 85
4.1.3 Current measurement techniques 87
4.2 Aqueous mercury detection utilizing gold nanoparticles 88
4.2.1 Experimental design 88
4.2.2 Results 91
4.3 Discussion of aqueous mercury detection 98
4.3.1 Sensor improvement via mass transfer optimization 99
4.3.2 Sensor improvement via a continuous flow system 103
4.3.3 Extension of results to solid samples 104
4.4 Conclusions on aqueous mercury detection with gold nanoparticles 105
5. Conclusion 106
References 110
Appendix A Spectral shifts of fiber optic sensors 125
Appendix B Matlab functions for processing absorbance data and fitting kinetic/diffusion models 127
Appendix B.1 Absorbance Processing Program 127
Appendix B.2 Function to apply a Langmuir Fit 133
Appendix B.3 Function for Sips/Freundlich Isotherm Fit 135

Appendix B.4 Function for First Order Fit 136
Appendix B.5 Second Order Fit Function 137
Appendix B.6 Nth Order Fit 138
Appendix B.7 Film Diffusion Fit Function 139
Appendix B.8 Double Exponential Fit Function 140
Appendix B.9 Elovich Model 142
Appendix B.10 Elovich Model Fit Function 143
Appendix B.11 Lorentz (Cauchy Distribution) Function Fit 144
Appendix C Matlab Functions for the Modeling of Optical Absorbance using Mie and Gans Dipole Approximations 145
Appendix C.1 Mie Dipole Approximation 145
Appendix C.2 Gans Dipole Approximation 146
Appendix C.3 Index of Refraction for Gold 148
Appendix C.4 Index of Refraction of Air using Ciddor Model 149
Appendix C.5 Mercury Index of Refraction 152
Appendix C.6 Index of Refraction for Silicon Dioxide 152
Appendix C.7 Drude Approximation for Size Confined Nanoparticles 153
Appendix D Mass transfer correlation Matlab functions 156
Appendix D.1 Impinging jet efficiency 156
Appendix D.2 Martin Correlation 156
Appendix D.3 Womac Correlation 157

Acknowledgements

This work would not have been possible without the kind help from many talented and dedicated people. I would like to thank my committee members, Professors Carlos Fernandez-Pello, Costas P Grigoropoulos, and S. Katherine Hammond, for their careful review and comments which improved the quality of this manuscript. In particular, I would like to thank my Co-Chair, Professor Chris Dames who in addition to reviewing this work graciously include me in his group. The challenging questions and insightful comments I received from him, and the other members of his group, helped me clarify many of the problems addressed in this work.

Many thanks to my labmate Jay James. He welcomed me into the lab, taught me a great deal, paved the way for much of this work with his own, and was always a source of encouragement, a keen sounding board, and full of anecdotes about Berkeley politics.

I would like to express my gratitude to the Department of Mechanical Engineering; I learned a great deal from the excellent faculty there and the always helpful staff knew exactly the best way to solve any problem. Additional thanks must go to the Superfund Research Program, whose support made most of this work possible.

Finally, none of this would be possible without the support of my research advisors Donald Lucas and Cathy Koshland. Always insightful and available, they taught me a great deal about how to conduct science, present ideas, and make an impact with research. Last but not least, they went over this dissertation with a fine toothed comb and made it a much stronger document.

1. Introduction on mercury and noble metal nanoparticle sensors

This section serves as a general introduction to the broad themes into which this dissertation fits, giving background and motivation for the work. It discusses the role mercury plays as a global pollutant, the major sources of anthropogenic and natural mercury, how mercury is transported in the environment with emphasis on the different forms that mercury can take, and finally the current state of detection technology. It subsequently provides background on the use of nanoparticles as a sensing mechanism, how their strong absorbance band can be tuned to the visible range, and how that absorbance band is sensitive to changes in the environment. An introduction to the analytical model of nanoparticles based on the Mie and Gans solution to Maxwell's equations is presented. The last section will discuss the strong interaction between gold and mercury, and previous work on mercury sensors

1.1 Health effects of mercury

Mercury is an element, number 80 on the periodic table. Mercury, in trace amounts, is ubiquitous on the planet, with several areas containing higher concentrations of the element, usually as the ore cinnabar (HgS) [1]. Since industrialization the concentration of mercury in the environment has increased. This increase is a concern as mercury has been linked to a variety of health effects, most notably neurological damage. The largest category of the anthropogenic mercury results from the combustion of fossil fuels [2]. As a pollutant mercury primarily takes three forms: elemental mercury, ionic mercury, and organic or methylmercury. It can also exist bound up as particulate mercury associated with many other chemical and biological species.

1.1.1 Historical background of mercury toxicity

Mercury, acting as a neurotoxin, has a long history of interaction with human populations. Historical reports suggest mercury compounds in cosmetics and medicines as a cause of mortality in ancient Egyptian, Roman, and Chinese societies[1] [4][5]. Occupational exposures have a similarly long history; of particular note were the illness experienced by feltmakers employed in the hat industry of seventeenth and eighteenth century Europe [4], and the short life expectancy of convicts and slaves employed in large mercury mines in Spain and its New World colonies [6].

While these observations must have suggested a link between mercury exposure and health outcomes, it was not recognized until a series of lab accidents in the 1800's demonstrated the toxicity of methylmercury [7] to portions of the scientific community. This recognition did not prevent a series of industrial exposures in the 1940's causing health problems. Limits, mostly voluntary, were then placed on occupational exposures to mercury compounds [8]. Eventually two large environmental disasters led to widespread concern and strong limits being placed on methylmercury releases. The first was in Minamata Bay, Japan. From 1956 to 1968 methylmercury releases from a chemical plant caused severe neurological and developmental impairment of local residents who consumed seafood from the polluted bay. Many were

[1] This practice has continued in some parts of the world, see [3].

infected through their pregnant mothers [9]. The second was the death of 459 people, and the impairment of possibly thousands more, in Iraq in 1971 after the inadvertent consumption of seed grain which had been treated with a methylmercury fungicide [10][11].

1.1.2 Mercury's physiological effects

Further research, spurred on in part by these environmental health disasters, investigated the method of action by which mercury acts as a neurotoxin. There are still uncertainties about the exact cause of mercury toxicity, but the broader physiological effects are established. While generally similar, the exact method of action depends on the form of mercury and the pathway through which it is introduced to the body. Elemental mercury, most often breathed in as a vapor, traverses the alveoli membrane into the blood. Most of this mercury is oxidized to ionic mercury, bound in proteins and eventually secreted. The conversion of elemental mercury to ionic is mediated by the catalase-hydrogen peroxide and the exact rate is variable depending on cell chemistry [6]. If exposures are high, sufficient quantities can reach the blood brain barrier and cause impairment. Ionic mercury, usually ingested in drinking water, tends to be bound in proteins, and while capable of damage to other organ systems; it tends not to affect the central nervous system[12]. Methylmercury is particularly pernicious due to its lipid solubility and the high affinity for thiol (SH-) groups. Thiol groups are found in a variety of amino acids. Thus methylmercury easily passes the blood brain barrier and creates disruptions in cell activity in the central nervous system [6][13].

Methylmercury can also cross the placental barrier causing similar disruptions in the developing brain. Fetal exposure can be fatal at high doses. Lower levels led to: diminished cognitive capacity, cerebral palsy, and psychomotor disorders [13]. The link between higher concentrations of mercury and adverse health outcomes has been clearly established both by the tragic environmental exposures mentioned and laboratory experiments. As with most environmental pollutants, health effects are difficult to determine at low to moderate exposure levels.

1.1.3 Epidemiological basis for dose-response

Dose-response work has focused on prenatal exposures and subsequent neurological development of the fetus, as the developing nervous system is keenly susceptible to lasting damage from low mercury concentrations [14]. Three large longitudinal cohort studies were conducted to quantify the dose-response. The studies are broadly similar. In each, a population is chosen based on its potentially elevated exposure level. Mothers enlisted in the study are tested for mercury levels either in maternal blood, maternal hair, or umbilical cord blood. The children are then followed and given standard tests at specific development milestones. Island populations are ideal, as they tend to consume higher levels of marine protein, a key pathway for human exposure, and are often easy to track for the follow up studies. The three large cohort studies were conducted in New Zealand, the Seychelles, and the Faroe Islands [15].

The New Zealand study found an association between maternal hair-mercury levels and offspring's IQ and psychomotor skills at 6 and 7 years of age, though only after excluding a particularly high exposure case [16]. The child in the high exposure case (86 mg/kg, four times any other maternal hair-mercury level) did not show diminished performance on the psychological and scholastic tests administered. If this case is included in the regression analysis, there is no correlation evident between maternal hair-mercury levels and development. It is only after the case is excluded from the analysis that a positive correlation is indicated. Despite this positive correlation, this study is often omitted when regulators are deciding on limits for mercury exposures due to questions about the population selection and the limited external scrutiny the data received [15][17].

The Seychelles and Faroe Islands studies are the two longitudinal cohort studies most often cited in evaluating methylmercury health effects [15], both for their rigor and sample size. However the two studies present contradictory results. The Faroe Island study found a correlation between performance on certain benchmark developmental performance tests and maternal mercury-hair concentration, at levels generally thought to be in the safe range of 10-20 μg/g [18]. The Seychelles Island study found very limited associated between development endpoints and mercury exposure, and concluded there is not a neurodevelopment risk from low concentrations of methylmercury due to reasonable fish consumption [15][19].

Various explanations have been offered for the difference in findings between the Faroe Islands and the Seychelles cohorts. Researchers have discussed additional exposure to polychlorinated biphenyls (PCBs) in the Faroe Island group, perhaps exacerbating mercury effects [17]. An attempt to control for PCB exposure in the cohort did not show correlation with developmental endpoints [18]. The cultural appropriateness of the testing in the Seychelles Islands has been questioned, as the tests were originally translated from American English [20]. Subsequent investigations in the cohort addressed some of these testing concerns [19]. Several research studies, including toxicological investigations on rats, suggest that the affinity of mercury for selenium, another heavy metal, may have offered some protection from the health impacts of mercury [21][22]. However, an epidemiological follow up on the Faroe Island cohort did not find evidence of a protective benefit from selenium [23]. Perhaps the most satisfying explanation is simply the difference between the two populations and their environments. The subarctic Faroese receive most of their mercury from pilot whale consumption. The pilot whales have a higher mercury level and accumulate other pollutants, such as the PCB's. The tropical Seychellois consume fish which have a lower mercury concentration and lower overall pollution burden [15]. This highlights the difficulty in sorting out the exact relationship between subtle health outcomes and low level exposures, and the myriad of confounding variables that can affect epidemiological studies. These difficulties should not diminish the possible health implications from mercury consumption.

Several other smaller studies have also shown an effect between prenatal mercury exposure and developmental outcomes in a variety of settings and exposure routes. McKeown-Eyssen et al. [24] examined exposure relationships of Native American populations in Northern Canada and found significant association between neurological deficits and methylmercury levels in

maternal hair. Interestingly, the effect was only seen in boys. Studies of children in a Peruvian fishing village did not find a relationship between exposure and outcomes, but the population was relatively small (131 pairs) [25][26]. Murata et al. [27][28] found no link between neurodevelopmental effects and maternal hair-mercury concentrations up to 54.5 ppm (54.5 mg/kg); they did find some neurophysiological changes. Cordier et al. [29] found various developmental effects correlated with mercury hair levels for the children. The developmental effects included deficits in reflexes, leg coordination, and visual spatial organization. There were difficulties with selecting comparable individuals, who spoke French, from the three villages selected in French Guiana. There has also been a cohort study in the United States, by Oken et al [30]. They found a correlation between infant cognition and mercury levels, but no relationship to fish consumption.

Even if, as it appears from the various studies, the level of methylmercury to which most pregnant women are exposed by consumption of fish would lead to relatively small deficits in neurological development, these can still have large and measureable effects on society as a whole, completely excluding cases of acutely high exposure. Mental ability is a distribution and small shifts in the central tendency can cause long shifts in the tails of the distribution [31]. Additionally, the US EPA estimated that each lost IQ point costs the individual around $8,000[2] in reduced income over a lifetime [32]. This analysis was done for childhood exposure to lead and is based off an estimate of a 2.38% reduction in lifetime earnings per IQ point lost [33]. Sundseth et al. [34] extended this reasoning to methylmercury, estimating that it costs the United States $3.7 billion a year. This analysis is not to suggest that damage from mercury exposure is only financial, but that mercury controls can be a net gain for the economy.

The EPA has established a reference dose[3] for methylmercury exposure. This is 0.1-1 µg/kg/day for neurological impairment [35]. This reference dose is based on the longitudinal cohort study of the Faroe Islands. Previously, it was based on the dose response derived from exposure to tainted grain in Iraq. The reference dose was updated based on recommendations by the National Research Council after a review of all the available epidemiological data [17]. Interestingly, the value for the reference dose stayed the same before and after the study even though the data set changed. This data along with the most relevant exposure criteria set by other bodies is given in Table 1-1.

[2] The exact value is $8,346 per IQ point lost in 1995 dollars.

[3] A reference dose is an estimate of the daily exposure which is likely to have no appreciable risk of deleterious effects over a lifetime. The reference dose can be derived from a No Observed Adverse Effect Level (NOAEL), Lowest Observed Adverse Effect Level (LOAEL) or a benchmark dose. The uncertainty can span an order of magnitude. The reference dose includes consideration of potentially vulnerable subgroups [35].

Table 1-1: Exposure limits set by regulatory agencies or intergovernmental panels

Relevant Group	Mercury Form	Health Effect	Reference Dose/Exposure Limit
EPA[35]	Methylmercury	Developmental Impairment	1 µg /kg/day
CDC/EPA[36]	Blood Mercury	Developmental Impairment	5.8 µg/L
EPA[37]	Ionic (Drinking Water)	Renal Damage	2 µg/L
OSHA PEL[4] [36]	Elemental Vapor	Various	100 µg /m^3
NIOSH REL[5][36]	Elemental Vapor	Various	50 µg /m^3
NIOSH TLV[6] [36]	Elemental Vapor	Various	25 µg /m^3
WHO Annual Exposure Avg[7] [38]	Elemental Vapor	Various	1 µg /m^3

1.1.4 Mercury exposure assessment

The National Health and Nutritional Examination Survey (NHANES), an ongoing national medical survey of health and nutritional outcomes run by the CDC, investigated methylmercury levels in pregnant mothers in the 1999-2000 survey [29]. They found that 7.8% of women had blood mercury levels above the level generally considered safe (5.8 µg/L). These levels rose to 31.5% for certain ethnic groups, most likely due to differing food preferences [39]. Additionally, mercury blood levels vary with region and proximity to coasts, strongly correlated with fish consumption [40]. Concern over mercury has led to the avoidance of fish consumption. A practice that may deprive pregnant women of some of the health benefits conferred from eating fish [41]. The EPA and FDA have recommended limiting fish intake and avoiding certain species with high mercury levels. While this has not reduced the mean blood mercury level seen in NHANES data, it has reduced the number of cases above 5.8 µg/L [40].

1.2 Mercury cycle and fate and transport

1.2.1 Mercury sources

Mercury as an element is released from natural sources. Volcanoes, geothermal activity, wildfire and rock weathering all liberate mercury into the environment [42]. The United Nations Environmental Program undertook to catalogue the sources, transport, and fate of

[4] PEL is a Permissible Exposure Limit is the legal limit for exposure, either as a ceiling or a time weighted average. The value of 100 µg /m^3 is a ceiling value.

[5] REL is a Recommended Exposure Limit. For mercury the REL is a time weighted average for a 10 hour day and a 40 hour work week.

[6] TLV is a Threshold Limit Value set by the American Conference of Governmental and Industrial Hygienists for an 8 hour day and 40 hour work week.

[7] The WHO's annual exposure is a time weighted average over an entire year.

global mercury emissions. Their 2008 report found that total mercury emissions were approximately 3530 tonnes, of which 1930 tonnes were attributable to human activity. There is considerable uncertainty in those numbers, spanning a range from 1230-2890 and 900-2300 tonnes for human and natural emissions, respectively. Additionally mercury, as a volatile compound, will re-emit after being deposited on surfaces. It is not feasible to distinguish the proportion of re-emitted mercury from anthropogenic and natural sources. It is reasonable to assume that the portion is roughly 50%, mirroring the 50% split in the original emissions [42].

The bulk of anthropogenic mercury released to the atmosphere, 45%, comes from fossil fuel combustion for electric power, with coal the primary source of the mercury. Metal production, gold extraction, chemical manufacture, cement production, waste incineration, and dental amalgams (through cremation), also contribute significantly to the global mercury releases. The magnitudes and proportions of releases from these activities are given in Figure 1.1.

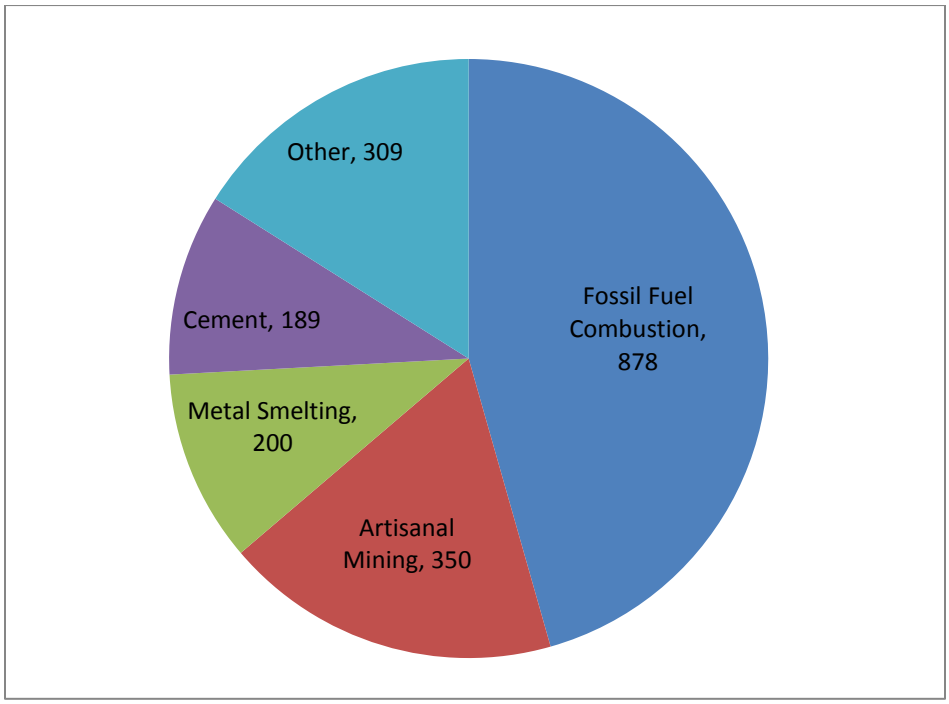

Figure 1.1: Sources of anthropogenic mercury by sector in tonnes. Other includes waste incineration (125 tonnes) chlor-alkali production (47), large scale gold production (111), and dental amalgams (26). Data is for 2005 from [42].

Mercury sources are also distributed by country and region of origin, with Asia emitting roughly two thirds. This is detailed in Figure 1.2.

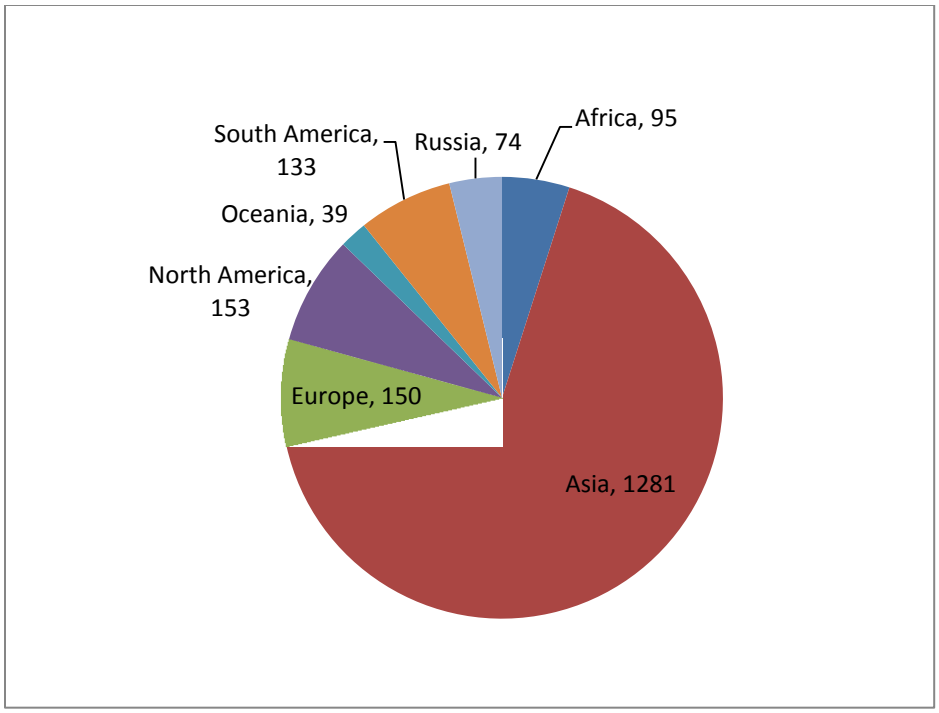

Figure 1.2: Regional sources of mercury emission in tonnes. 2005 data from [42].

There is a great deal of variation underlying many of these data with the mix of mercury emissions specific to each country being dominated by differing industries. In China, the United States, and India (the three largest mercury emitters) emissions are dominated by fossil fuel combustion. In Indonesia and Brazil, both within the top ten mercury emitters, artisan and small scale gold mining dominate the emissions [42]. While most large mining concerns have moved away from the use of mercury amalgamation as a method of gold extraction, many small scale miners continue the practice in which liquid mercury is mixed with the gold panning slurry, wetting and separating the gold. This gold-mercury amalgam is then heated. The mercury boils off and leaves the gold behind. This amalgam 'burning' can create mercury vapor levels up to 16,000 $\mu g/m^3$ [43], which far exceeds the recommended limits for occupational exposure set by the WHO [44] or NIOSH [36]. Often these amalgam burnings are done in populated areas, contaminating nearby buildings, and the escaped mercury can enter local waterways further increasing the risk from consumed fish [43]. There are an estimated 500,000-1,000,000 artisanal miners working in the Amazon alone, who have released approximately 2000 tonnes of mercury since the mid-1980s [43].

1.2.2 The mercury cycle

Mercury in the environment undergoes a complex cycle that is still not completely understood. The basic outline is as follows. It is released from power plants primarily as elemental or ionic mercury. The ionic mercury is more reactive and deposits near the power plant. The elemental mercury is fairly stable in the atmosphere and can be transported long distances. Its residence time has been estimated to be on the order of a year [45][46][47][48]. In the air some of the

mercury becomes oxidized and is deposited. In water, ionic mercury can be methylated by the addition of a methane group to the mercury, in a process mediated by bacteria. Methylmercury accumulates in tissues as it works its way up the food chain [42].

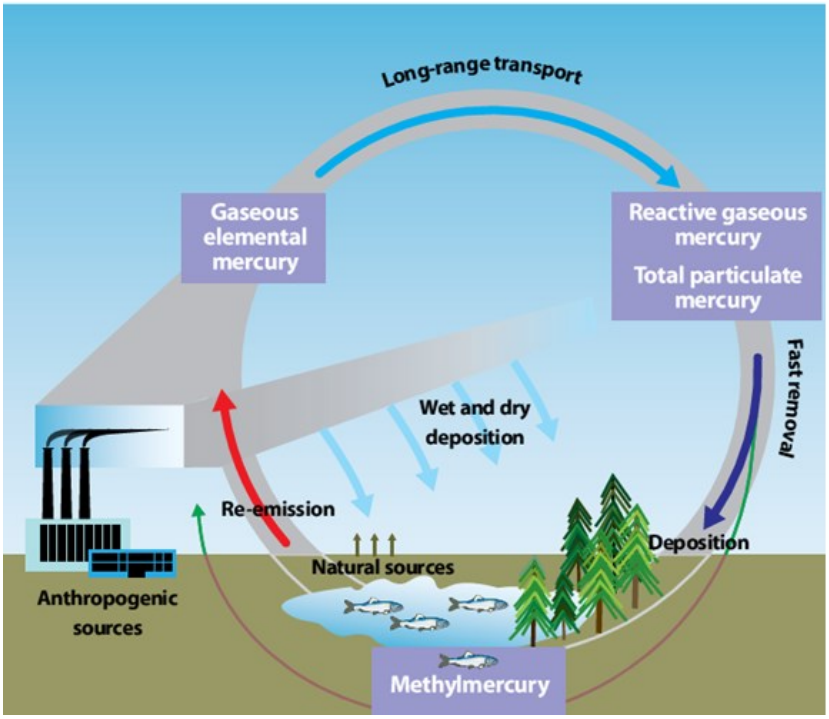

Figure 1.3 Mercury Cycle from [42]

Mercury emitted in ionic form or bonded to particulate matter tends to deposit close to sources, whereas, elemental mercury, with its long residence time and ability to be transported on strong wind currents, can traverse the globe. Several studies, using both direct measurements and atmospheric modeling, have shown deposition of mercury originating from Asia in the United States [49][50][51]. The strong westerly winds and the high amount of mercury released from eastern Asia contribute a significant fraction of the mercury deposited in the United States, in addition to their large contribution to the global atmospheric mercury stores [49]. The effects of mercury sources on the immediate surroundings should not be discounted. For example, the high emission density in regions of Asia can increase elemental mercury concentration 5-10 times over baseline (a mean value of 1.7 ng/m^3) [52]. This is in addition to the ionic and particulate bound mercury which is deposited close to sources. Mercury pollution is a complicated phenomenon and controls will involve local and global action.

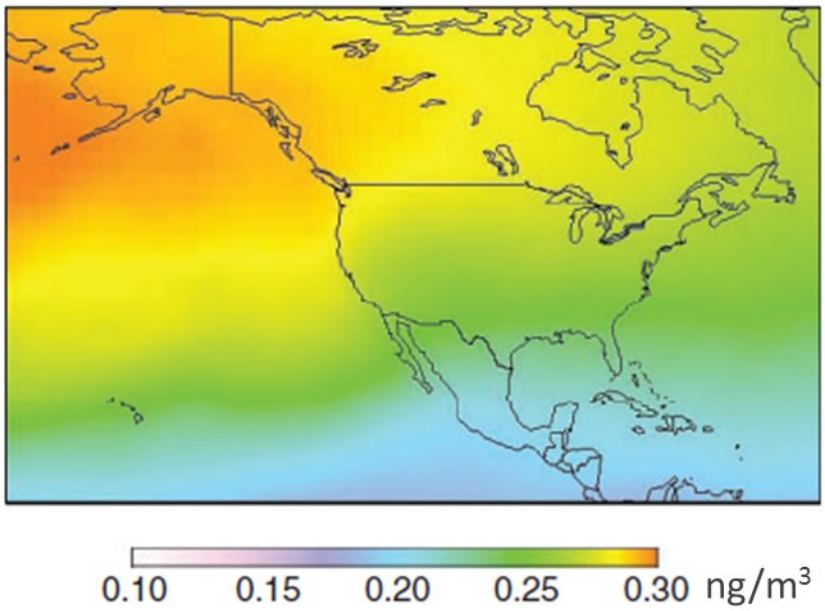

Figure 1.4 Deposition of Asian anthropogenic mercury over North America, adapted from [52].

1.2.3 Bioaccumulation of methylmercury

Increasing the complexity of controlling mercury is the tendency of methylated mercury to bioaccumulate. Mercury concentrations in fish species can be several orders of magnitude higher than ambient mercury concentrations in water [53][54][55], from ng/L levels to mg/L or ppt to ppm [56]. Several researchers have linked the trophic level of fish species to mercury concentration[57][58]. These studies were conducted at remote lakes in Northern Canada. These lakes are far from point sources or human disturbance, highlighting the global nature of mercury deposition. Investigations have also found that mercury concentrations in fish can be correlated with lake temperature and acidity [59][57]. Increased carbon levels in the atmosphere are expected to both raise temperature and water acidity. Predatory fish, higher on the food chain, show higher mercury levels. A selection of commonly consumed fish's mercury level is given in Table 1-2.

.

Table 1-2 Commonly consumed fish's mercury level data from the FDA [56], data is averaged from 1990-2010.

Species	Mean(ppm)	Standard Deviation (ppm)	Mean ug/100g
Anchovies	0.017	0.014	1.7
Catfish	0.025	0.005	2.5
Clam	0.009	0.002	0.9
Crawfish	0.033	0.035	3.3
Pollack	0.031	0.003	3.1
Salmon	0.022	0.015	2.2
Sea Bass	0.354	0.303	35.4
Shark	0.979	0.811	97.9
Shrimp	0.009	0.001	0.9
Snapper	0.166	0.113	16.6
Squid	0.023	0.016	2.3
Swordfish	0.995	0.87	99.5
Tilapia	0.013	0.004	1.3
Tuna (Canned, Abacore)	0.358	0.138	35.8
Tuna (Canned, Light)	0.128	0.078	12.8
Tuna (Fresh/Frozen)	0.391	0.34	39.1

The bioaccumulation of methylmercury is often ascribed to its greater lipid solubility. This explanation is incomplete as other inorganic forms of mercury have similar lipid solubility but do not bioaccumulate to nearly the same degree as methylmercury, with up to 90% of the mercury in fish being methylated [60]. Variation in the location of mercury accumulation within plankton cells, and how these differences facilitate trophic transfer, appear to account for the mercury speciation observed. Mason et al. (1995) found that methylmercury tends to be found in the cytoplasm of plankton, which transfer up the food web easier then inorganic mercury, which is bound preferentially in the cell membrane [60]. Additional research found that water chemistry and plankton speciation can have marked differences on methylmercury transfer and concentration in fish [53]. This helps to explain why different bodies of water can have marked difference in methylmercury concentration even among the same fish species and in the absence of point sources.

1.3 Regulation and detection of mercury

1.3.1 Regulatory background

Despite the long history of health effects from exposure to mercury and methylmercury, regulation to protect public health by limiting exposure has proceeded slowly and often only after serious outbreaks of mercury toxicity, such as Minamata Bay or the Iraqi Bread disaster. The first controls were voluntary standards and practice to protect those who would come into contact with acutely dangerous concentrations of mercury: laboratory workers, sailors, miners, goldsmiths, and workers in chemical and pesticide plants [61]. It was not until the 1960's and 1970's that the burgeoning environmental movement, strengthened by the repercussions of Minamata Bay, Iraq, and smaller, more isolated poisoning incidents in the United States, began to turn the government's attention towards mercury as a pollutant [62][61] . Some of the first regulations passed by a newly created EPA banned most ethyl- and methyl- mercury containing pesticides [61]. Additional regulation phased out use of mercury in industrial settings through taxes, process bans, and other controls. A grouping of recent regulations have banned mercury exports and use in thermometers [63]. Recent negotiations (Jan., 2013) have led to a preliminary multi-national reduction treaty, though it primarily focuses on plans to reduce emissions from artisanal mining [64].

The regulation of mercury in air and water, a particular focus of this dissertation, has followed a somewhat tortuous path, in some ways mirroring the political battles for many pollutants. Regulation has also been delayed by the complexity of mercury's cycle, forms, and effects on human health. The EPA has the authority to regulate mercury emissions to the atmosphere under the Clean Air Act. Before the 1990 amendment to the Clean Air Act mercury, as a Hazardous Air Pollutant (HAP) was regulated based on a health/benefit cost effectiveness standard. Debate over quantifying benefits and costs hindered and delayed effective controls. The 1990 amendment shifted to a technological regulations standard, a Maximum Achievable Control Technology (MACT), and focused on specific sources instead of pollutant by pollutant control. It also specifically listed mercury among HAPs to be controlled. In 1992, after the passage of the amendments, the EPA listed sources emitting mercury. Oddly, the EPA did not specifically list power plants, the largest source [62]. Over the next decade and a half the EPA issued rules for municipal waste incinerators, industrial boilers, chlor- alkali plants, and iron and steel foundries [63]. The EPA did not issue a final rule for coal power plants based on a MACTs standard. In 2000, before the change of administration, the EPA did determine that power plant regulation was 'necessary and proper.' After 5 years of study, it issued a cap and trade type strategy for power plants. Fifteen states in conjunction with various environmental groups sued, claiming the rule did not protect health. The suit was upheld by the US Court of Appeals for the DC Circuit, in 2008. The incoming Obama administration decided not to appeal the suit and commenced the rule process. A final rule was issued in December of 2011 [65]. Final implementation to regulate mercury emissions for all power plants will be in 2015 [66].

Similarly, the EPA has authority to regulate emissions and levels in drinking water, under the Clean Water Act and the Safe Drinking Water Act. It has set a limit of 2 µg/L for drinking water. This limit has not translated into regulation on fish, as food is regulated by the FDA. In fact

during the 1990s the EPA and FDA issued different reference doses for mercury consumption, leading to some confusion. To resolve this Congress mandated the 1997 Mercury Study Report and an NRC review of epidemiological literature [62]. Currently, the EPA and FDA monitor fish mercury levels and issue joint guidelines for consumption [56][67].

1.3.2 Current mercury detection methods

Current detection methods broadly fall into two categories: environmental monitors and occupational monitors. Environmental monitors are more sensitive and are typically used to investigate ambient concentrations and monitor exhaust from point sources. The current 'state of the art' environmental monitors are based on Cold Vapor Atomic Fluorescence Spectroscopy (CVAFS) [68]. CVAFS excites the mercury vapor with an ultraviolet light source and records the intensity of the emitted light [69]. To detect mercury levels at the low concentrations found in ambient air and flue gas the CVAAS uses a gold trap and an argon carrier stream. The gold trap pre-concentrates the mercury from the air. Upon heating the gold, mercury is released into the argon carrier stream. Argon is necessary as oxygen will quench the fluorescence signal from the mercury. In addition to being costly and complicated, the pre-concentration can introduce sources of uncertainty into the measurements [70]. Several companies manufacture CVAFS mercury detectors.

CVAFS forms the basis for environmental measurements of mercury in water, soil, or biological samples. Mercury is liberated from the sample through sequential oxidation, reduction, vapor separation, and collected in a gold trap. This chemical pretreatment is necessary as CVAFS measures elemental mercury, whereas the majority of mercury in water or biological samples is ionic, particulate, or methylated[71][72]. This technique has formed the basis for the EPA's Method 1631E, the standard for determination of mercury in water samples [73].

Conductometric detectors use the adsorption[8] of mercury vapor onto gold film to drive a change in the electrical resistance[74]. This approach is an efficient means to detect mercury vapor in air, as such it has been incorporated into commercial products to detect mercury, though the sensitivity of such products is limited (around 1 $\mu g/m^3$). Most of the application is in occupational or industrial hygiene settings for the detection of mercury spills and verification of clean up.

Several other techniques, not involving plasmonic absorbance of nanoparticles, have been developed to detect mercury. Their use is not widespread, nor have they been incorporated into commercial products or official standards. Mercury has also been detected by monitoring the changing resonance of a vibrating micro-cantilever [75][76]. As the mercury adsorbs onto the, often gold coated, surface of the cantilever, it changes the mass distribution and thus the resonance frequency. A similar method used changing surface acoustic waves on a gold coated silicon [77]. Sensors primarily for aqueous detection have been investigated utilizing fluorophores which turn off or on based on concentration of mercury, usually by mercury ions mediating bond length [78][79], and some of these have taken advantage of the fluorescent properties of nanoparticles[80].

[8] Adsorption is a surface phenomenon. Absorption is a bulk phenomenon. See Chapter 2 for more details.

1.4 Gold nanoparticles as mercury sensors

1.4.1 Noble metal nanoparticles background

1.4.1.1 Description of noble metal nanoparticles

It has been suggested that colloidal gold was used for artistic and medicinal purposes starting in the 4th or 5th century in Egypt and China [81]. The most striking and durable examples of nanoparticle use come from stained glass. The addition of noble metals during glassforming created vivid colors. The most notable example is the 4th century Lycurgus Cup, crafted by the Romans, which appears green under reflected light and red under transmitted [82]. TEM and theoretical effective medium calculations have concluded that the presence of gold-silver alloy nanoparticles creates this striking optical effect [83][84].

Several authors, including Francisci Antonii in 1618 and Johann Kunckels in 1676, published treatises on colloidal solution; however, it was Michael Faraday who brought the attention of the wider scientific community to the connection between metal colloids and optical properties [85][81]. In the 1857 Bakerian Lecture he investigated the optical properties of colloidal gold formed from the reduction of chloroauric acid and the color changes in thin films [85]. These vivid optical properties arise due to the interaction of light with the nanoparticles' electrons.

Metals have a large number of valence electrons which are able to travel freely through the material. When disturbed from their equilibrium position, the electrons can oscillate around the positive ion cores, analogous to a mass on a spring. This collective oscillation of charged particles is termed a plasmon [86]. When the oscillations are along the surface of the material where it is more able to interact with the surrounding material or external electromagnetic waves, it is termed a surface plasmon. Again like the mass spring systems, these surface plasmons tend to oscillate at a specific resonance frequency. When the surface plasmon is confined by the shape of the material such that the material dimension is less than the wavelength of the exciting light, the phenomenon is termed Localized Surface Plasmon Resonance (LSPR) [87][82][88]. The oscillation of these localized surface plasmons is dominated by the surface effects, as the mean free path of the plasmon is typically larger than the size of the material [87]. As such, the resonance frequency of the localized surface plasmon is strongly dependent on the size and shape of the particle and on the dielectric function of the material and its surroundings [87][88]. Thus the optical properties of the material can be tuned by changing the size, shape, or composition of the particle.

1.4.1.2 Theoretical models of noble metal nanoparticle light absorption

One of the first theoretical treatments of the optical properties of nanoparticles was developed by Gustav Mie in 1908 [89]. Mie solved Maxwell's Equations for light interacting with a spherical particle, when the particle is smaller than the wavelength of the light. The wavelength and intensity of the light scattered from the spherical particle is related to the size and composition of that particle's material and the surroundings. Mie's solution is given below:

$$C_{ext} = \frac{24\pi^2 R^3 \epsilon_m^{3/2}}{\lambda} \frac{\varepsilon''}{(\varepsilon' + 2\varepsilon_m)^2 + \varepsilon''^2} \quad \text{(Equation 1)}$$

Where C_{ext} is the extinction coefficient, R is the particle radius, ε_m is the dielectric constant of the surrounding material and $\varepsilon'+\varepsilon''i$ is the complex dielectric function of the particle's material.

The solution was extended in 1915 by Richard Gans to oblong particles[90], a good approximation for nanorods [91]:

$$C_{ext} = \frac{8\pi^2 R^3 \epsilon_m^{1.5}}{3\lambda} \sum_{k=a}^{c} \frac{\frac{1}{P_k^2}\epsilon_2}{\left(\epsilon_1 + \frac{(1-P_k)}{P_k}\epsilon_m\right)^2 + \epsilon_2^2} \quad \text{(Equation 2)}$$

Where Pj are the depolarization factors of the axes (a>b=c)

$$P_a = \frac{1-L^2}{L^2}\left(\frac{1}{2L}\ln\left(\frac{1+L}{1-L}\right) - 1\right) \quad \text{(Equation 3)}$$

$$P_b = P_c = \frac{1-P_a}{2} \quad \text{(Equation 4)}$$

Both of these solutions assume that the particle is smaller than the wavelength of the incoming light and sees a uniform electric field. This dipole approximation neglects higher order terms.

1.4.2 Noble metal nanoparticle synthesis and assembly

1.4.2.1 Nanoparticle synthesis

Our ability to synthesize and deposit nanoparticles with control and precision has increased interest in noble metal nanoparticles in the last few decades. Gold and silver nanoparticles can be synthesized at high yields in a wide variety of shapes and sizes. Post-synthesis processing can replace coatings on the particles, allowing them to be deposited on substrates. This treatise will not go into detail on the wide variety of synthesis and deposition methods; it will highlight two, each which have proven useful in the development and testing of mercury detection sensors.

Perhaps the most popular method for the synthesis of gold nanospheres was developed by Turkevich et al. in 1951 [92]. This method is broadly similar to the methods employed by Faraday in his work making colloids [81][62]. In the method, chloroauric acid ($HAuCl_4$) in water is reduced with sodium citrate. The citrate acts as both as a reducing agent on the gold ions, but also stabilizes the nascent nanoparticles preventing aggregation [92]. Frens (1973) improved

the size selection by controlling the ratio of citrate added [93]. Today, citrate stabilized gold nanoparticles in aqueous solutions are commonly synthesized in nominal sizes from 10nm to 100nm.

The seed mediated growth method allows for the creation of gold nanorods in a variety of sizes and aspect ratios with tight distribution (10-15%) [81]. The method, developed by Murphy et al., involves first the reduction of chloroauric acid to form gold seeds (1-2 nm particles). The seed solution is then added to a solution of more chloroauric acid, a mild reducing agent (often ascorbic acid), and a micellar template, usually cetyl trimethlyammonium bromide or CTAB [94][95][96]. The micellar template preferentially binds along a face of the particle supporting growth into rod structures from the nucleus of the seed. Aspect ratio and size can be controlled by the size of the seed, the relative ratio of chloroauric acid and CTAB , the pH of solution, the temperature of solution, and the addition of extraneous metallic ions [97][98][99][100][101][102].

1.4.2.2 Nanoparticle assembly

Citrate or CTAB coated nanoparticles are stable in water, though they quickly aggregate in organic solutions and do not disperse into controllable mono or sub-mono layers on substrates. They can be drop cast onto glass slides. Such films tend to be non-uniform, easily disturbed, and subject to aggregation. Deposition can be improved by replacing a portion of the stabilizing agent post synthesis with a different functional molecule. Liz-Marzan et al. pioneered a technique to accomplish this using a silane molecule in their work creating core-shell silica coated gold and silver nanoparticle [103][104]. Post synthesis a fresh solution of (3-Aminopropyl) trimethoxysilane, APS, is added to the citrate stabilized gold nanosphere solution. The APS, a commonly used silanizing agent, is a chain molecule with a silicon atom. The amine group bonds to the gold surface displacing the citrate, while the oxysilane group is free to bond to silica, depicted in Figure 1.5.

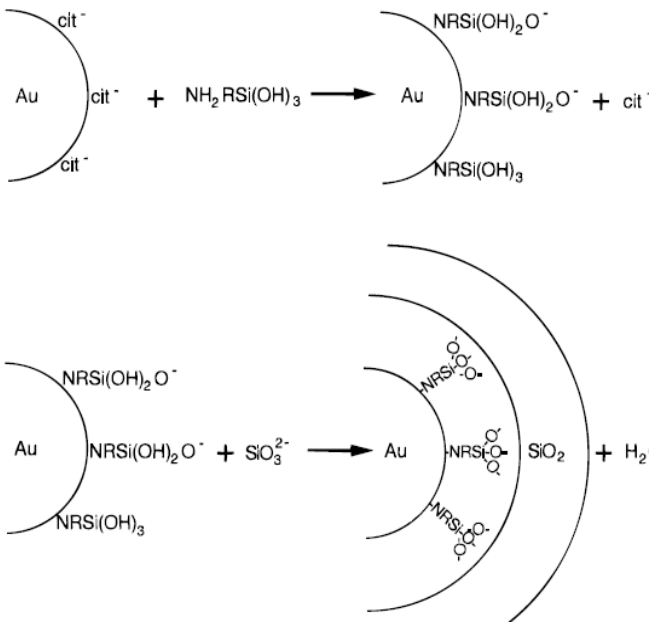

Figure 1.5 Diagram of citrate to silane replacement on gold nanoparticles from [104].

This process has been modified and adapted, proving to be of great utility in the construction of stable gold and silver nanoparticle thin films on silica surfaces, and as a useful substrate for a variety of chemical and biological sensors. Jin et al. used a similar procedure to immobilize gold nanoparticles on glass slides, which they then electrolessly plated and used as an SPR substrate. They investigating the surface morphology and electrical properties [105]. Frederix et al. modified the procedure, using a slightly different silane molecule, (3-mercaptopropyl) methyltriethoxysilane, and a quartz substrate. They then used these surfaces as a biosensor. In a scheme repeated in other sensors, a protein receptor is attached to the nanoparticle film. When the protein bonds with that receptor, the local index of refraction is changed causing measurable shifts in the SPR [106].

1.4.3 Nanoparticles as sensors

Increased facility with nanoparticle synthesis and deposition has led to growth in the applications for noble metal nanoparticles based around their unique optical properties. The enhanced scattering has made the particles attractive for imaging studies, such as in cancer screening[9] [108][87]. They possess tunable fluorescence properties leading to possible applications in light harvesting, bioassays, and molecular interactions [109][110][111]. A great deal of work has been done on the enhanced Raman emissions of various species in close proximity to various noble nanoparticle structures [87].

[9] Similar work has continued along this line, utilizing the enhanced electromagnetic field caused by the LSPR as a means to kill cancer cells [107].

Sensing with surface Plasmon resonance is a well-established technique. The first sensors used thin metallic films to detect gas and biological substance [112][113]. These sensors were fabricated by evaporating a metal and depositing it as a thin film onto a glass prism, the prism being necessary to match the momentum and energy of the incident light to the surface plasmon. The metallic film is functionalized with an antigen for the target molecule, which upon binding to the antigen changes the local electrical properties and hence the reflectance of the light returning from the prism [113]. A similar method was developed for the detection of gasses based on the absorption of a target gas into a polymer coating on the surface [114]. Many of the advances in the field since then have been driven by interest from the biological community based on some of the inherent advantages in SPR sensing, namely real time analysis and label free detection. Several companies have been formed to take advantage of this system offering commercial SPR biosensors [113][115]. Several sensors have been demonstrated that detect various hydrocarbon gases, NO_2, H_2S, NH_3, hydrogen, and various ions [115].

LSPR sensors grew out of the work with surface plasmons. The key difference between the two is the localization of the surface plasmon due to the confinement by the nanostructure. Localization of the plasmon provides several advantages over SPR sensors. LSPR sensors do not require a prism, or similar device, to couple the light into the plasmon. The confinement of the plasmon by the nanostructure allows the light to interact directly with the oscillating charges. This advantage in geometry and size enables sensors which are smaller and less cumbersome. For example Stuart et al. [116] deployed an in vivo silver nanosphere based sensor to monitor glucose levels within a Sprague-Dawley rat. The second advantage comes from the wide variety of nano-structures that can be synthesized. Sensors have been demonstrated with nanospheres, nanorods, nanoshells, nanocubes, nanopyramids, nanostars, and nanoarrays in both silver and gold with a wide variety of functionalizing coatings [117]. Occasionally a less common plasmonic material such as copper is used [118]. The nanoparticle transducer can to be tuned to the application, in terms of wavelength absorbance peak, sensitivity to index of refraction changes, and material compatibility. For example, gold nanoparticles are often preferred to silver ones, which have a stronger LSPR absorbance peak, because gold is more stable and bonds with thiol terminated molecules. Additionally, while not taken advantage of in this work, coupling between plasmons of adjacent nanoparticles drastically alters the LSPR of the system, creating opportunities for highly sensitive devices [117][119].

1.4.4 Interaction of mercury with gold nanoparticles

1.4.4.1 Adsoprtion of mercury vapor on gold films

Humans' long interaction with mercury and gold, the metals' unique physical properties and value have led to many investigations, some predating the scientific method. Several relatively recent studies have examined the interaction that drives the well-established adsorption and subsequent amalgamation of mercury and gold. These studies have been facilitated by

advances in techniques for probing material on the micro- and nano- scale and motivated by the need to better understand the physics underpinning much of mercury detection.

Several studies probed the mixing of mercury and gold on a macroscopic level. They have documented changes in the electrical properties, work function, and resistance of thin gold films upon exposure to various concentration of mercury vapor [74][120][121]. Additional studies evaluated the collection of mercury on gold or silver surfaces, such as wools, coated beads or wires. They generally found high collection efficiencies and postulated that sticking probabilities were near one[10], at least for initial exposures [122][123][124]. In the late nineties several studies began to apply new nano- scale investigation tools to this problem. Yang et al. (1995) looked at mercury adsorption on gold films in acid under electric potentials with Atomic Force Microscopy (AFM) [125]. Basttistoni et al. [126]used a variety of techniques (XPS, SIMS, SAM, and SEM)[11] to probe mercury adsorption. They determined that under low concentrations, mercury was deposited in a thin subsurface layer. At high concentrations, the film was irreversibly deformed; this deformation was attributed to poor surface adhesion between the gold and silicon substrate. They also measured the resistance changes in the film in real time, finding concentration dependent adsorption and saturation, which is characteristic of later work (described presently) and the work presented here in later chapters. Nowakowski et al. [127] investigated mercury adsorption with AFM. They found surface morphology changes dependent on concentration and postulated preferential adsorption along grain boundaries of defects.

In 1999 Levlin et al. [128] presented a detailed and influential study of mercury adsorption onto gold and silver polycrystalline surfaces vacuum deposited onto mica substrates. They were able to control temperature and concentration of mercury in air in their exposure chamber. The quantity of adsorbed mercury was determined by two separate methods: the dissolution in strong nitric acid and by thermal desorption. The former method yielded 20% higher results, which suggested the incompleteness of thermal desorption. The surface morphology was also investigated with a Scanning Tunneling Microscope (STM). Two series of experiments were run for mercury on the gold: the first, a constant concentration of 30 $\mu g/m^3$, at different temperatures; the second increasing concentrations at 90 ^oC. They both found mercury adsorbed as 'islands', not as more complete monolayers, nor as multilayer structures. The size of the islands and their growth rates were influenced by temperature and concentration. At all but the most elevated temperatures the system would reach a 'saturation' point when mercury adsorption would proceed at a slower pace. Figure 1.6 illustrates the relationship between time temperature and surface coverage, and Figure 1.7 illustrates the relation between varying concentrations and surface coverage.

[10] This postulate of a unity sticking probably may have been due to lack of clarity between sticking probability and collection efficiency.

[11] XPS is X-ray Photoelectron Spectroscopy; SIMS is Secondary Ion Mass Spectrometry; SAM is Scanning Auger Microscopy; and SEM is Secondary Electron Microscopy.

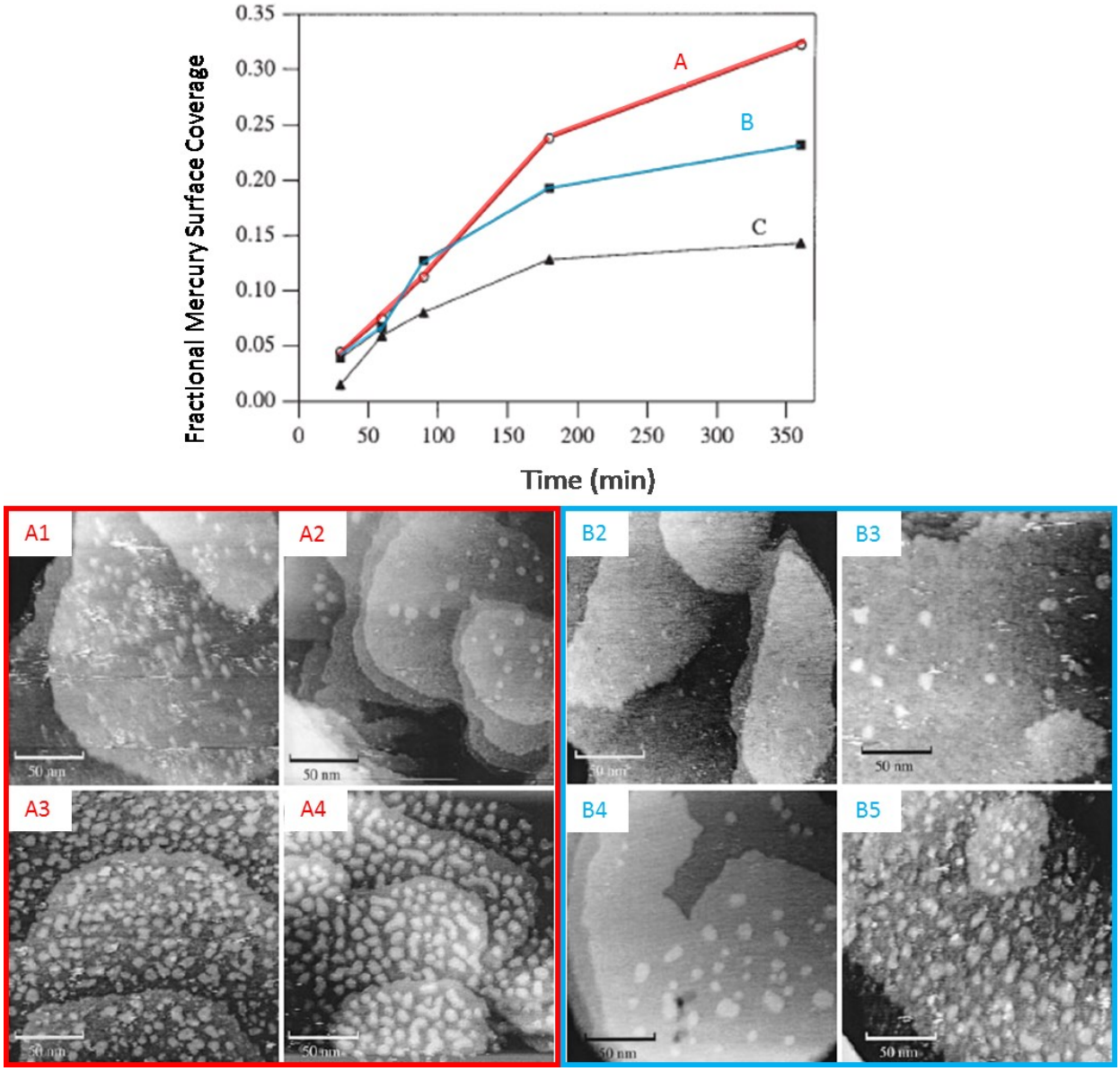

Figure 1.6 Percent surface coverage of gold films exposed to 30 ng/L of elemental mercury. Curve A is at room temperature, curve B is at 60°C, and curve C is at 90°C. Subsets A and B 1-4 are TEM images at 60, 90, 180 and 360 min respectively. Adapted from [128].

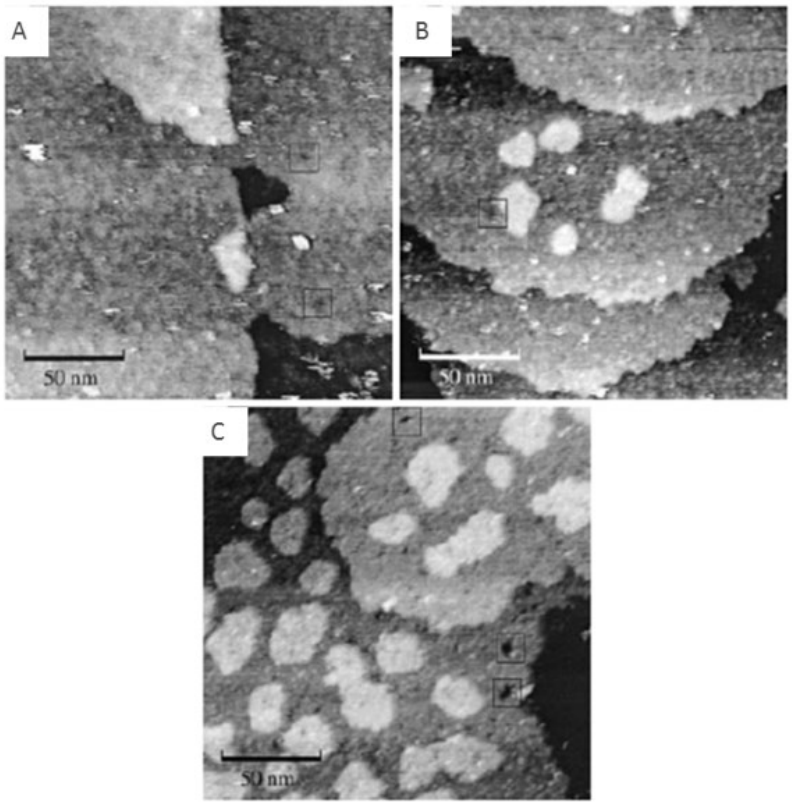

Figure 1.7 STM of gold thin film exposed to A) 30 ng/L, B) 130 ng/L, and C) 320 ng/L for 60 min at 90°C. Adapted from [128].

To explain their findings they proposed a place exchange mechanism, where mercury would initially adsorb onto an available site, defect or edge, but was then free to translate across the surface until forming or joining into one of these amalgam islands. This model does not explain the concentration dependent saturation condition. It would be explained if there was an equilibrium between adsorption and desorption from the surface, though they did not observe any desorption during removal of the sample from the exposure chamber and transport to the STM. To account for this discrepancy, they proposed that the amalgam islands provided additional energy needed for further mercury adsorption [128].

Kobiela et al. [129] extended this work using XRD, AFM, and resistivity measurements to investigate mercury adsorption onto thin gold poly crystalline films under different gases: hydrogen, argon, and air. They also confirmed 'island formation' and found the presence of various amalgams: AuHg, $AuHg_2$, and Au_3Hg, depending on temperature. They found that island formation and the amalgamation process is dependent on mass transport to the surface. Amalgamation formation was slower in the heavier gasses due to the smaller diffusion

coefficient as predicted by the Chapman-Enskog diffusion coefficient equation. The exception being vacuum which was much faster, due to the transfer being driven by ballistic transport, and air where some contaminant in the atmosphere may have bonded to some surface sites making them unavailable to mercury adsorption [129].

1.4.5 Prior gold nanoparticle mercury sensors

The natural affinity of gold for mercury and the increased facility for making and depositing nanoparticles with noble metals has led to their use as possible sensors. Several works since 2000 have used nanoparticles for mercury detection [79]. Of some interest are the studies that detect aqueous ionic mercury. The ionic mercury reacts with DNA, reducing the distance between nanoparticles bonded to the DNA, and thus altering their optical absorbance [130][131][132][133]. The ones that are most relevant to this work, however, rely on the direct absorption of Hg on gold and the monitoring of the resultant changes in the surface plasmon resonance.

Morris and Szulczewski [134] examined shifts in the SPR of films of silver, gold, and gold/silver alloy films. They found initial linear shifts due to mercury adsorption. Their work focused the responses of different metal films at a fixed concentration (15 ppm, or 130 mg/m^3) and the flow rate (3-4 ml/min). While silver films had a larger response than gold, the paper suggested that gold films, or an alloy, may be preferable due to the increased stability of gold [134]. Continuing this work, the same group looked at the response of various sizes of nanospheres in aqueous solution exposed to mercury bubbled through the solution in a nitrogen stream [135]. They found noticeable (~5nm) blue shifts in the LSPR peak. This system required long exposure times and was impractical as a working sensor as the solution had to be removed at a constant interval, 15min, to record the absorbance spectrum [135]. Improving on this design, the group measured the resonance of gold nanosphere films deposited on silica and glass slides by a variety of preparation methods: layer by layer, Langmuir-Blodgett, and salinization [136]. This work again showed shifts in the LSPR peak, but they were only measuring the total shift after the nanoparticles had saturated.

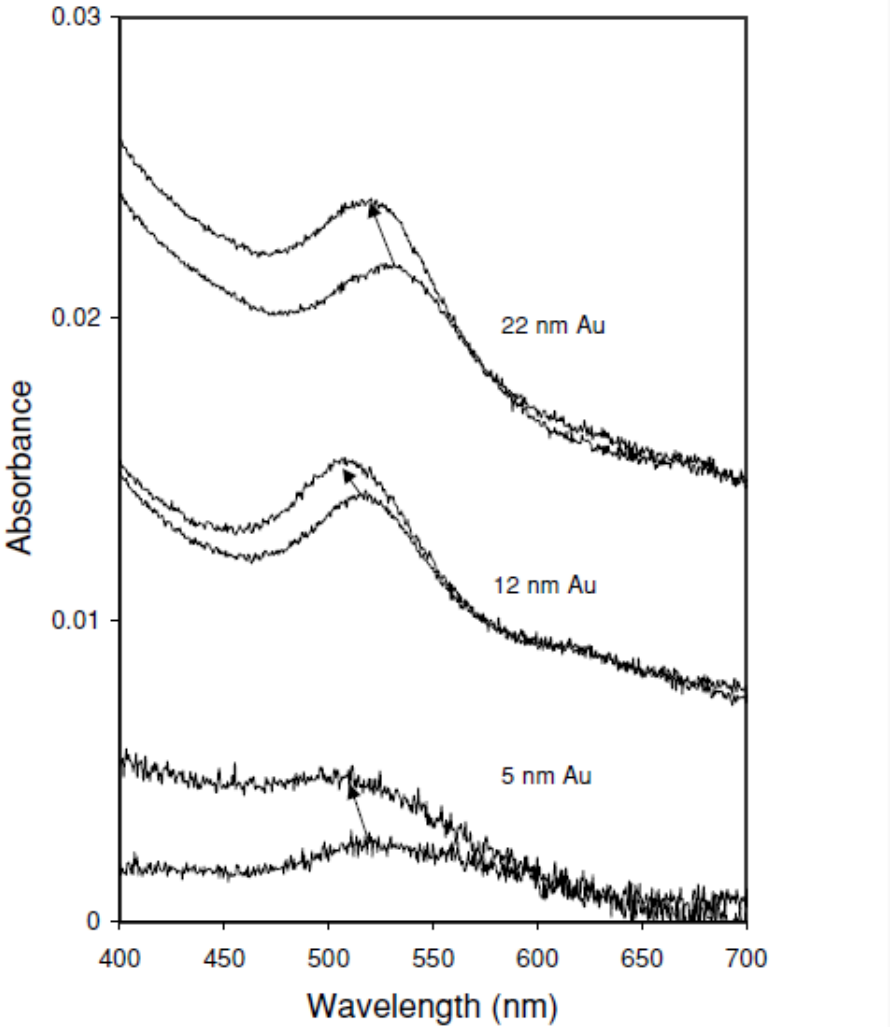

Figure 1.8 Peak wavelength shift observed by Morris et al. after exposure of gold nanoparticle films to mercury vapor from [135].

A response based on total shift would render the design somewhat impractical for a working sensor[12], it did prove the concept that gold nanoparticles would function as mercury sensors. They also performed XPS and EDS on the films and showed that a significant fraction of mercury adsorbed on the particles (between 3-15 %) [136].

Rex et al. [137] investigated the use of nanorods as a sensing medium for ionic mercury in water. They chose rods, as the longitudinal peak of the rods is more sensitive to changes in index of refraction, which could allow a lower limit of detection. The work claimed a limit of detection of 6.6×10^{-13} g/L based on extrapolation of the peak shift seen, which they ascribed to

[12]The total shift in LSPR of a gold nanoparticle is proportional to the mass of mercury adsorbed. Thus a low concentration of mercury over a long time would be indistinguishable from a high concentration of mercury over a short time.

changes in the aspect ratio of the rods [137]. For mercury ions to adsorb onto the gold nanoparticles, they need to be reduced in the solution. The reducing agent chosen, sodium borohydride, is also used in the synthesis of the nanorods. It is thus possible that the sodium borohydride alone or in concert with mercury led to some of the shape change and peak shifts observed.

Previous work in our lab on gold nanoparticles deposited onto quartz substrates by Langmuir Blodgettry established the suitability of deposited nanoparticles as mercury senor. Particles display a linear relationship between mercury concentration and LSPR peak shift rate. In addition, this prior work performed initial investigations on the importance of the mercury mass transfer to the surface, and it demonstrated regeneration of the nanoparticles [138].

This thesis builds upon the prior work in the lab, and more broadly the field in general, with the overarching goal of improving health through better mercury measurement techniques. This work quantifies the phenomena behind sensor response, namely the mass transfer and surface kinetics of mercury adsorption. The work then takes these results, and results from prior external experiments, and applies them towards expanding the capabilities of gold nanoparticle based mercury detection to fiber optic systems and aqueous measurements.

2. Mass transfer, surface kinetics and thermodynamics of mercury adsorption on gold nanoparticles

This section investigates some of the fundamental relationships driving the adsorption of mercury onto gold nanoparticles. Relevant background on mass transfer and adsorption kinetics is presented. Experimental results based on a gold nanoparticle mercury sensor utilizing an impinging flow geometry are discussed. To decouple the effects from mass transfer and adsorption, electrical analogy models are constructed and fit to the experimental data. The models can account for variations in flow conditions and surface coatings on the nanoparticles.

2.1 Background

2.1.1 Mass transfer and gas sensors

As the response of a mercury sensor depends on the number of mercury atoms deposited on the surface, mass transfer must play an important role in the performance of the sensor. Any sensor which depends on the adsorption or contact of a target molecule with a transducer will be limited, to some degree, by the effectiveness of the transport of the target species from the environment to the transducer. Despite the fundamental importance of this phenomenon there is relatively little attention paid to mass transfer concerns specific to gas sensors. This lack is particularly evident when examining the literature where mass transfer plays a crucial role in other fields, such as catalysis, gas handling, chemical engineering, water and soil remediation, and some recent works in biosensing. Many of the results from these fields, and more broadly heat transfer, could be applied to gas sensors to validate and improve performance. In general, in the sensor literature, mass transfer, if even mentioned, is either neglected as not response limiting or ignored as a potential means to improve sensor performance.

Some of the previous work which addresses mass transfer in gas sensors arises from applications related to catalysis. For example, Ackelid and Petersson [139] examined Metal-Oxide-Silicon (MOS) hydrogen sensors. Palladium deposited on an oxide layer of a silicon wafer acts as a capacitor in an architecture similar to field effect transistors. The palladium, a hydrogen catalyst, converts H_2 into H_20. This conversion and some of the hydrogen absorbing into the interface layer changes the potential across the device. These sensors are susceptible to mass transfer effects as the analyte species is constantly being consumed and the product species, H_2O, must be removed from the surface. In their investigations they found a smaller active area had a higher sensitivity, as the unused portion of the palladium device acted as a sink for hydrogen. There was a dependence on the diffusion coefficient which they modified by changing both pressure and carrier gas. They were designing for conditions where the sensor is kinetically controlled and where mass transfer effects could thus be neglected.

Johansson et al. [140] also examined similar palladium-hydrogen catalytic surfaced MOS sensors. They completed numerical simulations and measurements, and found qualitative agreement between model and experiments, in that shape and trends for response to increasing mass flow and sensor area were similar to those in the Ackelid and Petersson work; however, it was difficult to directly compare the two different studies, and even to compare the

model and experimental results due to the assumptions about physical constants, such as the sticking coefficient and adsorption and desorption constants.

Lezzi et al. [141] investigated CO sensors based on similar field effect devices with a tin oxide surface. The focus of this work was the influence of test chamber geometry on the sensor response. Two chambers, an impinging flow chamber and a cross flow chamber, were tested. Most of the discussion concerned the impinging flow chamber. As expected, the results showed a dependence between flow rate and the time required to reach the same concentration at the sensor as at the inlet. There was broad agreement between the model and the experiment; however, the sensor response time was too slow to follow the initial shift in concentration, especially for high flow rates.

Zhu at al. [142] evaluated chemical sensors on titanium dioxide nanospheres and did see a flow rate dependence on the luminescence, but they did not investigate this effect any further than to determine that the surface activity at the testing conditions was diffusion limited.

2.1.1.1 Mass transfer and biosensors

A brief aside is warranted to highlight some research from the field of biosensors, in particular microscale biosensors, which in recent years has grappled deeply with the issues of mass transfer and sensor response. Several articles have dealt with the issue in a systematic way, applying some of the tools developed in engineering to improve sensor performance. The impetus for this work is more pressing in the field of biosensors as large molecules in fluids can have diffusion constants several orders of magnitude smaller than in gas systems, and concentrations and sample volumes can be quite low, in the picomolar and microliter range, respectively.

Sheehand and Whitman [143] used analytical calculations and finite element simulations to determine the collection efficiency of DNA-like molecules on a sensor. They found size, shape, and flow conditions profoundly affected the total flux. They concluded that without some method to actively direct the molecules to the sensor the sensitivity would be on the order of picomoles, despite several reports of limits of detection orders of magnitude lower. Kim and Zheng [144] also used analytical calculations and numerical methods to attempt to improve the performance of sensors through enhanced mass transport. Channel configuration and geometry optimization led to a predicted improvement in sensor response time by an order of magnitude. Experiments done by others showed similar results [145].

Squires et al. [146] provided a physically intuitive picture of biosensors by means of dimensionless groups, particularly Peclet and Damköhler numbers. The Peclet number is the ratio between convective and diffusive transport, and the Damköhler number is the ratio of reaction rate to diffusion flux. By plotting various regimes they were able to make predictions concerning flow depletion, collection efficiency, and the limiting behavior, when systems were reaction limited, diffusion limited, or balanced. Despite the completeness of model presented, they were unable to explain the order of magnitude discrepancy between experimental results

and predictions. The results presented were only for a rectangular cross flow channel, though they are extendable to other geometries.

2.1.1.2 Mass transfer and sensor response

Even with the generally higher diffusion coefficients, improving the mass transfer in a gas phase sensor can improve performance, particularly at low concentrations. Knowing the mass transfer characteristics can indicate if the sensor is diffusion limited, and help identify situations where a sensor response is the result of other factors, such as surface reactions or interferences, rather than actual analyte transport and detection. The relative lack of investigation into mass transfer effects in this field stands in marked contrast to the field of heat transfer where considerable effort has been expended into improving the transfer of heat under a wide variety of conditions.

The comparison with heat transfer is particularly apt because it is possible to use many of the relationships derived for that field in mass transfer. The following procedure uses the well-known example of a boundary layer over a flat external plate [147][148].

Similar to the velocity boundary layer, a temperature boundary layer will arise due to a difference between the free stream temperature and the temperature on the surface. Analogously, a concentration boundary layer forms when there is a difference between concentrations in the free stream and on the surface, where sorption or a chemical reaction can occur.

The governing equations for a steady, two-dimensional, incompressible flow boundary layer are as follows:

Conservation of mass:

$$\frac{du}{dx} + \frac{dv}{dy} = 0 \qquad \text{(Equation 5)}$$

Conservation of x-momentum:

$$\rho \frac{Du}{Dt} = -\frac{dP}{dx} + \mu \nabla^2 u + X \qquad \text{(Equation 6)}$$

Conservation of y-momentum:

$$\rho \frac{Dv}{Dt} = -\frac{dP}{dy} + \mu \nabla^2 v + Y \qquad \text{(Equation 7)}$$

Conservation of energy:

$$\rho c_p \frac{DT}{Dt} = k\nabla^2 T + \mu\Phi + \dot{g} \quad \text{(Equation 8)}$$

where $\mu\Phi$ is a viscous dissipation term, often treated as negligible and neglected here:

$$\mu\Phi = \mu\left\{\left(\frac{du}{dy} + \frac{dv}{dx}\right)^2 + 2\left[\left(\frac{du}{dx}\right)^2 + \left(\frac{dv}{dy}\right)^2\right]\right\} \quad \text{(Equation 9)}$$

Conservation of species, in this case a dilute mixture of species A in a larger volume of species B:

$$\frac{DC_A}{Dt} = \mathfrak{D}_{AB}\nabla^2 C_A + \dot{N}_A \quad \text{(Equation 10)}$$

Typically in boundary layer it is possible to make several simplifying assumptions, making the equations tractable to analytical solutions:

$$u \gg v \quad \text{(Equation 11)}$$

$$\frac{du}{dy} \gg \frac{du}{dx}, \frac{dv}{dx}, or \frac{dv}{dy} \quad \text{(Equation 12)}$$

$$\frac{dT}{dy} \gg \frac{dT}{dx} \quad \text{(Equation 13)}$$

$$\frac{dC_A}{dy} \gg \frac{dC_A}{dx} \quad \text{(Equation 14)}$$

The variables for (Equation 5 through (Equation 20 are given in Table 1.

Table 2-1 Description of variables for boundary layer problem

Symbol	Variable Name
$\boldsymbol{u}$	x velocity
$\boldsymbol{v}$	y velocity
$\boldsymbol{\rho}$	density
$\frac{\boldsymbol{D}(\,)}{\boldsymbol{Dt}}$	substantial derivative
$\boldsymbol{P}$	pressure
$\boldsymbol{\mu}$	Viscosity
$\boldsymbol{X}$	x body forces
$\boldsymbol{Y}$	y body forces
$\boldsymbol{c_p}$	specific heat
$\boldsymbol{T}$	temperature
$\boldsymbol{k}$	thermal conductivity
$\dot{\boldsymbol{g}}$	heat generation
$\boldsymbol{C_A}$	concentration of species A
$\mathfrak{D}_{\boldsymbol{AB}}$	diffusion coefficient of species A in B
$\dot{\boldsymbol{N}}_{\boldsymbol{A}}$	generation of species A
$\boldsymbol{\eta}$	similarity variable
$\boldsymbol{Re}$	Reynolds number
$\boldsymbol{Pr}$	Prandtl Number
$\boldsymbol{h_m}$	mass transfer coefficient
$\boldsymbol{L_{char}}$	characteristic length scale

The most famous solution to these boundary layer equations was developed by Blasius [149] for a momentum boundary layer by taking advantage of a similarity variable:

$$\eta \equiv y\sqrt{\frac{u_\infty}{vx}} \qquad \text{(Equation 15)}$$

With the hydrodynamic conditions known, it is possible to solve the heat transfer problem by again postulating the existence of a similarity solution. The result for a laminar flow and uniform surface temperature, reformatted in terms of a Nusselt number [147][148], is:

$$Nu_x = 0.332Re^{\frac{1}{2}}Pr^{\frac{1}{3}} \quad Pr > 0.6 \qquad \text{(Equation 16)}$$

The average heat transfer over a plate of length L is found by integrating the above:

$$\overline{Nu_x} = 0.664 Re^{\frac{1}{2}} Pr^{\frac{1}{3}} \quad Pr > 0.6 \qquad \text{(Equation 17)}$$

Because the forms of the energy and the species conservation equation are the same the solution will be the same with different variables. It is convenient to define a different dimensionless group such as the Schmidt number, Sc, a ratio of momentum and mass diffusivities analogous to the Prandtl number:

$$Sc = \frac{\nu}{\mathcal{D}_{AB}} \qquad \text{(Equation 18)}$$

and the Sherwood number, a dimensionless mass transfer flux analogous to the Nusselt number:

$$Sh = \frac{h_m L_{char}}{\mathcal{D}_{AB}} \qquad \text{(Equation 19)}$$

The solution for the average mass transfer coefficient over a flat plate takes the same form:

$$\overline{Sh_x} = 0.664 Re^{\frac{1}{2}} Sc^{\frac{1}{3}} \quad Sc > 0.6 \qquad \text{(Equation 20)}$$

This solution makes clear the variables which can be manipulated to improve mass transfer of mercury to the gold nanoparticle surface: the physical properties of the system, the diffusion coefficient, and viscosity. The diffusion coefficient is part of the Sherwood and Schmidt number, and the viscosity is part of the Reynolds and Schmidt number. It is possible to change these physical properties, diffusion coefficient and viscosity, by changing temperature, pressure, or carrier fluid.

Increasing the flow rate would increase the Reynolds number and the mass transfer. It is a viable option where sample volume is not limited, such as when sampling ambient air or from a large sample chamber. Increasing the flow rate above the transition point to turbulent flow would change the regime of mass transfer with a new correlation [147]:

$$Sh_x = 0.0296 Re^{\frac{4}{5}} Sc^{\frac{1}{3}} \quad 3000 > Sc > 0.6 \qquad \text{(Equation 21)}$$

Limits on the flow rate imposed by pump pressure, manifold material strength, or flow chocking may not allow this transition, but it does suggest that great gains can be realized by operating under a different mass transfer regime. By examining the correlations developed for heat transfer, it is possible to find the highest mass transfer correlation with a feasible geometry. The most favored geometry is for an impinging jet, Figure 2.1. Generally smaller boundary layers and mixing of the fluid after impinging on the surface make transfer in impinging jets often faster than other geometries. Phase change processes offer a marked advantage in heat transfer, but it is difficult to construct an analogy to phase change for mass transfer processes.

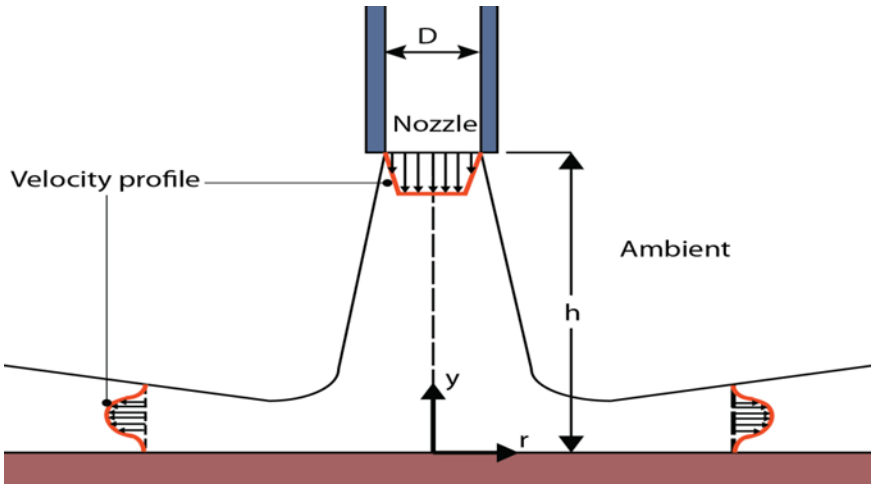

Figure 2.1 Schematic of an impinging jet indicating the momentum boundary layer, though an analogous profile could be drawn for temperature or concentration boundary layers.

Martin [150] recommends the following correlation for an impinging jet:

$$\overline{Sh} = F_1\left(\frac{r}{D}, \frac{H}{D}\right) F_2(Re) Sc^{0.42} \qquad \text{(Equation 22)}$$

where:

$$F_1 = \frac{D}{r} \frac{1 - 1.1D/r}{1 + 0.1(H/D - 6)D/r} \qquad \text{(Equation 23)}$$

D is the diameter of the nozzle and r is the radius from the center line of the nozzle to the edge of the impinged surface. H is the height of the nozzle above the surface.

And where:

$$F_2 = 2Re^{1/2}\ (1 + 0.005Re^{0.55})^{1/2} \qquad \text{(Equation 24)}$$

This correlation is valid for:

$$2000 \leq Re \leq 400{,}000 \quad \text{(Equation 25)}$$

$$2 \leq H/D \leq 12 \quad \text{(Equation 26)}$$

$$2.5 \leq r/D \leq 7.5 \quad \text{(Equation 27)}$$

2.1.2 Adsorption

2.1.2.1 Established adsorption models

Adsorption is the bonding of a species to a surface either through a chemical bond (chemisorption) or a physical bond (e.g., van der Waal forces for physiosorption) [151]. Adsorption is distinct from the separate but related phenomenon of absorption where the species is integrated into the bulk of the material. If both processes are active or if there is ambiguity, the general term sorption is preferred. As a complex yet important process underlying a great deal of sensing techniques, among other fields, adsorption has been the subject of considerable long term study [151][152][153][154].

The key pieces of information sought to describe an adsorption process are the nature of the bond between the adsorbate and the adsorbent and the relationship between surface coverage and the number of adsorbate molecules above the surface. While there is certainly other information that could be gathered in an investigation, these two describe the fundamentals of the system and suggest ways to achieve optimal outcomes for the constraints of the specific application. The nature of the adsorbate-adsorbent bond is often elucidated via a determination of the surface binding energy.

2.1.2.1.1 Adsorption isotherms

The relationship between concentration and surface coverage is usually portrayed via an isotherm. Isotherms are mathematical relations between the concentration, or a related measure like partial pressure, and the percent surface coverage of that species on the surface. These are steady state measurements performed at a set temperature, as they are often quite temperature dependent. A typical isotherm graph is given in Figure 2.2.

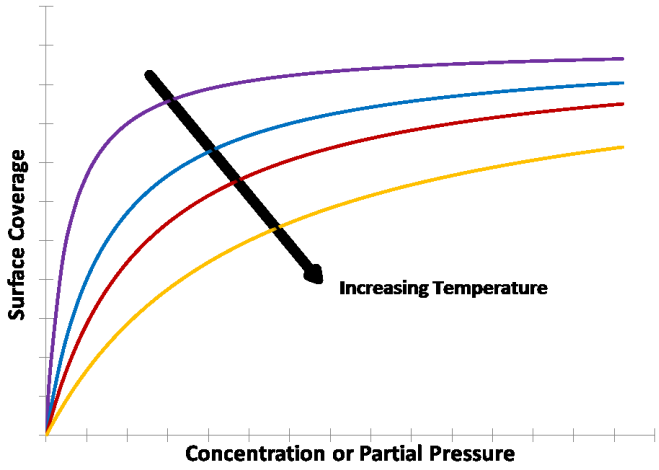

Figure 2.2. A typical adsorption isotherm (These are based on a Langmuir type isotherm; other models would have related but distinct shapes)

The most commonly used isotherm is that of Irving Langmuir (1916) [152]. The described isotherms are based on the assumptions that: 1) adsorption proceeds to a single monolayer; 2) all adsorption events are independent; and 3) all sites are equally available to adsorption events. Solving for the fractional surface coverage, θ, yields the common Langmuir Isotherm Equation:

$$\theta = \frac{C}{1/k_{eq} + C} \qquad \text{(Equation 28)}$$

where C is the concentration and k_{eq} is the temperature dependent equilibrium constant.

In many situations, including the one treated here, it is more convenient to deal with a time dependent equations [155]. If the adsorption and desorption coefficients, k_a and k_d, are constant for a certain temperature then the change in the fractional surface coverage would be given by:

$$\frac{d\theta}{dt} = k_a C(1-\theta) + k_d(\theta) \qquad \text{(Equation 29)}$$

Integrating this equation with the initial condition of zero surface coverage at time zero, yields:

$$\theta(t) = \frac{k_{eq}C}{1 + k_{eq}C}(1 - exp(-k_n t)) \qquad \text{(Equation 30)}$$

with $k_{eq}=k_a/k_d$ and $k_n=k_aC+k_d$.

The variables were reorganized as above for convenience in subsequent curve fitting.

Another commonly used adsorption model is the so-called Freundlich isotherm. It is an empirical model which actually predates the Langmuir isotherm. The model was proposed by Boedecker in 1895 though it was popularized by Freundlich [151]. The equation postulates a power relationship between concentration and surface coverage:

$$\theta = kC^{1/n} \quad \text{(Equation 31)}$$

or in a time dependent form:

$$\theta = A(1 - \exp(k * C^{1/n}t)) \quad \text{(Equation 32)}$$

There are a several other isotherm models that have been successfully applied to a variety of systems, including BET, Frenkel-Halsey-Hill, Polanyi potentials, Temkin, and Dubinin-Radushkevich[154][156]. These models were investigated as being possible candidates for describing the adsorption of mercury vapor onto gold nanoparticles, but they were ultimately not applied here as they were based on assumptions or conditions not fulfilled in this system. These assumptions were multi-layer adsorption, preferential adsorption at grains, sorption on pores, or the requirement for a priori constants not available. Subsequent success describing the system with the models chosen did not necessitate the exploration of these other models.

2.1.2.1.2 Kinetic models

It is common in the field concerning sorption from liquid onto sorbents to investigate the kinetics of the process [153][157] . Kinetic information can be used to help determine the nature of the sorption, rate constants, and saturation conditions. The notation and language of kinetics for sorption process is similar to general chemistry with some distinctions.

A first order[13] kinetic process is generally described as one where the reaction rate is proportional to the concentration of a species:

$$\dot{N} = KC \quad \text{(Equation 33)}$$

In the context of sorption the reaction is usually related to the availability of sites. This was first expressed by S. Lagergren in 1898 [158][159] and from Ho et al. (2000):

$$\frac{dq_t}{dt} = k_1(q_m - q_t) \quad \text{(Equation 34)}$$

[13] A zeroth order rate is constant, $\dot{N} = K$ though that is not very relevant to this work

q_t is the mass sorbed at time t, q_m is the mass sorbed at $t = \infty$, often treated as an experimentally determined parameter, and k_1 is the rate constant [153]. This form applies to both surface adsorption and bulk absorption. Framed in terms of the variables introduced previously and relevant to surface adsorption, the fractional surface coverage is equal to the mass adsorbed at a time t divided by the total mass which can be adsorbed by the surface:

$$\theta = \frac{q_t}{q_m} \qquad \text{(Equation 35)}$$

Dividing the pseudo-first order equation[14] through by q_m, which is constant, yields:

$$\frac{d\theta}{dt} = k_1(1-\theta) \qquad \text{(Equation 36)}$$

The reaction constant k_1 can be replaced by a concentration dependent constant k_a when the concentration is constant (which includes all experiments presented here):

$$\frac{d\theta}{dt} = k_a C(1-\theta) \qquad \text{(Equation 37)}$$

Thus the pseudo-first order kinetic equation is equivalent to a special case of the time dependent Langmuir isotherm where the desorption constant is negligible. Indeed Azizian (2004) has shown that the first order and pseudo-second order (described presently) kinetic equations are special cases of kinetic models being equivalent to the Langmuir isotherm. His general analytical solution is complicated and does not allow for easy fitting for data analysis, and as such was not used further in this work [160][161].

Sorption processes may be modeled by a pseudo-second order equation where the surface coverage is proportional to the square of the available sites [162]. Such a model has been applied to the sorption of various metal ions into bio-sorbents such as peat or leaf mold [153][163][164][165][166].

$$\theta = 1 - \frac{1}{1 + kC^n t} \qquad \text{(Equation 38)}$$

here for a second order mode the exponent n would be equal to 2.

A third kinetic model of some relevance to this work is the Elovich Equation [167] which is included because it was originally applied to chemisorption of gases on solids. It is an empirically derived relationship with two constants describing adsorption and desorption:

[14] The nomenclature pseudo-first order kinetic model is used to distinguish this form based on sorbent capacity from the more general first order model based on concentration, similarly for the pseudo second order model [153].

$$\theta = \frac{1}{\beta}\ln(\alpha\beta) + \frac{1}{\beta}\ln(t) \qquad \text{(Equation 39)}$$

where α is the initial sorption rate constant, and β is the desorption constant [157][168][169].

2.1.2.1.3 Diffusion Models

In addition to the equilibrium models and the kinetic equations, diffusion models have been applied to sorption processes. As Ho et al. [153] describes in their review of pollutant sorption, the process itself can be divided into 4 steps. The first three steps are related to different mass transport processes. First there is bulk transport where target species move from the 'free stream' fluid to the near surface of the sorbent. Second is film diffusion where the target species transports across films or boundary layers that may exist on the surface of the sorbent. The third, and last diffusion stage, is diffusion into pores. Many of these diffusion studies concern high surface area sorbents, such as activated carbon, where transport into, or through, micro-scale pores is important. The fourth and final step involves the kinetics of the surface, the adsorption and desorption of species at the sorbent's surface. Many of the experiments, for example [164][170][171][172][173] [174][175], attempted to minimize the effects of mass transport, especially bulk transport, by stirring or agitation of the sample. If the sample is well mixed, species transport through the first two diffusion steps will be quicker, and if the initial transport is fast compared to surface reaction then the kinetics, or the pore diffusion if applicable, can be considered the limiting step. The stirring and agitation is an attempt to make the later stages of the process the limiting phenomena, an approach seldom validated quantitatively, and bulk transport will still occur even if not rate limiting [153]. Attempts have been made to account for the diffusion across films and through pores.

Several works represented film diffusion as an exponential [153][157][171]. This representation is based on work by Boyd et al. (1947) who approximated the sorbent particles as a sphere and applied Fick's Diffusion Law to approximate the mass transfer rate. Integrating the differential equation yields [176]:

$$\theta = 1 - \exp(-K_{fd}t) \qquad \text{(Equation 40)}$$

The above equation has been reformatted for consistent variables, K_{fd} is a constant related to the diffusion coefficient of the analyte through the fluid. That film diffusion and several of the kinetic equations have similar mathematical forms, highlights the difficulty in separating the two, especially if the assumption of 'fast mixing rates' is not warranted. Occasionally a double exponential model is used to attempt to disambiguate multiple rate limiting steps such as diffusion and sorption:

$$\theta = 1 - A_1\exp(-k_{d1}t) - A_2\exp(-k_{d2}t) \qquad \text{(Equation 41)}$$

where A_1 and A_2 are separate constants and k_{d1} and k_{d2} are rate constants. While numerically simple this could be just a convolution of a 1st order reaction and may not result in any novel information.

For diffusion through a pore of sorbent a relationship developed by Weber and Morris is most commonly used [153][177][178]:

$$\theta = K_d\sqrt{t} \quad \text{(Equation 42)}$$

where K_d is a diffusion constant.

2.1.2.1.4 Adsorption energy

The nature of the bond leading to sorption is often partially elucidated by measuring the adsorption energy. The most typical formulation is the Gibbs Adsorption Energy, the standard result for which is reviewed here.

Assuming the adsorption reaction is of the form:

$$v_A A + v_B B \Leftrightarrow v_{AB} AB \quad \text{(Equation 43)}$$

Where v stands for the stoichiometric coefficients and A, B, and AB stand for the adsorbate species, the bulk and the combined adsorbed species on the bulk. Of course, there would be adsorbate and bulk molecules which do not react, though they would cancel out from both sides of the reaction.

The Gibbs free energy is defined as:

$$G \equiv H - TS \quad \text{(Equation 44)}$$

Taking the derivative in terms of a species, in this case A, at a constant temperature and pressure:

$$\left(\frac{dG}{dn_A}\right)_{T,P,n_B} = \left(\frac{dH}{dn_A}\right)_{T,P,n_B} - T\left(\frac{dS}{dn_A}\right)_{T,P,n_B} \quad \text{(Equation 45)}$$

This equation can be reformatted as below for convenience, as each term satisfies partial molal properties:

$$\bar{G}_A = \bar{H}_A - T\bar{S}_A \quad \text{(Equation 46)}$$

As there is no change in pressure or temperature, an assumption for dilute mixtures, the enthalpy will be the same:

$$\bar{H}_A = \bar{h}_{A0} \quad \text{(Equation 47)}$$

where $\bar{h}_{A0}$ is a standard state value at the specified temperature and pressure.

The partial entropy of the species A is a function of the partial pressure of the species:

$$\bar{S}_A = \bar{s}_{A0} - R \ln\left(\frac{y_A P}{P_0}\right) \quad \text{(Equation 48)}$$

Substituting into (Equation 46:

$$\bar{G}_A = \bar{g}_{A0} + RT \ln\left(\frac{y_A P}{P_0}\right) \quad \text{(Equation 49)}$$

The same would be true for each species in the equation and the entire derivative of free energy, at the specified temperature and pressure for the reaction, would be given by:

$$dG_{TP} = \bar{G}_{AB} dn_{AB} - \bar{G}_A dn_A - \bar{G}_B dn_B \quad \text{(Equation 50)}$$

where dn_i is defined as the change in moles of the ith species, which can be rewritten as:

$$dn_i = v_i d\varepsilon \quad \text{(Equation 51)}$$

The change in the moles of the ith species is equal to the stoichometeric coefficient times the degree to which the reaction proceeded, $d\varepsilon$. Thus

$$dG_{TP} = (v_{AB}\bar{G}_{AB} - v_A\bar{G}_A - v_B\bar{G}_B)d\varepsilon \quad \text{(Equation 52)}$$

Substituting in

$$dG_{TP} = \left[v_{AB}\left(\bar{g}_{AB0} + RT\ln\left(\frac{y_{AB}P}{P_0}\right)\right) - v_A\left(\bar{g}_{A0} + RT\ln\left(\frac{y_A P}{P_0}\right)\right) - v_B\left(\bar{g}_{B0} + RT\ln\left(\frac{y_B P}{P_0}\right)\right)\right] d\varepsilon$$

(Equation 53)

The change in free energy for the reaction proceeded to completion as defined by the stoichiometric coefficients:

$$\Delta G_o = v_{AB}\bar{g}_{AB0} - v_A\bar{g}_{A0} - v_B\bar{g}_{B0} \quad \text{(Equation 54)}$$

Since the reaction proceeded to equilibrium when $dG_{TP} = 0$,

$$\Delta G_0 = -RT \ln\left(\frac{y_{AB}^{v_{AB}}}{y_A^{v_A} y_B^{v_B}}\left(\frac{P}{P_0}\right)^{v_{AB}-v_A-v_B}\right) \quad \text{(Equation 55)}$$

It is convenient to define the term inside the logarithm as the reaction coefficient at equilibrium K_{eq}[15].

$$K_{eq} = \frac{y_{AB}^{v_{AB}}}{y_A^{v_A} y_B^{v_B}} \left(\frac{P}{P_0}\right)^{v_{AB}-v_A-v_B} \quad \text{(Equation 56)}$$

$$\Delta G = -RT \ln K_{eq} \quad \text{(Equation 57)}$$

Often a Classius-Claperyron type equation is used to calculate the enthalpy of adsorption, with C_2 the equilibrium concentration:

$$\left(\frac{d \ln C_2}{dT}\right)_n = -\frac{\Delta H}{RT^2} \quad \text{(Equation 58)}$$

Several experiments have measured heats of adsorption experimentally, though the exact quantity described depends on the experimental conditions.

For isothermal conditions the adsorption of a fixed quantity of adsorbate, the total heat, Q, is often referred to as the integral heat of adsorption. By plotting, or otherwise, the change in Q as the number of molecules changes it is possible to determine the differential heat of adsorption q. A second term, the isosteric heat of adsorption, is calculated from the Classius-Calperyron Equation. The isosteric heat of adsorption is related to the differential heat of adsorption by the subtraction of an RT term, representing the energy of the approximated ideal gas, leaving the area above the solid [151][154] .

2.1.2.2 Review of previous work on adsorption

Previous work examined the adsorption kinetics of gold and gold colloids. Work reviewed in the introduction, such as Levlin et al. (1999) [128] or Morris et al. (2003) [179], investigated the morphological changes of gold surfaces after the sorption of mercury. While yielding valuable information about the structure and binding of mercury to gold surfaces, they did not have the time resolution in their methods to interrogate the kinetics or binding energy. Other work employing either plasmon resonance measurements or quartz crystal microbalances has been able to interrogate the adsorption kinetics.

[15] This is the same as the equilibrium reaction coefficient for an ideal gas reaction, based on partial pressures.

Karpovich and Blanchard (1994) used a quartz crystal microbalance (QCM) to investigate the kinetics and energy of adsorption of alkanethiolates (1-$C_{18}H_{37}SH$ and 1-$C_8H_{17}SH$ or 1-octadecanethiol and 1-octanethiol) on gold thin films. QCM have a resonant frequency which is very sensitive to the mass loaded on it. By measuring the change in the resonance frequency it is possible to extrapolate the mass deposited on the sensor. The adsorption of alkanethiolate from an organic solution to the gold coated QCM was performed in a 100 ml temperature controlled and agitated beaker. Thiol groups (-SH) have a well-established affinity for gold and will tend toward a monolayer, as evidenced by their fitting of a Langmuir type isotherm to the QCM frequency shift (Figure 2.3).

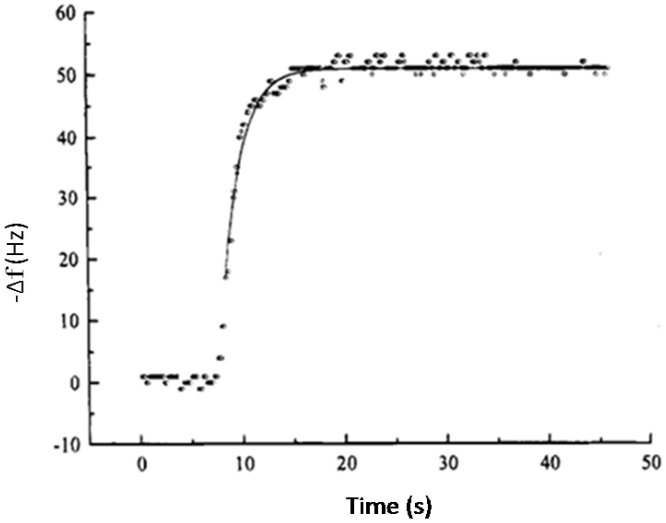

Figure 2.3. Shift in resonance frequency for alkanethiolate on gold coated QCM. Points are raw data; the solid line is the Langmuir isotherm. From [155].

They also calculated the free energy of adsorption of the various combinations tested, finding it to be between 4 and 6 kcal/mol [155].

Sabri et al. (2011) extended the use of QCM to investigate the adsorption of mercury on gold films. They investigated vapor phase deposition of elemental mercury onto gold films by monitoring the change in resonance frequency of the QCM. A temperature controlled permeation tube supplied mercury in a nitrogen flow to a 0.5 L exposure chamber at a constant 0.2 LPM. Though not explicitly mentioned, it is implied that the entire chamber was maintained at a constant temperature. No mention of mass transfer effects or the chamber geometry is given. The QCM were exposed to increasing concentrations of mercury from 1 mg/m^3 to 10 mg/m^3 in sequence with a 1 hour period of clean nitrogen flow. They fit the data to a rational polynomial function and gave results for 'sticking probability[16]' as a function of time at different temperatures. The experimental differences make it difficult to compare directly, the relationship of adsorption and sticking probability with time; though, the relationship roughly corresponds to the relationship observed in our experiments.

[16] Sticking probably is the ratio of atoms sorbed to the atoms which strike the surface [180][181]. It is related to the change in surface coverage, θ, over the atomic flux to the surface.

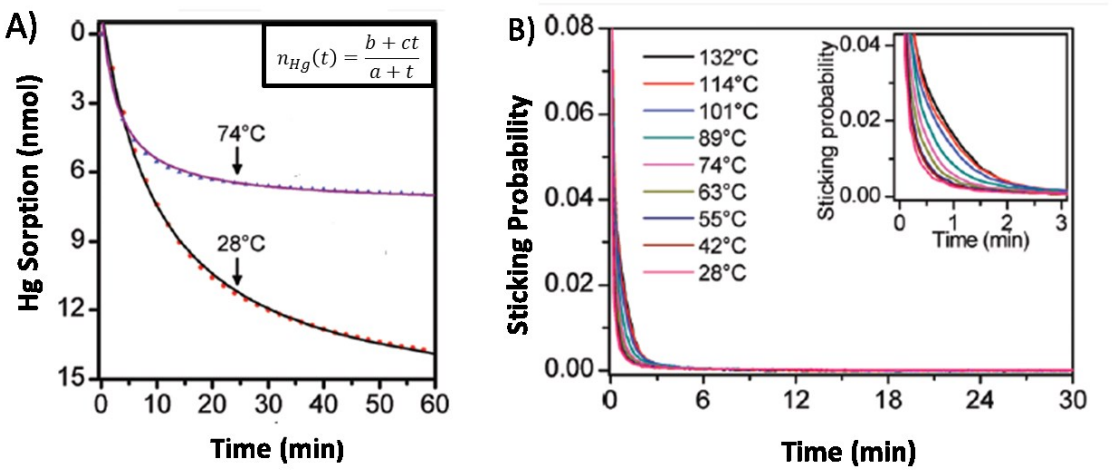

Figure 2.4. Mercury sorption and sticking probability on gold films at various temperatures. Data in A) is fit to a rational polynomial of the form in the insert. Adapted from[180].

In addition, they found that adsorption is favored by rough gold surfaces, and lower temperatures, which may have some bearing on sensor design [180].

Eck et al. (2000) used the plasmon resonance of colloidal gold in solution to measure the real time adsorption of biopolymers onto the gold nanospheres; biopolymers (gelatin) were chosen based on the interest in nanoparticles as biosensors and the historical observation of Faraday that an 'animal substance' caused a shift in color of his gold solutions. The particles were 15 nm spheres in an aqueous solution. They were able to measure the depletion of the biopolymer from the solution by means of fluorescent labeling. The amount of polymer adsorbed over time followed a Langmuir type isotherm from which they calculated an adsorption energy of 5.5 kJ/mol.

They also fitted the initial shift in peak location to the film model for diffusion, though their calculated diffusivity, 1.25×10^{-12} m^2/s, was an order of magnitude lower than the diffusivity of either the gold colloid (2.79×10^{-11} m^2/s) or the gelatin (1.05×10^{-11} m^2/s).

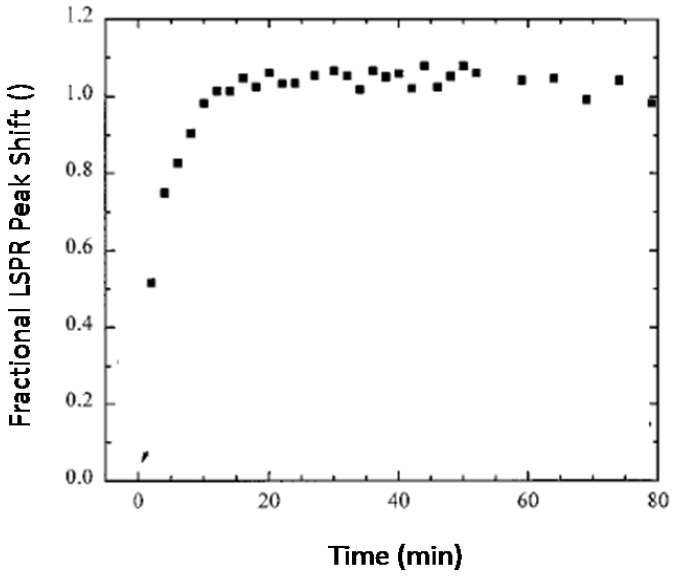

Figure 2.5. Fractional LSPR peak shift for polymer adsorption onto gold nanospheres. Data was fit to a Langmuir type isotherm (not shown). From [182].

The slower diffusion was attributed to an electrostatic barrier between the polymer and the gold since both species are negatively charged [182].

The preceding three studies and the previous work on absorption, cited in the introduction, suggest that a need exists to investigate the adsorption kinetics of the mercury adsorption on gold nanoparticles, and that measurements utilizing the LSPR peak provide a means to accomplish this. Additionally, the flexibility afforded by vapor studies in air allows a variety of flow rates and geometries to be investigated.

2.2 Adsorption of mercury on gold nanospheres

2.2.1 Experimental methods

To investigate the adsorption of elemental mercury, vapor was directed through an impinging flow nozzle onto gold nanospheres deposited onto a quartz substrate. The optical response of the nanoparticle was measured with a spectrometer. This response was used to elucidate the adsorption mechanics. Details of the experimental methods and results follow.

2.2.1.1 Substrate preparation

Previous work established the suitability of gold nanospheres for use as a mercury sensor, and found that the sensitivity of the sensor scaled with the surface area to volume ratio [138]. 4-tert-butylthiophenol functionalized gold nanospheres suspended in toluene were purchased from Sigma-Aldrich. The particles are nominally 5 nm but were measured by TEM to be between 3 nm and 4 nm. These were the smallest commercially available nanoparticles in an organic solvent which were functionalized with a thiol group and had a peak in the visible. The thiol group was preferred for adherence to the silicon oxide substrates. Deposition onto the quartz substrate was accomplished by Langmuir-Blodettry, a procedure which allows control over the density of deposition by controlling the surface pressure of the film of nanoparticles suspended in chloroform, a non-polar solvent. The chloroform/nanoparticle layer floats on a trough of water and the surface pressure is controlled by means of a mechanical arm. In this case the pressure was 15 mN/m, leading to an evenly dispersed monolayer. The monolayer coverage was verified by examination of a silicon nitride grid by TEM which was dipped simultaneously with the substrates used as mercury sensors. More details of this method can be found in [138].

A subset of the finished chips was exposure to an oxygen plasma for 10 minutes to remove the organic surface coating and clean the surface.

A separate procedure derived from Vakarelski et al. [183] created a gold nanoparticle coated quartz slide by layer by layer deposition, or LBL, using nominally 10 nm diameter citrate coated nanoparticles purchased from Ted Pella. Slides were cleaned in 2M NaOh, rinsed in Millipore water, and then further treated in 1:1:5 by volume H_2O_2 to $NH_{3(aq)}$ to H_2O. Slides were then immersed in 1% w/w polyethylenamine, or PEI, (Sigma-Aldrich 25,000 MW) to water. After one hour slides were double rinsed in Millipore water and then immersed in nanosphere solution, as delivered. Slides could be double rinsed again, and the process repeated as many times as desired. A 2x process, twice in the PEI and twice in the nanospheres, provided a good balance between absorbance and aggregation.

2.2.1.2 Exposure procedure

The results from the mass transfer correlations, previously described, led to the choice of an impinging flow apparatus. The impinging geometry provides the highest mass transfer rate for a given flow rate. We mounted the gold nanoparticle decorated substrate on a mirrored surface

by means of a silicon adhesive. The mirror provides a reflective surface to direct the path of the light from the source to the spectrometer. The spectrometer provided absorbance measurements of the light as the mercury was adsorbed onto the gold nanoparticles. A diagram of the apparatus is shown in figure 6.

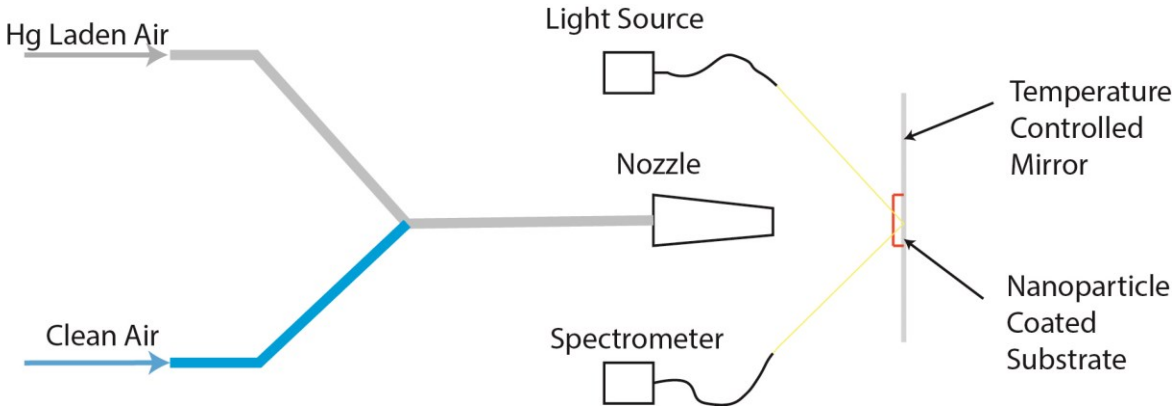

Figure 2.6 Exposure apparatus. Figure is not to scale. Relevant dimensions are given in Table 2-6. The location of collimating lens, not labeled, is at the transition point between the fiber optic cable, black line, and the light beam, straight yellow line. They have a focal length of 10mm.

The light source was a DH-BAL 2000 (Ocean Optics) equipped with both halogen and deuterium bulbs. The light was coupled to 600 µm fiber optic cables terminating in a collimating lens to focus the light on the slide. The reflected light was coupled back into a second 600µm fiber optic cable via a second collimating lens. This fiber optic cable terminated at an Ocean Optics QR9000 spectrometer with a resolution of 0.8 nm in the 200 nm to 1000 nm range. The spectrometer was controlled and data collected through the Spectra Suite Ocean Optics software package running on a PC.

A lab-built dehumidifier and filter cleaned and dried the house air. This clean dry air was provided to a PSAnalytical Calibration Kit, or CavKit, which maintained a mercury impregnated solid at a fixed temperature and supplied a saturated mercury vapor stream. This stream was mixed with clean dry air to provide the desired mercury vapor concentration.

The nanoparticle coated substrates were attached to a 1st surface aluminum mirror from Edmunds Optics. The mirrors had a reflectivity of greater than 90% in the visible range, and surface roughness was between 1.8 and 5 microns. The mirror was held in an optical mount holding the substrate fixed but allowing it to be raised and lowered into the light beam. The back side of the mirror was connected to heat tape controlled by a Variac transformer. The heat tape was used to raise the temperature of the gold nanoparticles above 373 K, the temperature which previous work and initial experimentation had determined was suitable for regenerating the sensor by desorbing the mercury [138].

During the exposure procedure, each slide was initially heated to 373 K. After being held at the elevated temperature for a minimum of 20 minutes the slides were allowed to cool to room temperature slowly, as increasing the cooling rate could crack the glass backing of the mirror. The cooling rate was determined by natural convection and took approximately 30 minutes to cool from 373K to room temperature. After returning to room temperature, clean dry air at the desired flow rate impinged on the slide. At this point the slide was moved out the light beam so background spectra could be taken. The background spectra are used to calculate the optical absorbance and include a 'light spectrum' of the light source reflected off the clean mirror into the spectrometer and a dark spectrum with the light source off. Optical absorbance spectra were calculated by:

$$\alpha(\lambda, t) = -\log\left(\frac{I_s(t) - I_D}{I_L - I_D}\right) \qquad \text{(Equation 59)}$$

Where $\alpha(\lambda, t)$is the absorbance at a specified wavelength (λ) and time (t), and $I_S(t)$, I_L and I_D are the sample intensities at time t, the light intensity, and the dark intensity respectively, all at the specified wavelength. The spectra that are a function of time are collected continuously during the course of the experiment, as detailed below. The light and dark spectra remain constant throughout each run.

The slide was returned to the light beam, and an absorbance spectrum was recorded every 5 seconds. This spectrum was the average of at least 30 separate spectra taken with a 100 ms integration time. Integration times of 100 ms provided sufficient intensity for a determination of the LSPR peak. The averaging of 30 spectra helped reduce the noise. Both of these choices were constrained by the desire to have as high a time resolution as possible. It should be noted that there was some variability in the time of each spectra's recording, i.e. they were not all at 5 s intervals. Some were as low as 3 s and some as high as 12 s. This variability was attributed to small bugs in the coding of Spectra Suite. If a constant 5 s was assumed for subsequent analysis, error would be introduced. This error was mitigated by reading the time stamp of each spectrum's file individually thus recording the actual time difference between each absorbance spectrum.

The system was run with clean dry air at a fixed flow and spectra were recorded until the location of the LSPR peak did not vary more than random noise within 0.5 nm. This process normally required at least 30 minutes. Then, the valve on the CavKit was the opened, exposing the sensor to the desired concentration of mercury at the same flow rate. This flow rate is generally stable, though it was monitored and small adjustment were made as required by pressure fluctuations. The CavKit is configured to continually exhaust its flow to a waste stream; this avoids a spike of high concentration mercury upon actuation of the valve. The exposure was run until the gold surface saturated and the LSPR peak stopped shifting, at least 90 min. Saturation was also verified after the experiment by examining the trace of the LSPR peak with time, Figure 2.9.

2.2.2 Result

Table 2-2 gives the summary of tests conducted with this geometry in order to investigate the kinetics, thermodynamics, and mass transfer effects of mercury adsorbing on gold nanoparticles.

Table 2-2. Summary of impinging flow tests. Flow rate and concentration are corrected via a pressure reading[17]. LB refers to the Langmuir Blodgett and LBL refers to a LBL deposition. Bare particles have been plasma cleaned and coated particles retain their original coating from synthesis.

Particle Type	Date	Run	Corrected Hg Conc. (µg/m3)	Corrected Air Flow (LPM)	Initial LSPR (nm)	Final LSPR (nm)
LB-Bare	26-Jul	1	3	20	527.3	512.6
LB-Bare		2	3	20	518.8	511.3
LB-Bare		3	3	20	519.2	513.2
LB-Bare	27-Sep	1	8	25	519.9	514.9
LB-Bare	24-Sep	1	4.2	25	519.0	513.0
LB-Bare		2	4.2	25	505.8	502.4
LB-Bare		3	4.2	25	512.5	508.1
LB-Bare	1-Oct	1	3	10	530.5	525.6
LB-Bare		2	3	10	521.7	518.0
LB-Bare		3	3	10	531.9	526.0
LB-Bare	4-Oct	1	5	5	531.6	525.5
LB-Bare			5	5	513.5	507.0
LB-Bare	5-Oct	1	33	25	538.3	531.8
LB-Bare		2	33	25	538.5	532.3
LB-Coated	28-Jan	1	3	20	526.0	517.5
LB-Coated		3	3	20	518.3	512.2
LB-Coated	31-Jan	1	3	20	512.8	515.8
LB-Coated	29-May	1	8	10	517.0	511.3
LB-Coated		2	8	10	511.3	507.8
LB-Coated	1-Jun	1	8	2	516.5	513.9
LB-Coated		2	8	4	514.7	511.7
LBL	18-Nov	1	3	20	542.5	536.7
LBL		2	3	20	538.0	533.0
LBL	19-Nov	1	3	10	551.8	549.4
LBL		2	3	10	552.1	549.1
LBL	25-Nov	1	20	20	544.3	541.2
LBL		2	20	20	543.2	540.6

[17] The flow rate was measured with a rotometer calibrated at atmospheric pressure. At the elevated pressure, 20 psig, of the exposure line it is necessary to correct the nominal volumetric flow by [184]:

$$\dot{V}_A = \dot{V}_G \sqrt{\frac{P}{(101kPa)} \frac{(294K)}{T}}$$

Where P is the actual pressure in kPa, T is the actual temperature in K. $\dot{V}_G$ is the flow rate reading from the meter, and V_A is the actual flow rate. The concentration is corrected by dividing the mass of mercury by the corrected flow rate.

The initial and final LSPR refer the peak location before the introduction of mercury and after saturation; an example is portrayed in Figure 2.7.

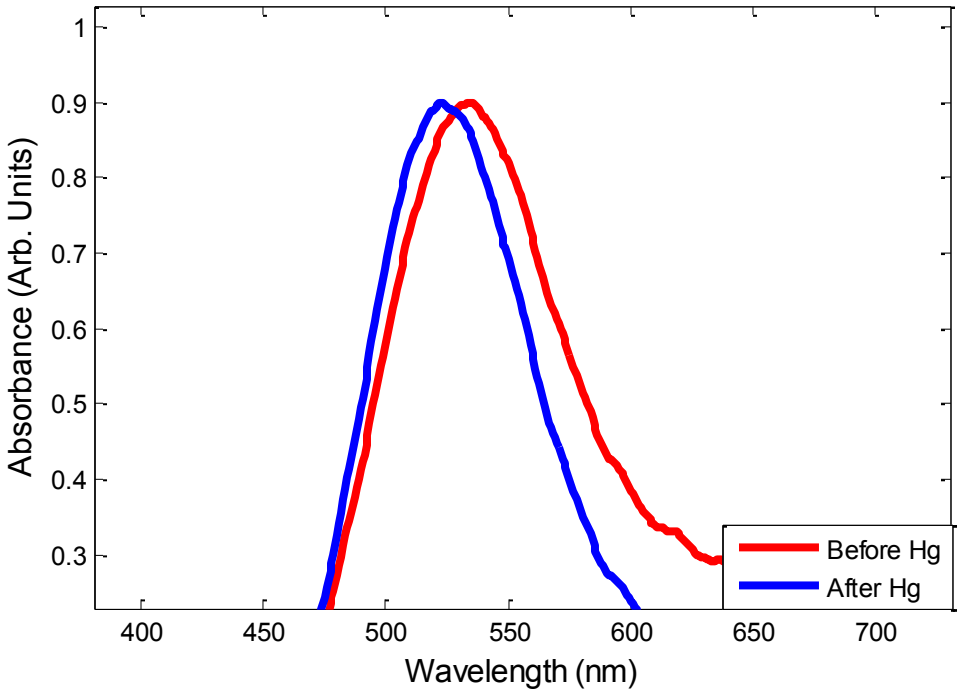

Figure 2.7. Optical absorbance spectra for sample Oct 5-1 before and after exposure to 33 µg/m^3 at a flow rate of 25 LPM. 200 spectra, representing 10 min, have been averaged and normalized to reduce noise and increase clarity. Individual spectra are taken over shorter integration times to increase time resolution at the expense of increased noise.

The peak location is determined by fitting the spectrum with a Lorentz Function:

$$\alpha(\lambda) = \frac{A'}{B'^2 + \left(\lambda - \lambda_p\right)^2} \qquad \text{(Equation 60)}$$

where $\alpha(\lambda)$ is the absorbance at a wavelength, λ; λ_p is the LSPR peak; and A' and B' are fitting constants.

The Lorentz function, also known as the Cauchy distribution, was chosen as its form closely matched the Mie dipole approximation for the extinction, a theoretical model commonly used for the absorbance of nanoparticles.

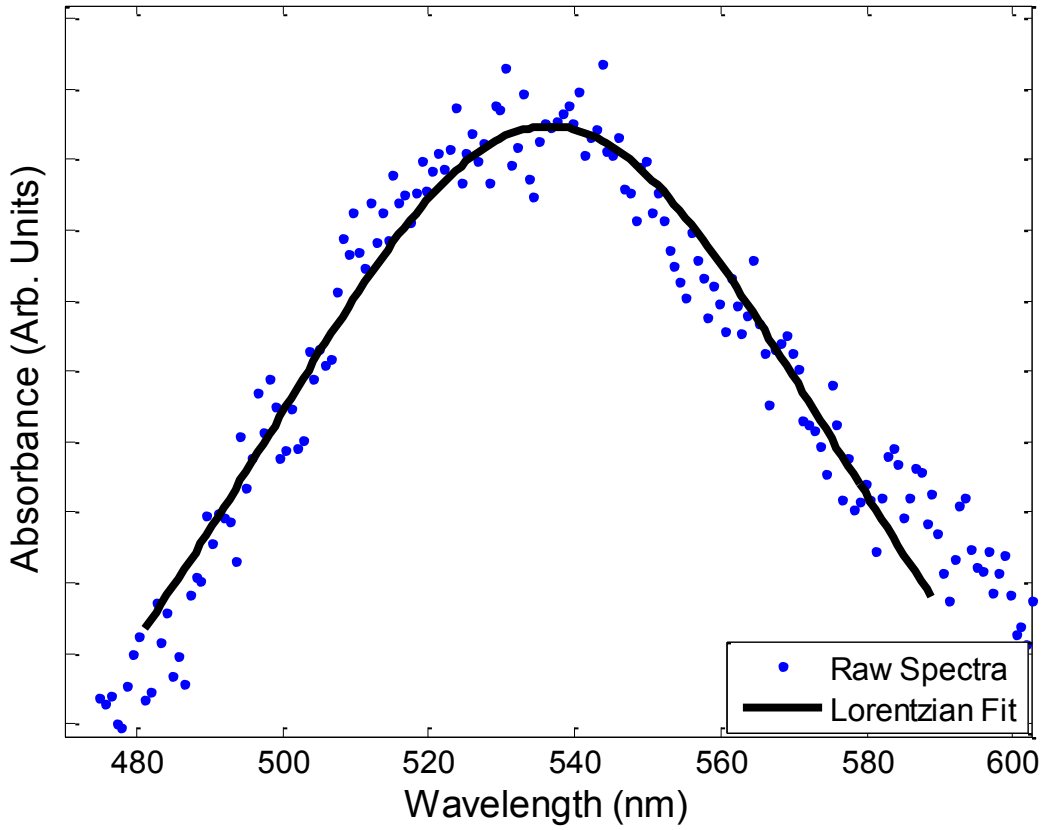

Figure 2.8. Example of Lorentz Function curve fit. The data is for the spectra right at introduction of Hg for test 1 from Oct 5.

This peak location over time is the data which is tracked for each run and which is used for subsequent processing and curve fitting. An example of the curve is given in Figure 2.9.

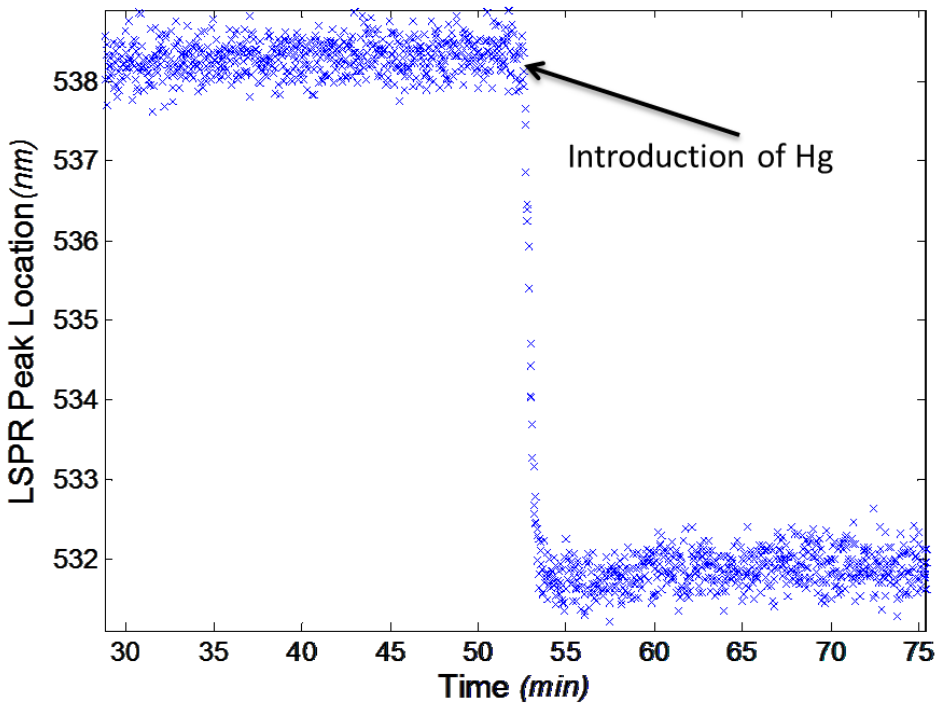

Figure 2.9. LSPR peak location over time. The introduction of Hg, recorded externally, is indicated. The data is for test 1 from Oct 5.

2.2.3 Application of adsorption models to data

To determine which adsorption model best corresponded to the data, a variety of models were fit to the data after introduction of mercury, using a Matlab computer program which utilized a least squares minimization scheme. The fit of a Langmuir isotherm is shown in Figure 2.10.

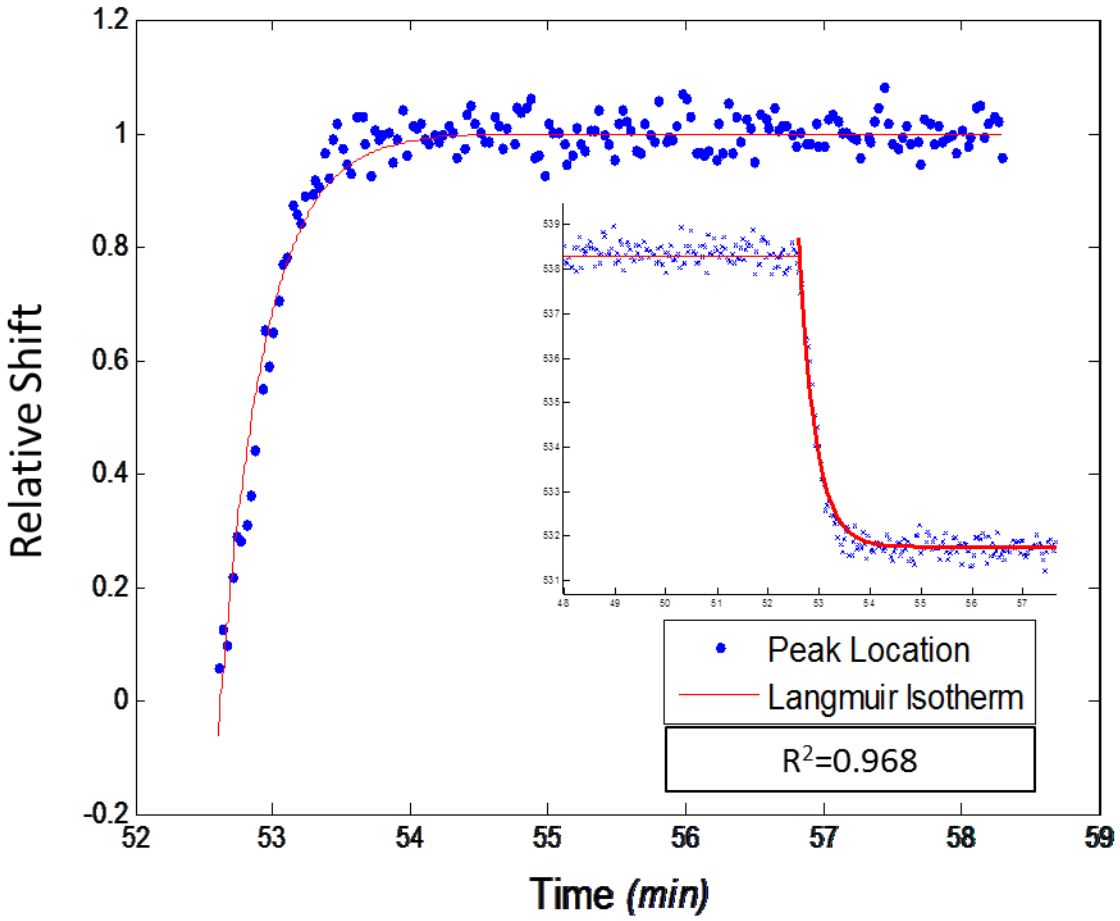

Figure 2.10. Fitting the normalized peak shift to a Langmuir isotherm. Insert is plot on original peak data.

These curve fittings assumed that the initial LSPR peak wavelength before the addition of mercury corresponded to the filling of zero available sites and that the final wavelength after saturation corresponded to complete filling of available sites. In effect the complete LSPR shift was assumed to correspond to θ=0 to θ=1, and normalized accordingly, as shown in the insert in Figure 2.10.

Other non-Langmuir models were applied and found to be poorer representations of the data as evidenced by the R^2 values presented in Table 2-3.

Table 2-3. Comparison of mean R^2 of different absorbance models fit to data

	Langmuir/ First Order	Freundlich	2nd Order	Nth Order	Elovich	Film Diffusion	Double Exponential
Average Uncoated	0.966	0.965	0.832	0.788	0.836	0.461	0.965
Average Coated	0.981	0.980	0.859	0.731	0.959	0.873	0.981
Average LBL	0.958	0.958	0.886	0.866	0.892	0.706	0.962

The pseudo-first order, or Lagergren type model, did fit the data well, but this model has been shown to be equivalent to the kinetic Langmuir model. A double exponential model tended to have a good fit, but essentially duplicated the data of the 1st order fit by splitting nearly identical exponents into separate terms, i.e. Ae^x+Be^x, where x is the same to several significant figures. The Freundlich model provided equivalently good fits, though it too essentially duplicates the form of the Langmuir isotherm with the addition of an exponent for which there was no theoretical basis for inclusion.

From this analysis, it was determined that the Langmuir/pseudo-first order kinetic model was the best fit available, which is in some agreement with prior work [128][129][127]. That work established that mercury adsorption proceeds towards a sub monolayer until available sites are full which is consistent with the assumption upon which the Langmuir model is based. Additionally, the adsorption constant was orders of magnitude higher than the desorption constant, again corresponding to prior observation of limited desorption at near room temperatures. Desorption does become significant at relatively modest temperatures, near 373K, as evidenced by the success with regenerating sensors. This evidence provided justification for the decision to neglect the desorption constant for ambient temperature experiments.

This model did not, however, adequately address the concerns of mass transfer. It is clear from prior work, observations, and the previously presented models that the flow rate will impact the transfer of Hg to the surface and thus the sensor's response time. Hence, there was a need for a framework which had the potential to decouple the response due to mass transfer and the response due to surface kinetics.

2.3 Combined mass transfer and surface kinetics model

Table 2-4: Variables used in adsorption models.

Variable	Symbol	Units
Fractional surface coverage	θ	[]
Concentration	C	µg/m^3
Equilibrium constant	k_{eq}	m^3/µg
Adsorption constant	k_a	m^3/sµg
Desorption constant	k_d	s^{-1}
Adsorption time constant	k_n	s^{-1}
Mass sorbed at time (t)	q_t	ng or moles
Mass sorbed at infinity	q_m	ng or moles
First order rate constant	k_1	s^{-1}
Film diffusion constant	K_{fd}	s^{-1}
Pore diffusion constant	K_d	s$^{-1/2}$
Mass transfer resistance	R_D	s/m^3
Proportionality constant	κ	m
Diffusion constant	$\mathfrak{D}$	m^2/s
Mass flux	$\dot{m}$	µg/s
Concentration at surface	C_S	µg/m^3
Pseudo-capacitance	P_C	s^{-1}
Ambient (or free stream) concentration	C_{amb}	µg/m^3
Concentration within nanoparticle (set to zero)	C_o	µg/m^3
Normalization constant	A	µg^{-1}
Time constant normalization	B	m^3/s
Complete capacitor charge	Q_m	coulombs
Capacitor charge at time t	Q_t	coulombs
Proportionality constant	K	s^{-1}

2.3.1 Theoretical background (RC circuit analogy)

To deconvolve the effects of mass transfer and surface kinetics, a framework is developed based on a circuit analogy, a common technique in the field of heat transfer. This 'Equivalent Thermal Circuits' approach then allows the full range of established mathematical tools (e.g. Kirchhoff's Law, Ohm's Law, resistor summing rules, etc.), to be used to solve the problem. The theoretical basis for this approach is due to the similarities between both systems. A voltage or

temperature potential drives an electric or heat current over an electric or thermal resistor, as illustrated in Figure 2.11.

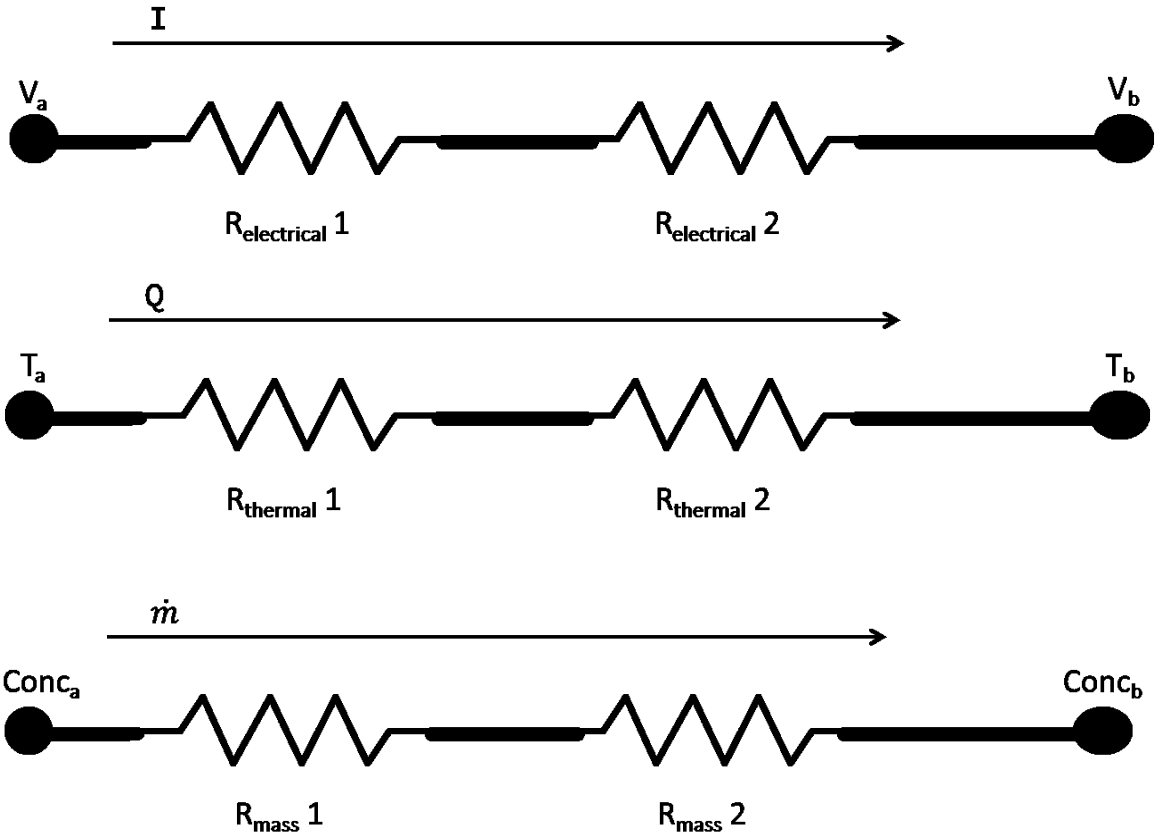

Figure 2.11. Thermal circuit analogy, with mass transfer analogy

This well-established problem solving technique is less commonly applied to mass transfer problems, though the heat transfer analogy is still valid. In this case the potential is provided by the concentration gradient of a species. The current is the mass flow of the species over a resistance to that mass transfer. Resistance is naturally occurring due to the particular circumstance of the mass transfer, such as diffusion, convection, or distance, also portrayed in Figure 2.11.

This analogy can be applied to the system presented in this work, mercury vapor adsorption on gold nanoparticles. Concentration in the ambient, or free stream, is variable based on testing conditions. The effective concentration within the nanoparticles, the second boundary for the system, is assumed to be zero. The resistance to mass transfer arising from the transport from the nozzle to the surface of the nanoparticle is given by R_D such that:

$$R_D = \frac{1}{\kappa \mathfrak{D}} \qquad \text{(Equation 61)}$$

where $\mathfrak{D}$ is the diffusion constant of mercury in air and κ is a proportionality constant related to the flow and geometry. This resistance is the inverse of the mass transfer coefficient determined previously for the system, normalized by the area.

The second element in the circuit analogy for this system would be a resistance that represents the barrier to transport imposed by the adsorption of particles on the surface. From the investigation of the adsorption isotherms presented previously, it is assumed that the adsorption kinetics are most closely modeled as a pseudo-first order reaction. Based on the previous isotherm investigation and prior work with gold adsorption near room temperature [128][129][127][185], the desorption constant is assumed negligible. This facilitates a more compact analytical treatment, the equation for which is given below:

$$\frac{dq_t}{dt} = k_a C_s (q_m - q_t) \qquad \text{(Equation 62)}$$

where C_S is the concentration at the surface. The mass transfer rate is equal to the change in the number of free sites such that:

$$\dot{m} = \frac{dq_t}{dt} = k_a C_S (q_m - q_t) \qquad \text{(Equation 63)}$$

The second element, which represents the resistance to mass transfer caused by the adsorption kinetics, behaves less like a traditional Ohmic resistor and more like a capacitor. Electrical capacitance is defined as the proportionality constant between voltage across a capacitor and its charge. However, here the proportionality constant relates free sites and mass flux through the surface. If it were to be reframed in terms of electricity, the current (i), at a fixed voltage, is proportional to the amount of charge which can yet be added to the capacitor:

$$i = \frac{dQ_t}{dt} = K(Q_m - Q_t) \qquad \text{(Equation 64)}$$

where K is a proportionality constant; Q_m and Q_t are the charge at the capacitor when fully charged and at time t respectively, all at a fixed voltage. This is distinct from a true capacitor where current is proportional the changing voltage over the capacitor, and the capacitor can hold as much charge as the voltage difference can support. The surface in this system can only adsorb as many atoms as there are sites for regardless of the concentration. Thus for clarity and to emphasize this distinction, I will refer to the element representing adsorption kinetic resistance as a pseudo-capacitor, P_C, where:

$$P_C = k_a C \qquad \text{(Equation 65)}$$

A schematic of the system as defined is given in Figure 2.12.

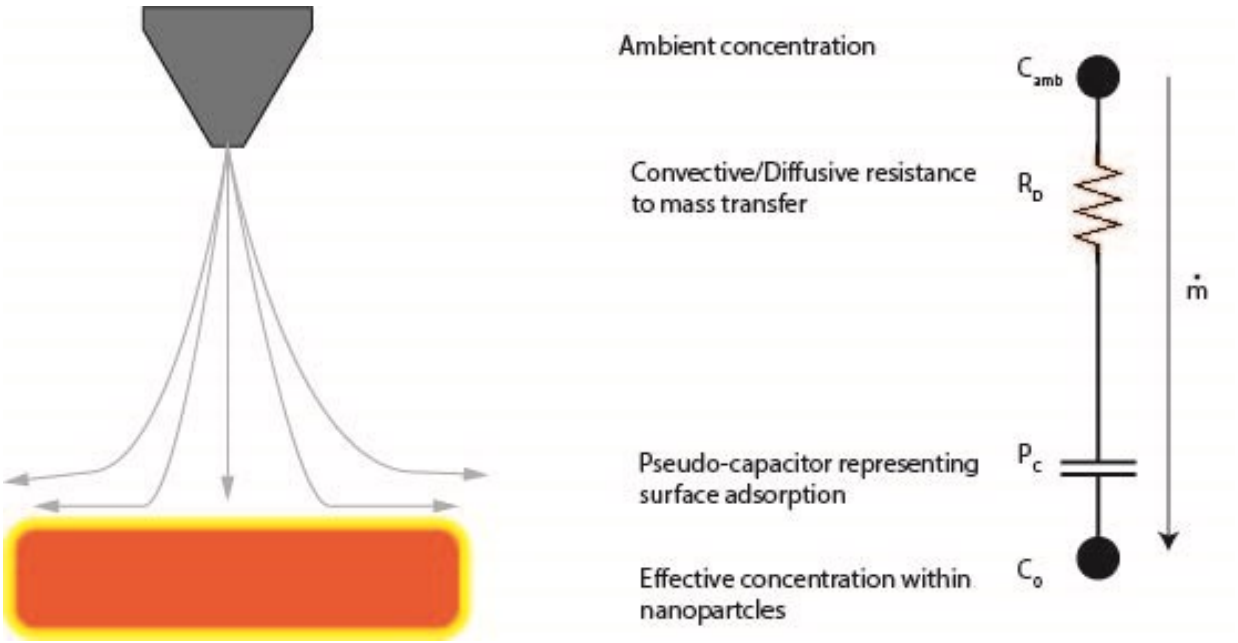

Figure 2.12 Resistor-capacitor circuit analogy for gold nanoparticle based mercury sensor.

The benefit of this approach, beyond the conceptual clarity provided, is that it allows the considerable tools developed to deal with circuits to be applied to this situation. The mass transfer is given by:

$$\dot{m} = \frac{C_{amb}}{R_c} e^{-t/R_D B P_C} \qquad \text{(Equation 66)}$$

were B is a fitting parameter to convert the product of the diffusive resistance and the pseudo-capacitance into a time constant.

Integrating from zero to time t would lead to the number of sites filled at time t:

$$\mathrm{q_t} = B P_C C_{amb} \left[1 - e^{-t/R_c B P_C}\right] \qquad \text{(Equation 67)}$$

However, the response recorded is not number of sites, but the location of the LSPR peak, Γ. Thus a constant is introduced to relate the number of sites filled to the location of the peak:

$$\Gamma = A q_t \qquad \text{(Equation 68)}$$

where A is the constant relating LSPR peak to mercury site adsorption. The combined time response for the LSPR peak is given by:

$$\Gamma = ABP_C C_{amb}\left[1 - e^{-t/R_c BP_C}\right] \qquad \text{(Equation 69)}$$

It is assumed that the LSPR peak is proportional to the amount of mercury adsorbed on the nanoparticle. This assumption is based on an alloy model linearly combining the dielectric functions of mercury and gold within the Gans Solutions; more details on this are presented in Chapter 3.

2.3.2 Applying the RC model to mercury-gold nanosphere data

2.3.2.1 Data fitting technique

This resistor-capacitor model (RC model) was applied to the data collected on the impinging jet flow system. The model was applied to the three different surface coatings tested previously: bare particles cleaned in a plasma oven, 4-tert-butylthiophenol coated particles, and particles coated with a thicker polymer in a layer-by-layer (LBL) deposition. Again, it should be noted the LBL particles were larger than the other nanospheres used.

To calculate the resistance or conductance caused by convective mass transfer, the first derivative of the peak position immediately after Hg introduction was determined by fitting a line to the first 30% of the total shift. This approach proved more tractable computationally than extracting the variable from a fit to the entire data set. In essence, the initial response is diffusion limited, as the time derivative of the LSPR Peak at time zero is not a function of the pseudo-capacitance term:

$$\left.\frac{d\Gamma}{dt}\right|_{t=0} = \frac{AC_{amb}}{R_D} \qquad \text{(Equation 70)}$$

Figure 2.13 portrays graphically the curve fitting regime used to calculate the conductance due to convective mass transfer.

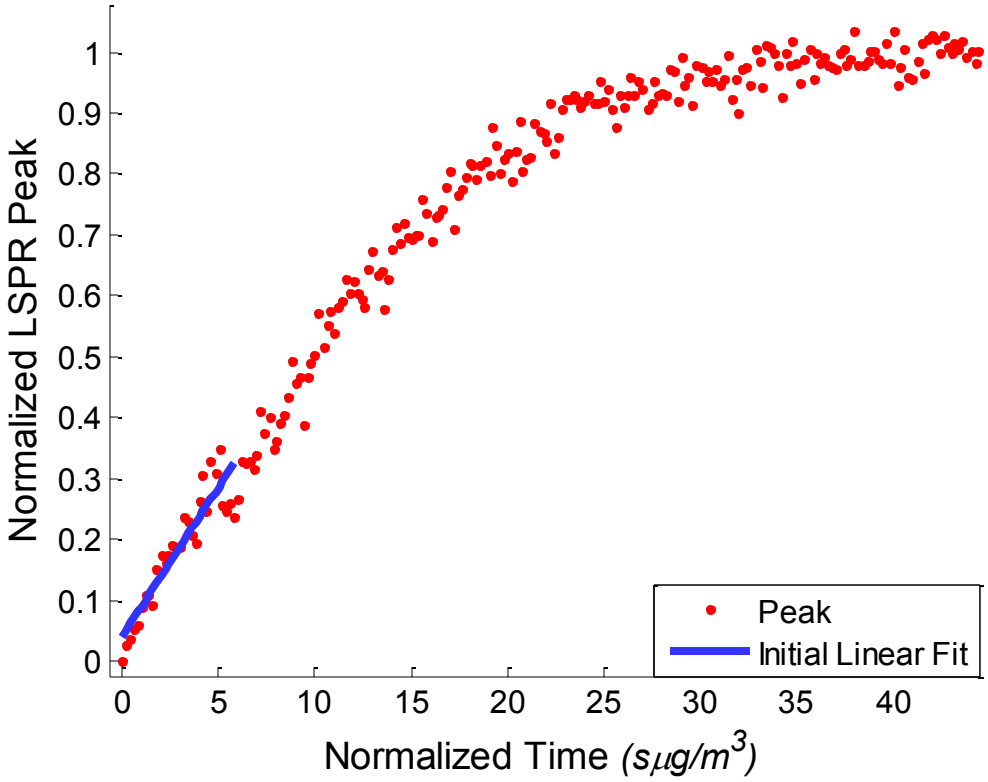

Figure 2.13. Determination of the conductance from convective mass transfer from the derivative as normalized time approaches zero. Normalized time is defined as time multiplied by the free stream concentration. Ideally at time zero there is zero LSPR shift. However, noise is the date created some uncertainty about the location of the initial LSPR peak thus the fit was not forced through the origin.

Similarly, the absorbance constant was extracted from a least squares regression fit of the normalized response fit to an exponential, portrayed in Figure 2.14.

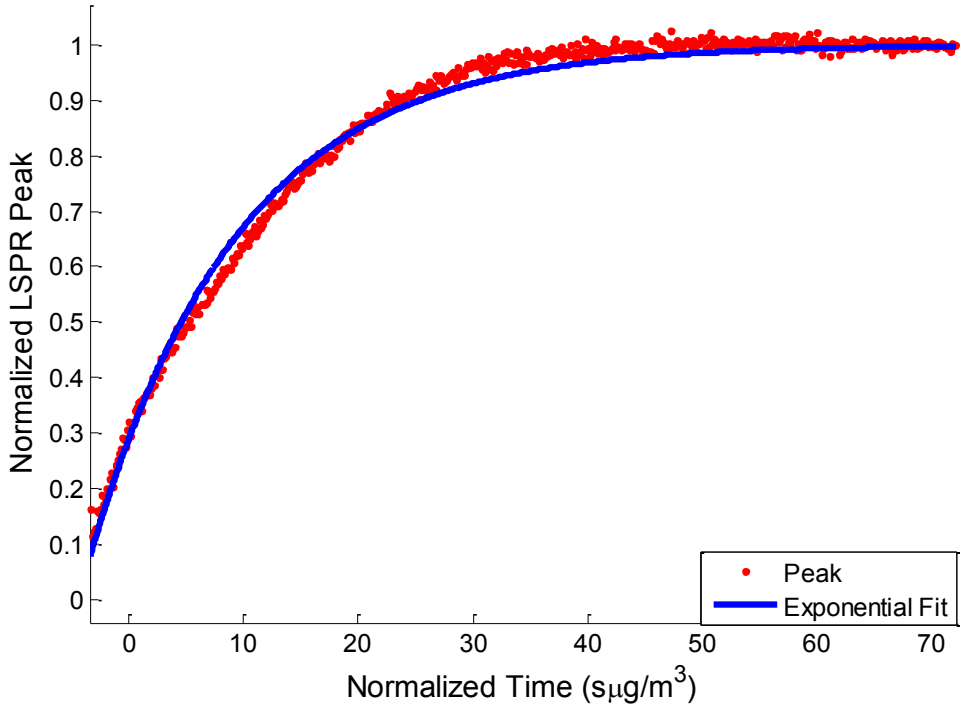

Figure 2.14. Determination of absorbance constant by fitting data to exponential curve. Similar to Figure 2.13 the fit was not forced through the origin.

2.3.3 RC model results

Running this analysis for each of the flow and concentrations conditions tested on the bare nanospheres yields a power law relationship for the conductance due to convection, with a dependence on flow rate raised to the approximately one third power, a result similar to the relationship expected from an impinging flow (Figure 2.15).

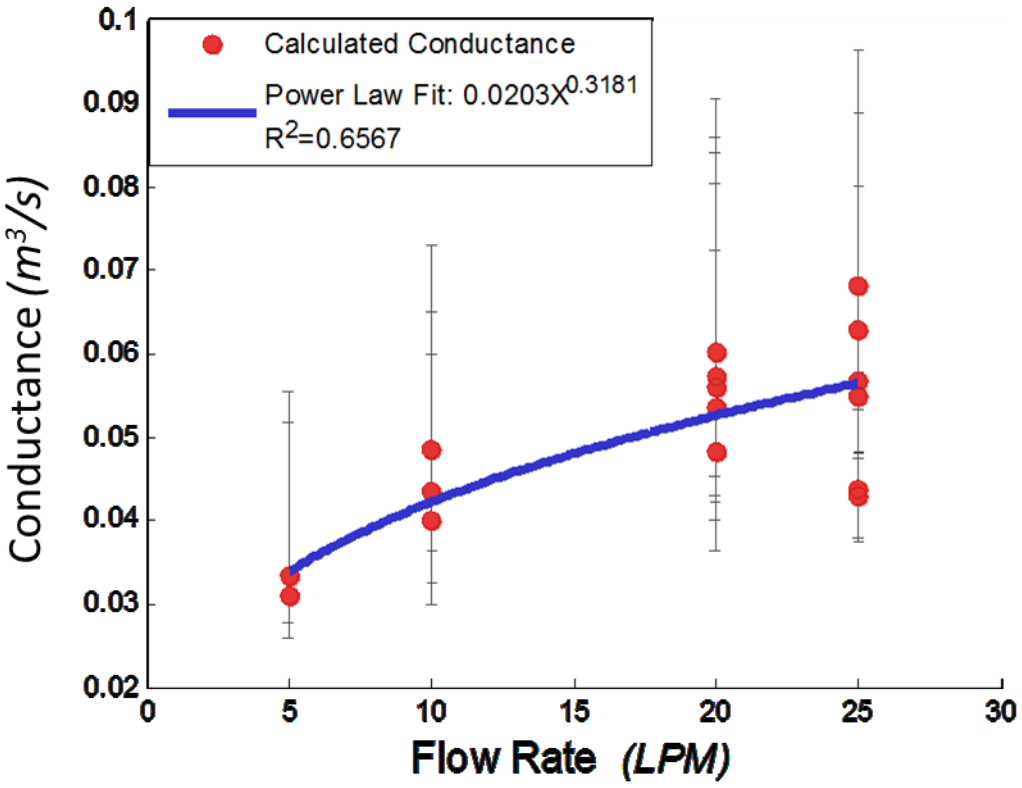

Figure 2.15. Conductance ($1/R_D$) due to flow rate for bare nanospheres. Horizontal error bars were omitted to improve clarity. The uncertainty of the flow rate was approximately 1 LPM.

As evidenced from the error bars the relationship is very sensitive to changes in concentration. While every effort was taken to maintain an accurate and constant concentration, fluctuations in temperature and flow through the CavKit were observed, and these translate to fluctuations in concentration. Thus the error bars represent the best recorded range of conductance possible from the maximum and minimum concentration observed from the CavKit on each run.

The absorbance constant is calculated based on the model using the results from the exponential fit and the conductance due to convection. While there is spread in the data, there is not an indication of dependence on flow rate or concentration. The results for the bare nanospheres are presented with the mean and standard deviation, indicated by solid and dashed lines, respectively (Figure 2.16).

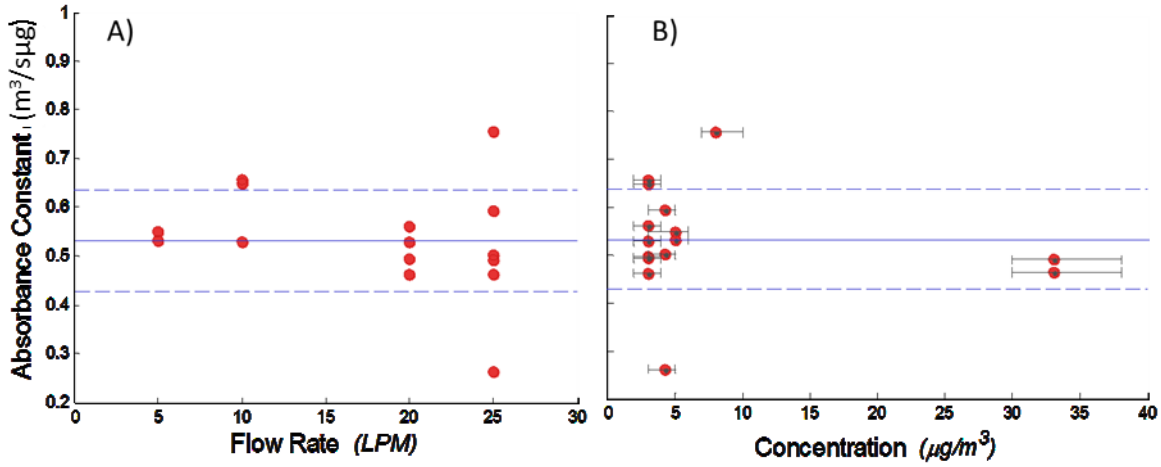

Figure 2.16. Absorbance constant (k_a) for bare nanospheres presented verses A) flow rate, and B) concentration. The solid line is the average, and the dashed lines are one standard deviation.

The equivalent data for the coated nanospheres are given in Figure 2.17 and Figure 2.18.

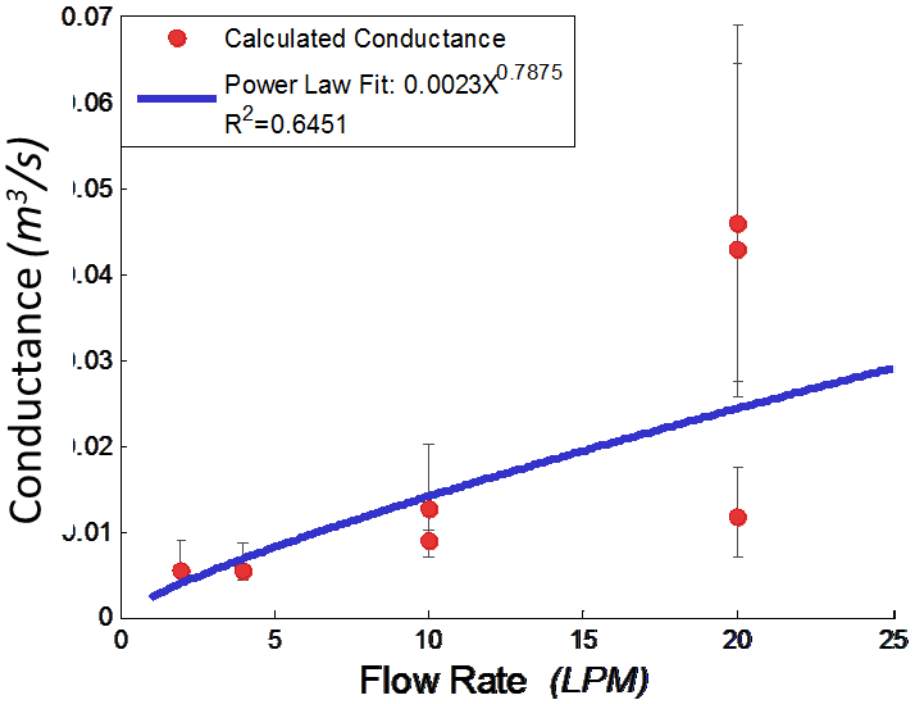

Figure 2.17. Conductance ($1/R_D$) due to flow rate. Horizontal error bars were omitted to improve clarity. The uncertainty of the flow rate was approximately 1LPM for coated nanospheres.

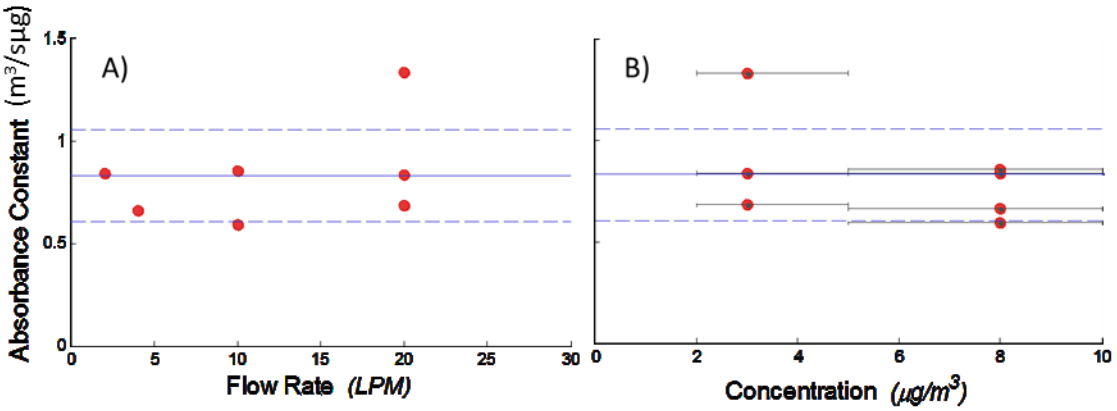

Figure 2.18. Absorbance constant (k_a) for coated nanospheres presented verses A) flow rate, and B) concentration. The solid line is the average, and the dashed lines are the standard deviation.

The data for the LBL particle substrates did not seem to follow the same trend, as seen in Figure 2.19 and Figure 2.20.

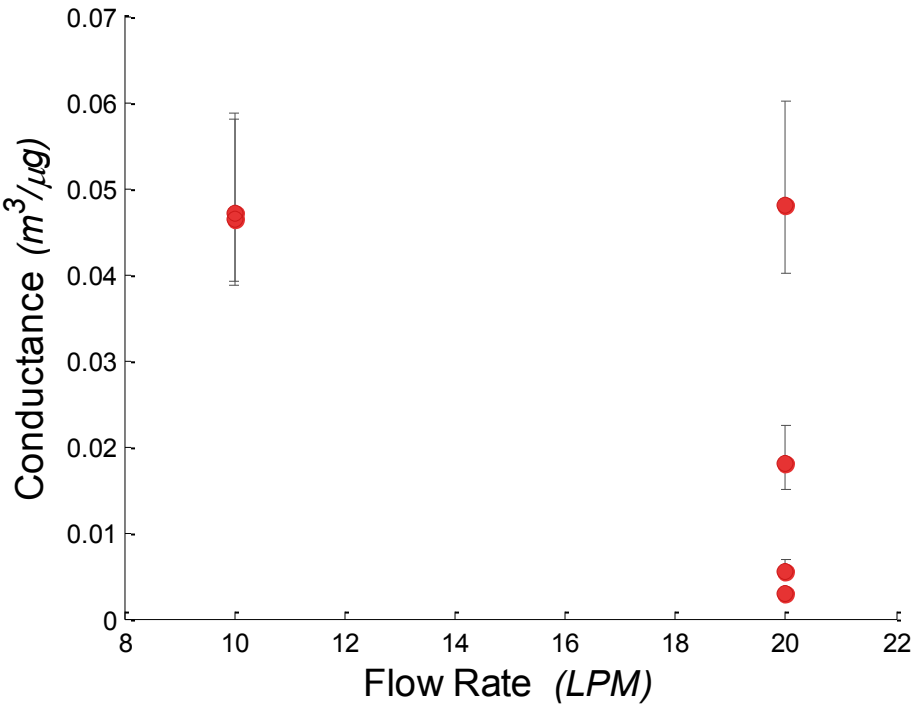

Figure 2.19 Conductance ($1/R_D$) due to mass transfer for LBL particle substrate as a function of flow rate.

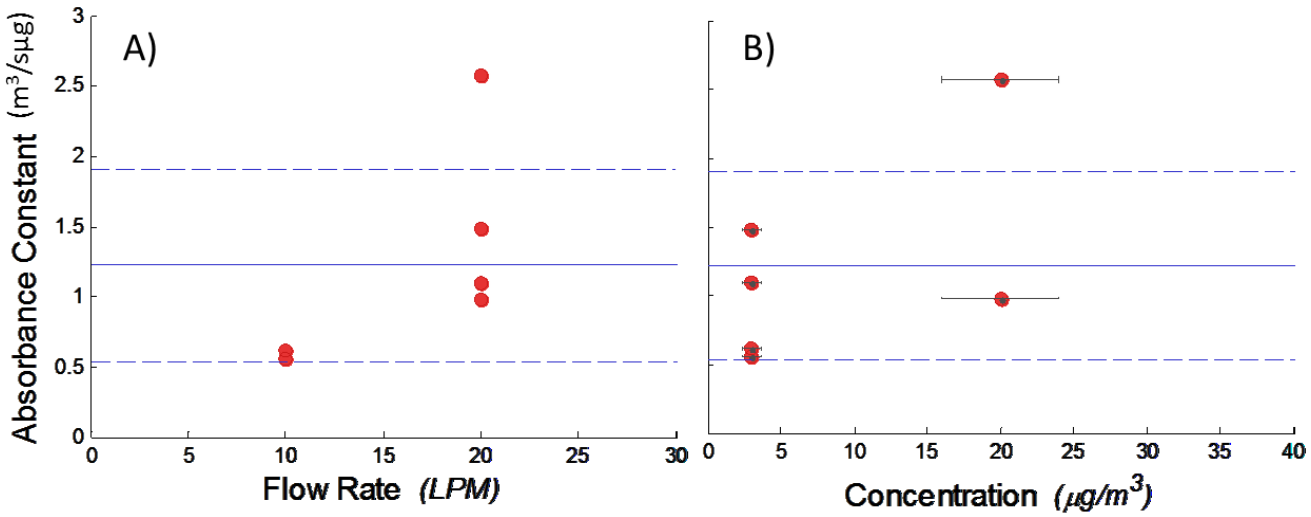

Figure 2.20. Adsorption constant (k_a) for LBL particles as a function of A) flow rate and B) concentration.

Drawing a conclusion from the limited number of LBL samples tested is difficult, especially since there seems to be a great deal of variation in the response with these specimens. They are also distinctly different in size and construction than the prior samples: 10 nm versus 3 nm particles and multiple layers versus a single layer.

The RC model does not yield an equilibrium constant, so the Gibbs Free Energy Equation could not be applied. The Classius-Calperyron relationship is also unusable, as neither different temperatures nor heats were directly measured. Table 2-5 gives the adsorption constants.

Table 2-5. Average forward first order adsorption constants for the three particle systems tested.

Particle Type	k_a (μg/sm3)	Std Dev ka (μg/sm3)
LB-Cleaned	0.533	0.104
LB-Coated	0.828	0.226
LBL	1.21	0.681

2.3.4 Conclusion

The RC model for adsorption of mercury on gold provides a framework to analyze the results, decoupling effects from mass transfer and surface kinetics. The decoupling allows the predictions from mass transfer correlations and surface kinetic models to be tested. Excepting the somewhat anomalous results of the LBL particles, there is good agreement between the

impinging flow correlation and the results obtained. The parameters used to calculate relationship between flow rate and mass transfer rate using the impinging flow correlation are given in Table 2-6.

Table 2-6 Constants for calculation of mass transfer

Variable	Value	Units
Nozzle Diameter	2	mm
Plate Size	10	mm
Nozzle Height	4	mm
Viscosity	1.80E-05	kg/ms
Air Density	1.20E+00	kg/m^3
Mercury Air Diffusion	2.00E-05	m^2/s

These values yield a mass transfer correlation of the form:

$$h_m = 0.0038\dot{V}^{0.77} \quad \text{(Equation 71)}$$

where $\dot{V}$ is the volumetric flow rate in LPM, and h_m is the mass transfer coefficient.

The predicted mass transfer correlation (Equation 71) is in good agreement with the correlations derived from the experimental results for the bare particles (Equation 72) and the coated particles (Equation 73), respectively:

$$Y = 0.0203X^{0.3181} \quad \text{(Equation 72)}$$

$$Y = 0.0023X^{0.7875} \quad \text{(Equation 73)}$$

where X and Y would be stand-ins for the volumetric flow rate and the mass transfer coefficient respectively.

It is more difficult to validate the results of the adsorption constant. The values presented in Table 2-5 are similar, if higher, than the values for chemisorption of various organic species on gold films and nanoparticles. While there is significant variation in the average, the trend seems to be higher values of adsorption constants for systems with more surface coverage perhaps indicating faster saturation due to fewer available sites.

This investigation of mercury adsorption onto gold builds upon the prior work in the field. The results clarify and confirm some prior observation concerning the adsorption of mercury onto gold nanoparticles. The adsorption follows a Langmuir type isotherm, with limited desorption at least at room temperature. The application of mass transfer correlations developed from the

field of heat transfer improves the performance of the mercury sensor[18] and suggests that such improvements could be made to other sensors. To our knowledge kinetic relationships have never been derived from LSPR measurements of mercury adsorption onto gold. Finally, the RC-circuit analogy model developed provides a framework to separate the response attributed to mass transfer and the response attributed to surface reactions. This framework was successfully applied to the data of mercury adsorption onto gold nanoparticles and could be extended to other systems.

[18] Changes in sensor geometry and flow rate were optimized towards reducing the time response of the sensor. Different choices, informed by these same mass transfer correlations, are made in Chapter 4 where the goal is improved collection efficiency for water measurements.

3. Detection of air borne elemental mercury concentration with gold nanorod decorated fiber optic sensors[19]

This section discusses the development and testing of a fiber optic based sensor using gold nanorods as the sensing medium for the detection of atmospheric elemental mercury. Mercury readily adsorbs on the nanoparticles, causing a measurable shift in the longitudinal localized surface plasmon resonance. Depositing the nanorods on the surface of a bare, bent fiber optic cable provides a means to excite the resonance and determine the absorbance through the evanescent wave at the surface. The response of the system is linear with concentration, and we have been able to directly measure concentrations down to 1.0 µg/m3.

3.1 Background

3.1.1 Fiber optic based sensing

Fiber optics are often thought of as a hallmark of the modern world, though they are based on relatively old technology and even older principles. The familiar relationship between the sines of the incidence and refraction angle of light passing through a medium change and the indices of refraction of two media is the basis of fiber optics. This law was published by Willebrød Snell in 1621[20][186]. Demonstrations of light guiding by total internal reflection were presented in the 1840's, including a clever 'light fountain' by Daniel Colladon, Figure 3.1 [187]. Waveguides found limited use in niche applications, such as luminous fountains, theatrical effects, endoscopes, and lighting for dentistry, for the next 120 years [188].

[19] Portions of this chapter appeared previously in: *Sensors and Actuators B: Chemical* vol. 181 pp. 938-942 (2013) "Fiber optic based evanescent wave sensors for the detection of elemental mercury utilizing gold nanorods," by.Jeffrey S. Crosby, Donald Lucas, and Catherine P. Koshland.

[20] Snell is usually given credit in the English speaking world for his eponymous law. In francophone countries the law is named after Rene Descartes who stated the law and gave a theoretical derivation of it in 1637. Though mostly forgotten by the 17th century, Abu Said al-Ala Ibn Sahl had presented the correct law in 984 A.D. and used it to calculate a theoretically perfectly focusing lens, or anaclastic lens. It is likely that Greek and Roman lens makers before them had at least some understanding of the relationship [186].

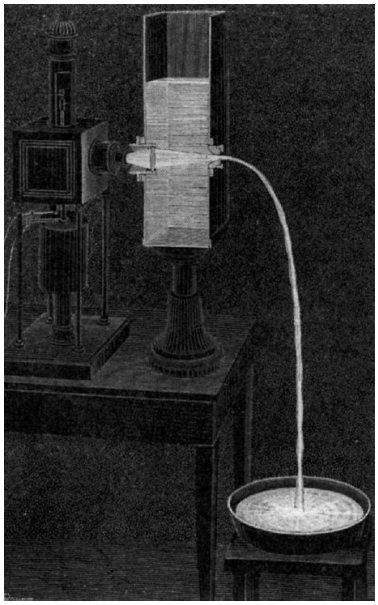

Figure 3.1 Daniel Colladon's light fountain, demonstrated in 1842. Light is directed through the water column by the light's total internal reflection at the water-air interface. Image originally published from *La Nature Magazine* 1884 reprinted in [188].

Modern fiber optics for use in communication did not develop until the late 1960's when advances in material science allowed for low loss optical fibers[21] [189]. Initial experiments utilizing fiber optics for sensing applications followed quickly. Many of the advantages that optical fibers have in communication carry over to sensors. Optical fiber sensors are compact and lightweight. They are typically minimally invasive and their flexibility allows for many geometric configurations. They are immune to electromagnetic interference. They are able to transmit high information density. They have been shown to function in harsh environments [189]. Additionally, the fibers themselves and the peripherals necessary to incorporate them into networks are now generally inexpensive and robust (at the most commonly used wavelengths) due to mass production by the telecom industry.

As with any technology, optical fiber sensors need to show a clear advantage over existing methods to be widely adopted. In areas with inexpensive, robust, and established sensors, fiber optic devices have not gained wide market share even if they perform equally well. Existing technologies have incumbency advantages [190]. Fiber optic sensors have found commercial success in underwater acoustics, gyroscopes, certain chemical and biological sensors, and temperature sensors [190]. Fiber optics can have a particular advantage in distributed sensing as they permit long path lengths [189]. Perhaps it should be noted that sensors can incorporate fiber optic cables into their design even if the signal transducing element itself is not a fiber optic element. In general this chapter discusses fiber optic sensors where the fiber optic itself plays a role in translating an analyte concentration into a measureable signal.

[21] The figure of 20 decibels per kilometer of attenuation is generally considered the threshold where fiber optic communication became viable [188]. Inexpensive semiconductor lasers are also a vital component of fiber optic communication, but they are not as critical for fiber optic sensors.

3.1.1.1 Surface plasmon resonance fiber optics sensors

Fiber optic cables have proven a versatile substrate for surface plasmon resonance (SPR) sensors. Described in Chapter 1, SPR is a collective oscillation of charge at the boundary between a metal and a dielectric. SPR's are very sensitive to changes in either the metal or the dielectric; however, they cannot be excited by free light and require a prism to couple the light into the surface plasmon. Fiber optics can replace the prism in SPR sensor configurations allowing for greater flexibility in deployment while retaining the general advantages of fiber optic sensors outlined above. Villuendas and Pelayo [191] described one of the first fiber optic based SPR sensor devices. In this case, a multilayer surface was applied to the cleaved end of the fiber. Light was reflected back to a second branch of the fiber for measurement, a configuration which is something of a hybrid between traditional prism SPR systems and later all-fiber devices. Index of refraction changes caused by parts per million changes in concentration of sucrose were detected by the sensor. Shortly after this work, De Maria et al. [192] reported on a SPR sensor based on the head of a single fiber optic cable interrogated with a He-Ne laser at 633 nm.

Jorgenson and Yee [193] improved the versatility of SPR fiber optic sensors by utilizing a white light source and placing the sensing element along a section of the fiber as opposed to at the end, Figure 3.2. The cladding of a 400 µm silica core cable was burnt away and a 0.55 nm silver layer was deposited over this declad portion. The sensor was able to detect index of refraction changes in agreement with the model presented in the work. A similar work was presented shortly after, concerning a single mode (4.5 µm core) fiber embedded in a polymer block, decladed, and coated with a silver thin film [194].

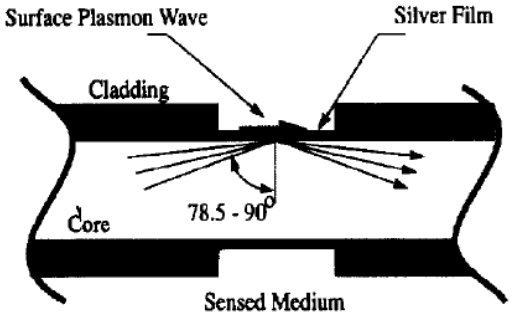

Figure 3.2. Configuration for SPR fiber optic sensor, from [193].

In the intervening two decade since these initial works, SPR fiber optics sensing has been an area of active research. SPR fiber optic sensors have been developed as chemical sensors detecting alcohols [195], salinity [196], sucrose [193], pesticides [197], and vapor phase halogenated hydrocarbons [198] among others [199]. There can be selectivity concerns with chemical SPR fiber optic sensors as any change in the refractive index will change the resonance. Occasionally this obstacle is overcome with the deposition of a coating on the metal film allowing selective permeation of the target analyte [198]. SPR fiber optic sensors have also proven particularly attractive as biosensors for their versatility and label free

detection, detecting proteins [200], bacterial toxins [201], markers of myocardial infarction [202], and other biological species [203]. Selectivity of biosensors is generally superior as the metallic thin film is functionalized with a receptor which selectively binds to the target molecule such as biotin and streptavidin [204].

3.1.1.2 Localized surface plasmon resonance fiber optic sensors

A localized surface plasmon resonance (LSPR) is an oscillation of charge which is confined by the dimensions of the nanoparticle on which it arises. Research interest in LSPR sensors has increased in recent years with increased facility in the synthesis and deposition of nanoparticles. Just as in SPR devices, fiber optic cables have proven an attractive platform for LSPR sensors. The principles and techniques of fiber LSPR sensors are broadly similar to SPR sensors; typically, changes in index of refraction, often mediated by selectively permeable coatings or target receptors, cause a change in the resonance. LSPR fiber optics have also been demonstrated to be effective chemical and biological sensors [205], [206], [207], [208], [209]. In comparing LSPR and SPR sensors, it has been suggested that LSPR sensors have a faster response time and are capable of simultaneous absorbance[22] measurements and surface enhanced Raman scattering (SERS) [20][210]. Sharma and Gupta [211], using analytical investigations, suggest that LSPR sensors typically have better signal to noise ratio and the sensitivity (response per refractive index unit change) is comparable. Both of these measures are highly dependent on the particulars of the system, such as material, particle size, and film thickness. Ultimately the sensing requirements drive the choice in transducer. As there are a wide variety of nanoparticle shapes, sizes, and materials, LSPR sensors may offer more choice in the plasmonic element. Chemical deposition of the nanoparticles onto a fiber optic surface is derived from well-established schemes [212][103][106] for glass or quartz deposition.

Nanoparticle based LSPR sensors also allow for more innovative schemes. Wang et al. [213] embedded gold nanorods in a polymer and drew the mixture into nanofibers. The polymer acted as a waveguide exciting the LSPR of the nanorod. They further demonstrated the ability of the compact device to act as a humidity sensor. Sirbuly et al. [214] combined 50 nm silver nanocubes, a single crystal tin dioxide, and a microfluidic channel into a combined absorbance, fluorescence, and SERS sensor, using an optical microscope to interrogate the device.

3.1.2 Evanescent waves

When light is totally internally reflected at the boundary between a higher and lower index of refraction material, an exponentially decaying wave arises at the interface. This phenomenon is predicted by Maxwell's equations, which do not allow a discontinuity in magnetic or electric fields at the boundary. The evanescent wave typically decays within the distance of a few wavelengths of the light and does not transmit energy. If, however, a medium which can support the propagation of the light is brought within the range of the evanescent wave, the light can be coupled into this third medium [215]. The first two media are the high index

[22] Absorbance can refer to the optical phenomena where light intensity is reduced by interaction with a material. Absorbance can also refer to the physical incorporation of a species into the matrix of another material. In this chapter the term absorbance is typically referring to the optical phenomena. The phenomenon of mercury bonding to the surface of gold, explored in chapter 2, is typically referred to in this chapter as 'adsorbance.'

material and the low index material. For fiber optics typically the high and low index media are the fiber core and its surroundings respectively. An evanescent wave is depicted in Figure 3.3.

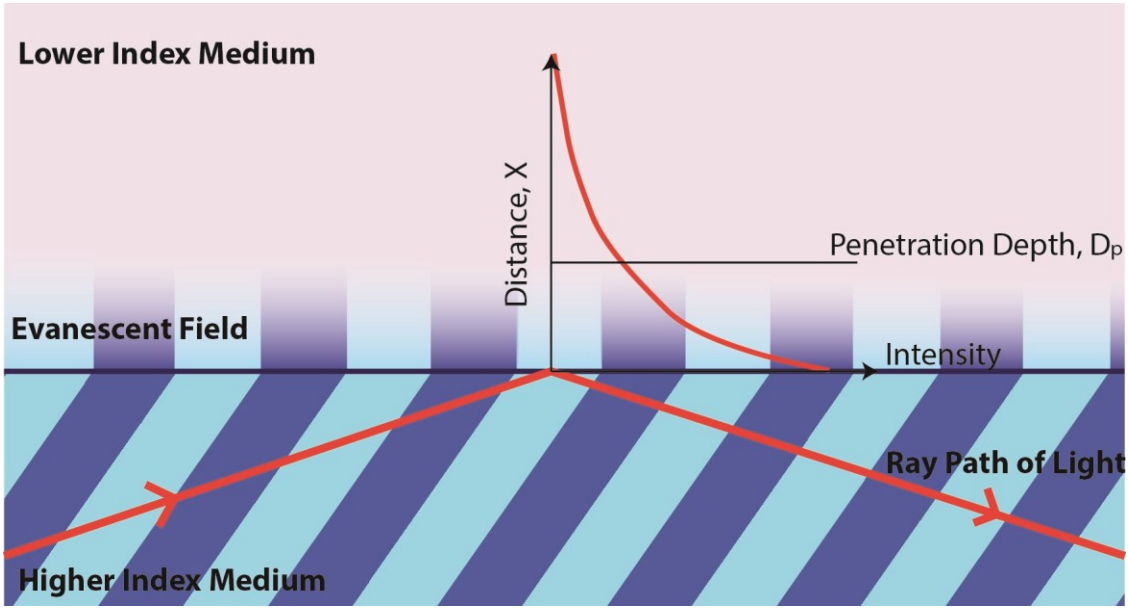

Figure 3.3. Evanescent wave on the interface of higher and lower index of refraction material. In fiber optic sensors the higher index medium is the fiber core, and the lower index material is the surrounding.

The evanescent waves which arise on the surface of fiber optic cables can be coupled into thin metallic films, or nanoparticles, which excites plasmons. This is what makes them suitable platforms for SPR and LSPR sensors[23]. The penetration depth, D_p, of the evanescent wave is given by [218][217]:

$$D_p = \frac{\lambda}{2\pi n_1 (sin^2\theta - sin^2\theta_c)^{0.5}} \qquad \text{(Equation 74)}$$

The variables used in (Equation 74) and estimated values for a typical fiber optic system are given in Table 3-1.

Table 3-1. The variables in the penetration depth relationship and estimated values for a fiber optic system.

Variable	Quantity	Estimated Value
$\boldsymbol{\lambda}$	Wavelength of light	400-700 nm
$\boldsymbol{\theta}$	Angle of incidence	80-90°
$\boldsymbol{\theta_c}$	Critical angle	$\theta_c = \arcsin(^{n_2}/_{n_1})$, 42°
$\boldsymbol{n_1}$	Index of refraction of core	1.5 (glass) [219]
$\boldsymbol{n_2}$	Index of refraction	1.0 (air)

[23] This evanescent wave can interact with target analytics directly which is a common manner of sensor operator[216][217]; this is of less relevance to this work.

For the conditions presented in Table 3-1, the penetration depth would be between 50 and 100 nm, on the same order as the length scale of many of the most commonly synthesized nanoparticles.

Several schemes have been developed to increase the interaction of the light with the surface of fiber, including tapered [220][221] and bent fibers [216][217]. Changing the path of the light allows for smaller angles of incidence between the light and the surface. Light entering a fiber optic system is typically well collimated and thus will reflect off the surface at high angles. Additionally bending the fiber converts the light to higher modes allowing for more interaction with the surface [216].

3.1.3 Application of the Mie and Gans solutions to gold nanoparticles

The Mie [89] and Gans [90] solutions to Maxwell's equation for light interacting with small particles, introduced in Chapter 1, provide a convenient and widely applied means for predicting the optical response of noble metal nanoparticle [91][87][88]. The Mie solution is given in (Equation 75); the Gans solution is given in (Equation 76); and variable names and reasonable values for gold nanospheres and rods are given in Table 3-2. Both of these solutions assume that the particle is acting as a dipole, or that the wavelength of the exciting light is large compared to the particle.

$$C_{ext} = \frac{24\pi^2 R^3 \epsilon_m^{3/2}}{\lambda} \frac{\varepsilon''}{(\varepsilon' + 2\varepsilon_m)^2 + \varepsilon''^2} \qquad \text{(Equation 75)}$$

$$\mathrm{C_{ext}} = \frac{8\pi^2 \mathrm{R}^3 \epsilon_\mathrm{m}^{1.5}}{3\lambda} \sum_{\mathrm{k=a}}^{\mathrm{c}} \frac{\frac{1}{P_k^2}\epsilon_2}{\left(\epsilon_1 + \frac{(1-\mathrm{P_k})}{\mathrm{P_k}}\epsilon_\mathrm{m}\right)^2 + \epsilon_2^2} \qquad \text{(Equation 76)}$$

where P_k are the depolarization factors of the axes (a>b=c)

$$P_a = \frac{1-L^2}{L^2}\left(\frac{1}{2L}\ln\left(\frac{1+L}{1-L}\right) - 1\right) \qquad \text{(Equation 77)}$$

$$P_b = P_c = \frac{1-P_a}{2} \qquad \text{(Equation 78)}$$

where $\mathrm{L} = \sqrt{1 - \frac{1}{\mathrm{AR\hat{}2}}}$

Table 3-2. Variables and estimated values for Mie and Gans Solutions used to calculate optical absorbance of gold nanospheres and nanorods.

Variable	Name	Estimated Value
$\boldsymbol{\lambda}$	Wavelength	400-900 nm
$\boldsymbol{R}$	Particle radius	5-40 nm
$\boldsymbol{\varepsilon_m}$	Medium dielectric function	Wavelength and medium specific
$\boldsymbol{\varepsilon'}$	Real part of particles' dielectric function	Wavelength specific
$\boldsymbol{\varepsilon''}$	Imaginary part of particles' dielectric function	Wavelength specific
AR	Particle aspect ratio	1-10

The Mie solution provides a convenient prediction of the absorbance spectra of gold nanoparticles, and the factors which influence the LSPR peak. An example is given in Figure 3.4.

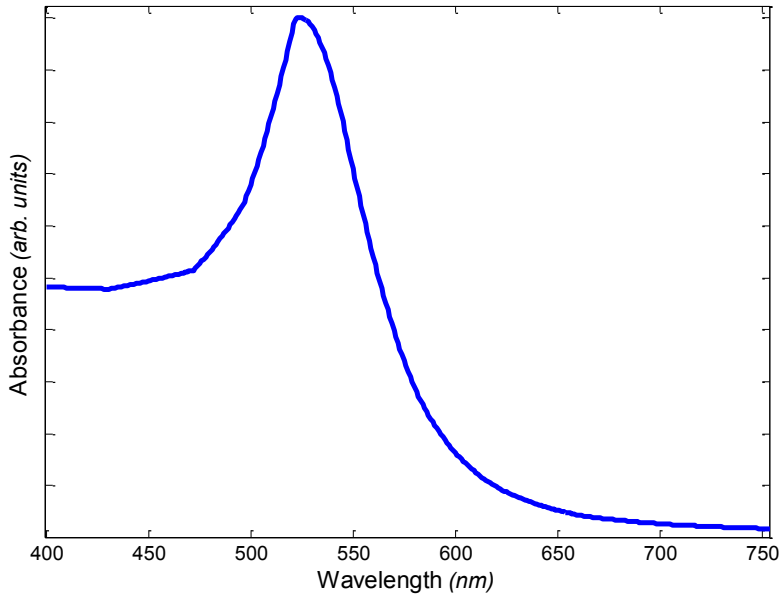

Figure 3.4. Absorbance spectrum of a 10 nm gold nanosphere as predicted by the dipole approximation of the Mie solution.

A similar example for gold nanorods, based on the Gans solution is given in Figure 3.5 and shows the strong dependence of absorbance on aspect ratio.

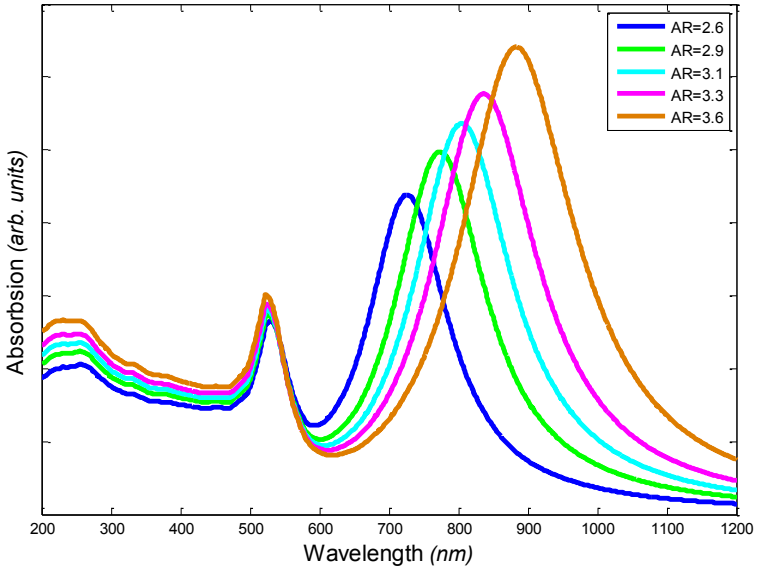

Figure 3.5. Gans dipole solution for gold nanorods. The diameter is 20 nm and the aspect ratio is as indicated. The medium index of refraction is 1.6, slightly higher than glass to emphasize the spread of the longitudinal resonance peak.

The absorbance peak at higher wavelengths is attributed to the plasmon resonance over the length of the nanorod, the longitudinal resonance peak [91]. This longitudinal resonance peak is very sensitive to changes in the aspect ratio of the particle. Nanospheres show a similar size dependent absorbance with shifts towards the red as size increases [222]. The nanospheres' size dependence is less pronounced than the shift in the longitudinal resonance of nanorods, and it is often lost in the dipole approximation of the Mie solution which neglects higher order terms that arise as the particle becomes larger compared to the wavelength of the light [223]. For the dipole approximation Mie solution the size dependence is buried within the complex dielectric function for the gold nanoparticle. In this work the dielectric function is based on established values for gold [224] with a correction for size based on the Drude free electron model [223][225][226].

The longitudinal plasmon resonance is also very sensitive to changes in the index of refraction. The relationship between index of refraction for nanorods and nanospheres as estimated from the dipole approximation Mie and Gans solution is shown in Figure 3.6.

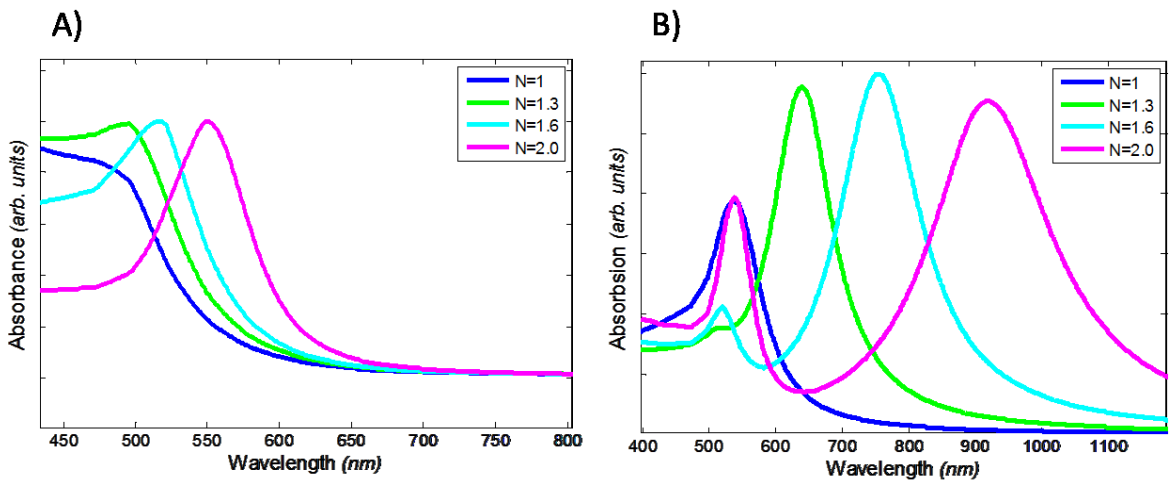

Figure 3.6. Relationship between absorbance and index of refraction for A) nanospheres, and B) nanorods, indicating the high sensitivity of the longitudinal plasmon resonance of nanorods. As the index of refraction approaches 1, the longitudinal and transverse peak of nanorods converge and the Mie solution becomes broadly absorbing at lower wavelengths.

This high sensitivity of the longitudinal plasmon peak is one of the reasons why nanorods are often chosen as a transducing medium for sensors [137][227][228][229]. A mercury sensor operates under a different principle than typical index of refraction sensors. The mercury adsorbs onto the surface, changing the dielectric function. This change is modeled using the dipole Mie and Gans approximation, Figure 3.7 .

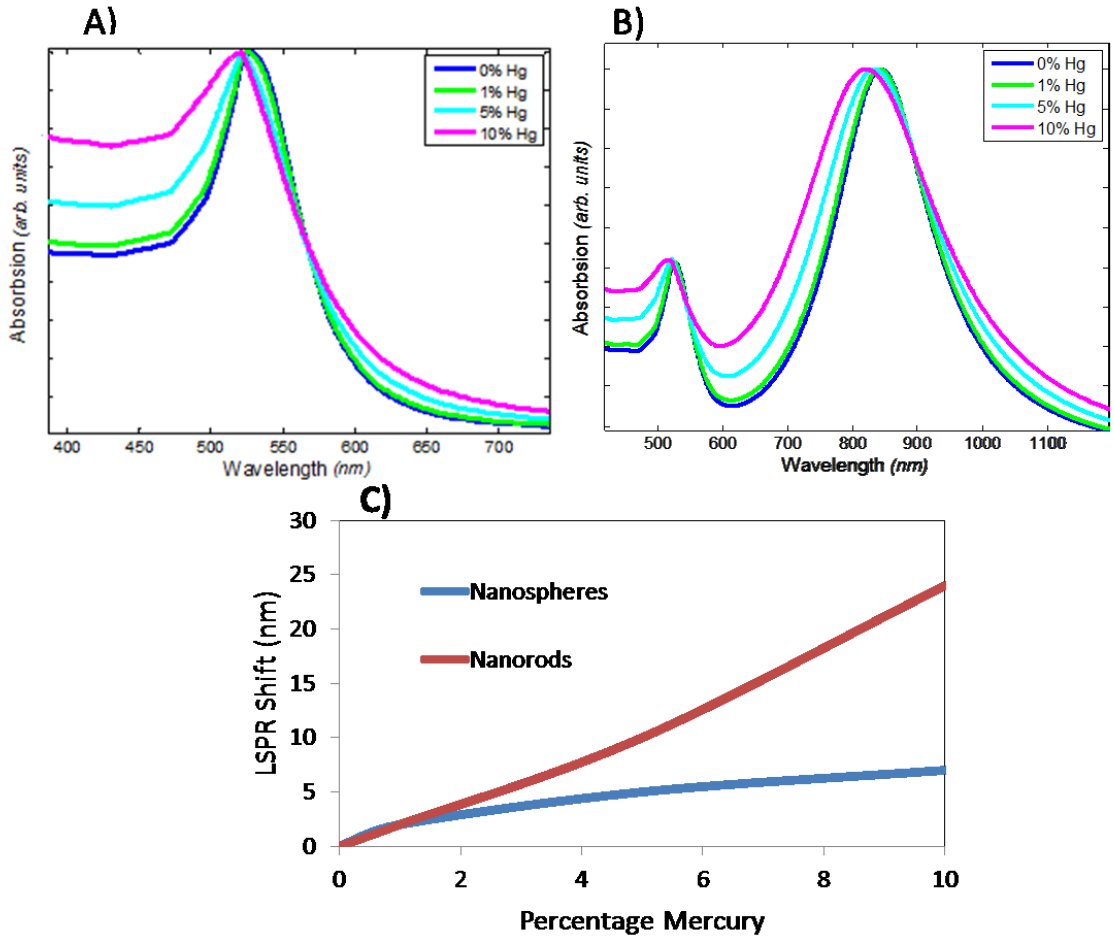

Figure 3.7. Shift in resonance peak of A) nanospheres and B) nanorods, as predicted by the dipole Mie and Gans approximation. The calculated shift is highlighted in C). The nanospheres shift roughly 2, 5, and 7 nm under 1, 5, and 10% mercury, respectively. The nanorods shift roughly 2, 10, and 24 nm under 1, 5, and 10% mercury, respectively. Mercury percentage is the proportion of the whole particle that is mercury, approximated as a linear combination of the gold wavelength dependent dielectric function and the mercury wavelength dependent dielectric constant [230].

The nanorod's longitudinal plasmon resonance is roughly twice as sensitive to mercury adsorbed. The results of increased sensitivity is based on the assumption that the amalgam particle's dielectric function is a linear combination of the mercury and the gold dielectric functions This result may not precisely predict the amalgam nanoparticles' LSPR peak as the mercury tends to form surface layers [128][127]. However, the result suggests that nanorods may be a more sensitive alternative to nanospheres, even though an equal percentage of mercury on the larger nanorods represents a greater totally sorbed[24] mass of mercury. It should be mentioned that these models are based on isolated single particles in a uniform matrix.

[24] The term 'sorbed' is used here to indicate that in the model some of the mercury may be in the matrix of the nanoparticle as opposed to just on the surface.

Actual system response and ultimate sensitivity may depend on many factors, including particle density and surface to volume ratio [138].

3.2 Experimental procedure

3.2.1 Materials and methods:

3.2.1.1 Sensor Fabrication

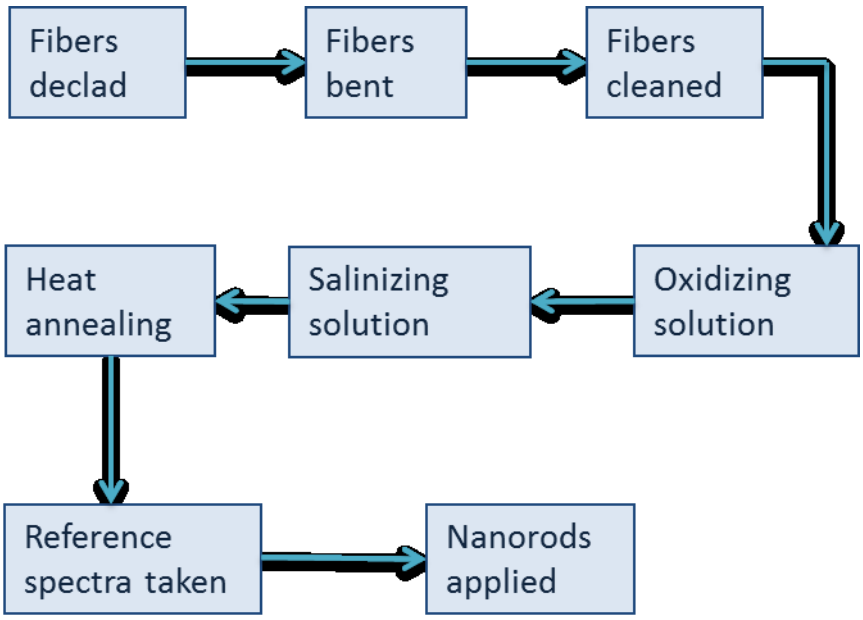

Figure 3.8. Sensor fabrication procedure; details are given in the text.

Sensor fabrication is depicted diagrammatically in Figure 3.8. Plastic clad silica fiber optic cables (600 µm inner diameter) were purchased from ThorLabs. The cables were cut to approximately 25 cm, and an approximately 5 cm section of cladding from the middle of the cables was removed by heating with a small gas-oxygen torch followed by rinsing with deionized water and careful rubbing with tissue wipes. The gas-oxygen torch was also used to heat this decladded section of the fiber in order to bend it into U-shape, with the angle of curvature approximately 90° and a radius of curvature of 7±3 mm.

Gold nanorods were attached to the bare portion of the fiber optic cable using a method derived from Frederix et al. [106]. The cables were cleaned in Citronox, a mild detergent and Millipore (18.2 MΩ) purified water. They were then further cleaned in 2M NaOH for 1 hour, and a further treatment in a 1:1:5 solution of H_2O_2 (29-32% Alfa Aesar), NH_3(aq) (28-30% EMD) and H_2O for 7 min at 80°-90°C to provide a fresh oxide layer. The cable was then rinsed again in Millipore water and dried in air before being immersed in a 95:5 methanol (99.9% Alfa Aesar): water solution with 2% (v/v) of 3-(mercaptopropyl)methyltriethoxysilane (94% Afla Aesar). The sample was left overnight, then removed and rinsed in 1 ml of methanol, before being

annealed for 10 minutes at 105°C. At this point reference spectra were obtained (before the nanorods were applied) and used later to calculate the absorbance.

All spectra were collected with an Ocean Optics HR4000 spectrometer with a resolution of 0.25 nm, controlled through their Spectra Suite software package on a PC. Absorbances were also calculated with Spectra Suite based on the log of the ratio between the reference spectrum and the current measurement.

Various surface coatings on the nanorods were tested in the experiments leading to the design of the functionalized fiber optic cable, including CTAB (cetyl trimethylammonium bromide) coated, and bare. Acrylate modified nanorods were found to be most repeatable in adhering to the bare cable. We used Nsol (akyl acrylate) polymer conjugated nanorods from Nanopartz, with nominal dimensions of 25 by 82 nm, though measurements with a TEM indicated that the particles were smaller, 19±4nm by 63±5nm. An image of the nanoparticles used is given in Figure 3.9.

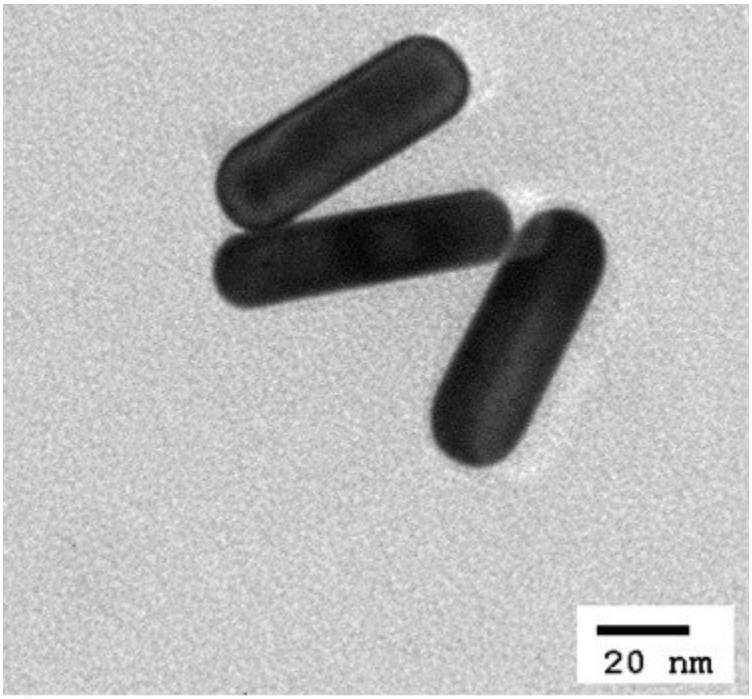

Figure 3.9. TEM image of gold nanorods used, captured on a Hitachi H-9500 operating at 120kV.

The concentrated nanorods were diluted 1:90 with ethanol, a ratio that provides a good balance between aggregation of the nanoparticles and sufficient coverage to provide a strong absorbance response. A 400 µl volume of the diluted nanorod solution was applied drop-wise from a pipette to the bare, salinized, fiber optic section, set overnight, and then rinsed with 1ml of Millipore water to remove excess particles. A schematic of the final device is given in Figure 3.10.

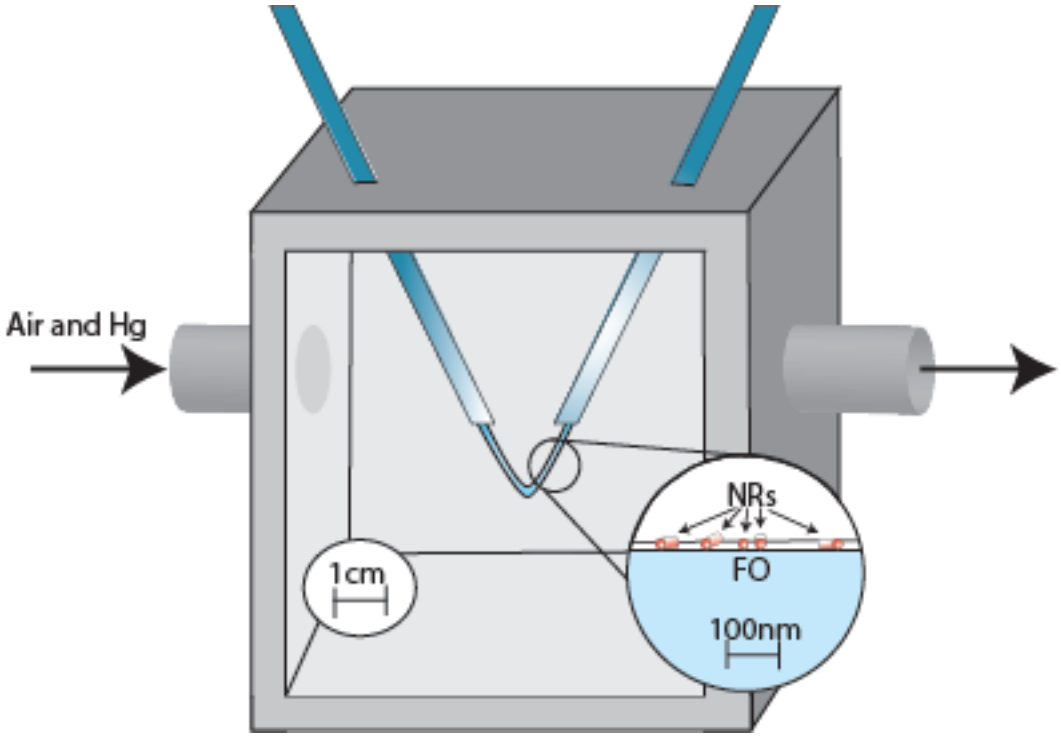

Figure 3.10. Schematic of evanescent wave fiber optic sensor with gold nanoparticles. The surrounding container is made of high density polyethylene and provides both protection to the fiber optic and a means of introducing mercury laden air.

Transferring the nanorods to the fiber optic is expected to lower the index of refraction. Changing from ethanol to a mixture of air and glass is expected to blue shift the longitudinal peak and cause changes in the full width at half maximum. The longitudinal peak is particularly sensitive to changes in the index of refraction. The change can be modeled below using a Gans Dipole approximation, Figure 3.11, and matches the shift seen in the actual nanorod decorated fibers in Figure 3.12.

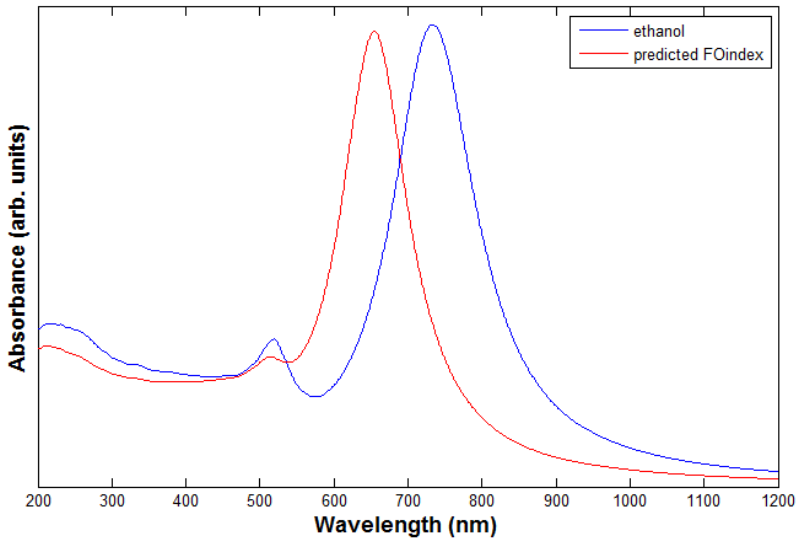

Figure 3.11. Predicted red shift of particles after attachment to fiber optic cable.

3.2.1.2 Exposure procedure

The sensor was installed into an enclosed flow system using a permeation tube (Vici Metronics) to provide a known and controlled amount of mercury vapor. This system allows a variable concentration of be delivered to the exposure chamber with a fixed flow rate of 10 LPM. The previous chapter established the importance of mass transfer effects. A constant mass flow rate creates a constant mass transfer coefficient and thus variations in the response of the sensor should be the result of concentration changes. Concentrations were checked with a Jerome Mercury Vapor Analyzer (Model 431-X) either at the exhaust from the exposure chamber or at the exhaust from the permeation tube before mixing when the concentration was within the range of the Jerome (above 1 $\mu g/m^3$).

3.2.2 Fiber optic sensor results

A comparison between the absorbance spectra of the nanorods in solution and the absorbance spectra of the nanorod decorated fiber optic cable is shown in Figure 3.12. The peak at higher wavelengths, associated with longitudinal resonances in the particle, is the main focus of this study, as it has greater sensitivity. The longitudinal peak of the nanorod film is blue shifted 50 nm from that of the nanorod solution. This blue shift can be attributed to the changes in the surrounding refractive index. There could also be some effects of coupling between the plasmons of nearby nanorods, but this effect, if present, is predicted to cause a red shift [231][232][233].

Upon exposure to mercury vapor, the longitudinal peak shows a clear and measurable blue shift, shown in Figure 3.12. A shift of 8nm was recorded after an exposure of 20 minutes to a concentration of $78\mu g/m^3$.

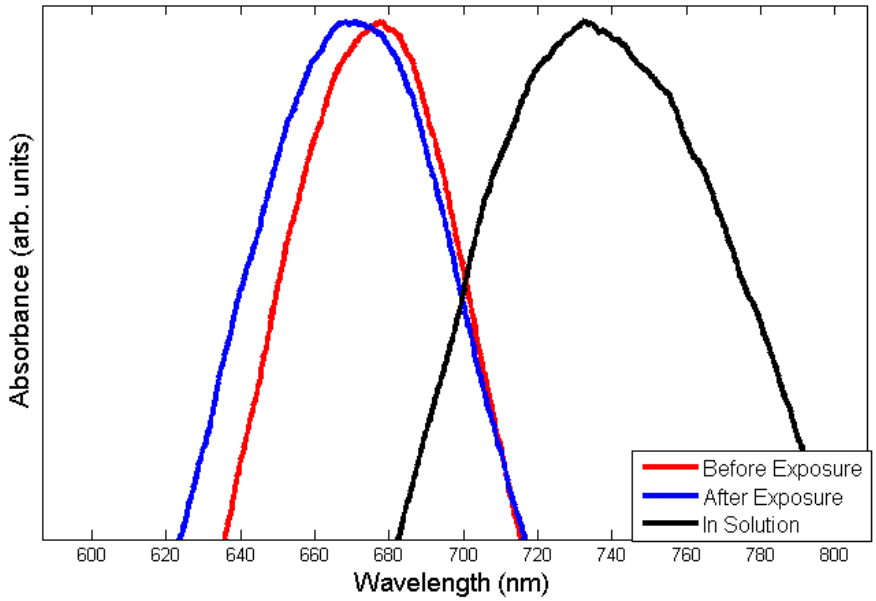

Figure 3.12. Representative blue shift of the longitudinal localized surface plasmon resonance peak from a nanorods decorated fiber optic sensor after exposure to 78 μg/m^3 for 20 min. The spectrum of the nanorods in solution is also included. The response for all sensors tested is included in the appendix.

The previous chapter established that just after exposure the sensor response should be diffusion limited. This limit is supported by the response of the nanorod fiber optic sensor which shows a nearly linear initial shift upon exposure to mercury, Figure 3.13. After that time, the rate is slower and no longer linear. This transition is attributed to the saturation of the surface and the adsorption proceeding at a rate limited by the adsorption and desorption kinetics. This observation is consistent with other investigations of mercury and gold interaction, notably the thin films investigated by Levlin et al., who showed a shift linearly proportional to the concentration, followed by a slower shift at saturation [128]. Additionally, other investigations of mercury interacting with gold nanoparticles show a saturation which is dependent on concentration [137][234][235][236].

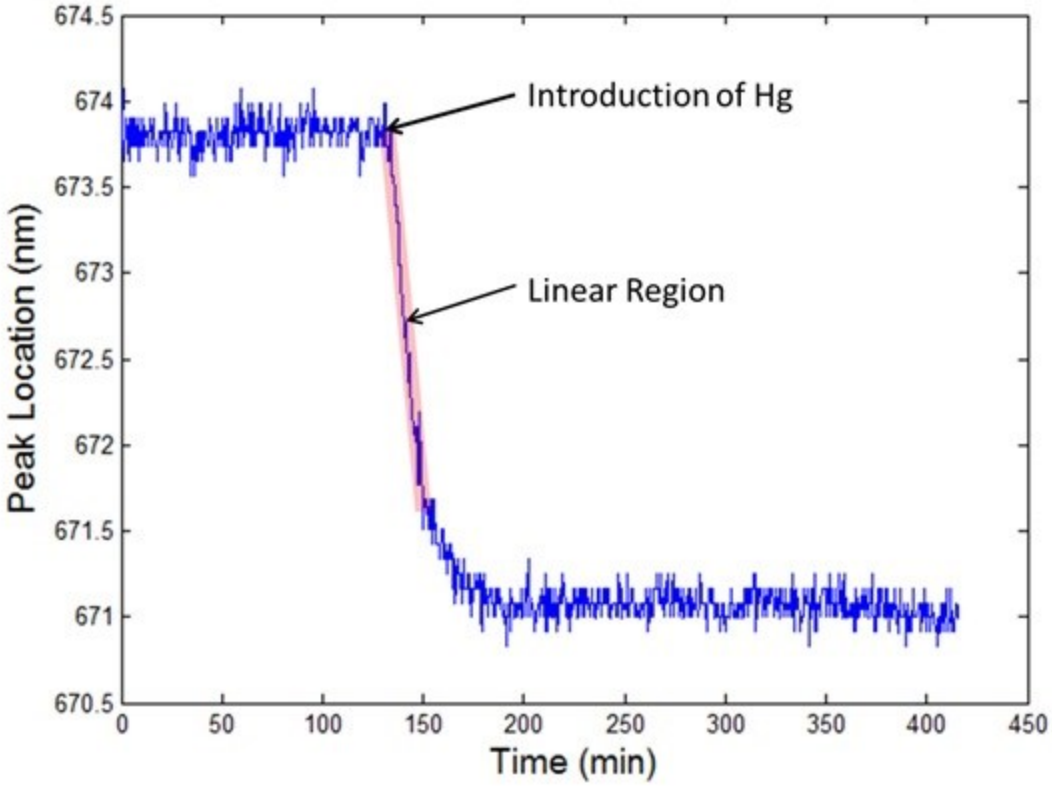

Figure 3.13. Longitudinal peak wavelength trace, indicating the point of introduction of the mercury vapor, and the linear shift, which is directly proportional to the concentration of mercury to which the sensor has been exposed.

The linear region directly following the introduction of mercury, when the transport is diffusion limited, is proposed as the measured feature most directly proportional to the concentration of mercury vapor. It is less computationally cumbersome to extract the slope of the initial linear region than to apply a more rigorous model to the entire data set. The goal of these experiments focused on the demonstration of a feasible mercury sensor, not validating the kinetics of mercury adsorption. Therefore, the initial linear shift should be sufficient to provide a working mercury sensor. This conclusion is supported by the response of several sensors to varying concentrations of mercury, shown in Figure 3.14.

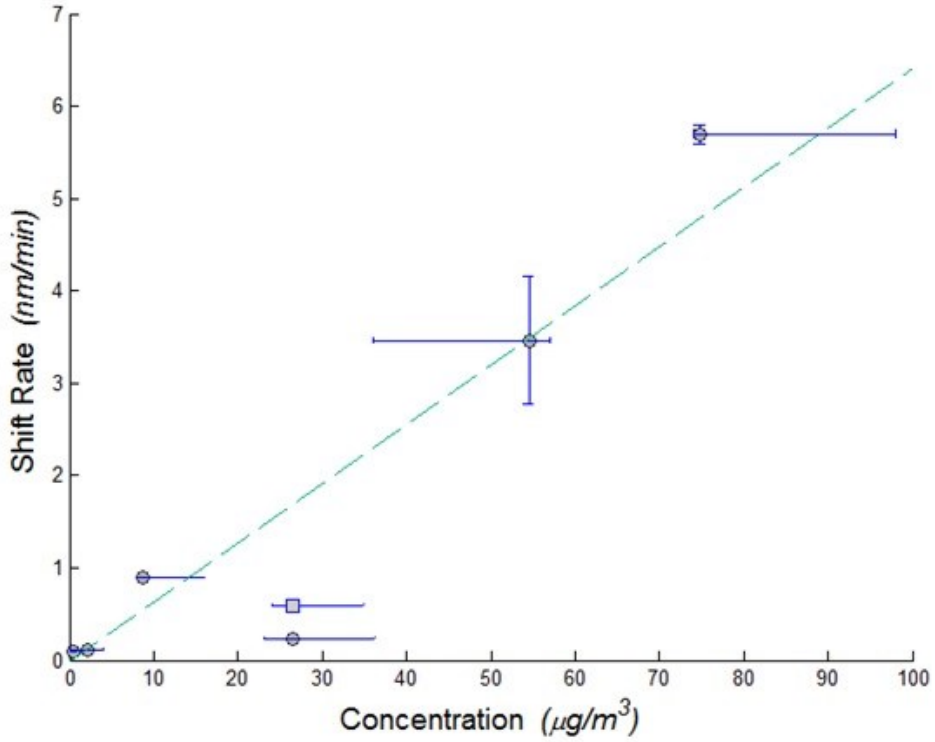

Figure 3.14. Summary results of various fibers tested at different concentrations. The dashed line indicates a linear fit to the data with a R^2 value of 0.845. The square data point at 25μg/m^2 concentration represents a regenerated run as described in the text.

Each data point represents a separate sensor which was manufactured and then individually tested, with the exception of the single square point, which is a measurement run after the regeneration of a sensor. This sensor has previous been used for the highest concentration data point at 75 μg/m^3. The regeneration was performed by running clean air over the sensor which had been heated to 70°C in the water bath for several hours; after this regeneration the sensor was exposed to 25 μg/m^3. The concentration values were determined from the predicted output of the permeation tube and measured air flow rates. The error bars in concentration were given by direct measurements with the Jerome analyzer at the outflow of the exposure chamber if the concentration was within the range of that instrument. If the concentration was below the range of the Jerome, the measurement was taken at the outflow of the line from the permeation tube to exhaust and then multiplied by the appropriate dilution ratio. Uncertainties in the flow rates were small compared to those from the Jerome analyzer.

Uncertainties in shift rate were calculated based on the standard deviation of the initial peak, giving a high and low value for this peak. A range for the final, or saturation peak, was also calculated based on one standard deviation of the peak location. The initial and final peak range was combined with the time resolution of the spectrometer to give maximum and minimum values for the shift rate:

$$\dot{Y}_{max} = \frac{(Y_{initial} + SD) - (Y_{sat} - SD)}{(T_{initial} + T_{step}) - (T_{sat} - T_{step})} \quad \text{(Equation 79)}$$

$$\dot{Y}_{min} = \frac{(Y_{initial} - SD) - (Y_{sat} + SD)}{(T_{initial} - T_{step}) - (T_{sat} + T_{step})} \quad \text{(Equation 80)}$$

where Y indicates the position of the peak at the indicated times, SD is the standard deviation, $T_{initial}$ is the time at mercury exposure, and T_{sat} is the time at mercury saturation, with T_{step} being the time resolution of the spectrometer. In most cases this uncertainty was small, smaller than the size of most of the data point markers in Figure 3.14. The exception is the point at 54.5 µg/m^3 which has an uncertainty range of approximately 20%; this is attributed to higher noise in the data causing a larger standard deviation compared to the total shift.

3.3 Discussion: temperature effects and selectivity of fiber optic sensors

As the flow conditions were constant, from Fick's law the mass transfer to the nanorods should be linearly proportional to the concentration. The shift rate does appear to follow a linear relationship with concentration. The observed deviations from linear are attributed to variations in the construction of the sensors, as the peak LSPR locations do vary from one sensor to the next. Variations in the deposition of the nanorods onto the fiber optic, particularly effects of coupling between nanorods, can cause significant variations in the response of the sensors [237]. However, all of the initial peaks, before exposure, were within 10 nm of 645 nm for the six sensors used in this study. Nanorod coupling, percent surface coverage on the fiber, and other variables of sensor construction create a slightly different proportionality constant between the mercury concentration and the LSPR response, contributing to the deviations seen. While this would be detrimental to a sensor in the field, a linear relationship between mercury concentration and initial shift rate was observed for all sensors. The regeneration and reuse of sensors could provide a means to remove this variability. A regenerated sensor would retain the same characteristic deposition of nanorods and thus could be calibrated and used repeatedly for more accurate concentration measurements. Another important contributor to uncertainty is the variations in measurements using the Jerome analyzer, especially at low concentrations near the limit of detection.

LSPR peak shifts caused by temperature changes could be expected in a system that measures ambient concentrations as a temperature shift would change the index of refraction around the particles. Even with temperature control in our apparatus, shifts of up to 1K were measured inside the flow chamber. To determine if this is a factor we used a model based on the Gans dipole approximation. The gold dielectric function was calculated as before, and the medium index of refraction is a simple approximation based on a linear combination of accepted models for air and glass (Ciddor [238] and Sellmeier [226][239]).

The results of the model for a variety of temperatures are given in Figure 3.15, which indicate that a variation of 1 K would create a shift of around 0.2 nm, much smaller than the shifts observed.

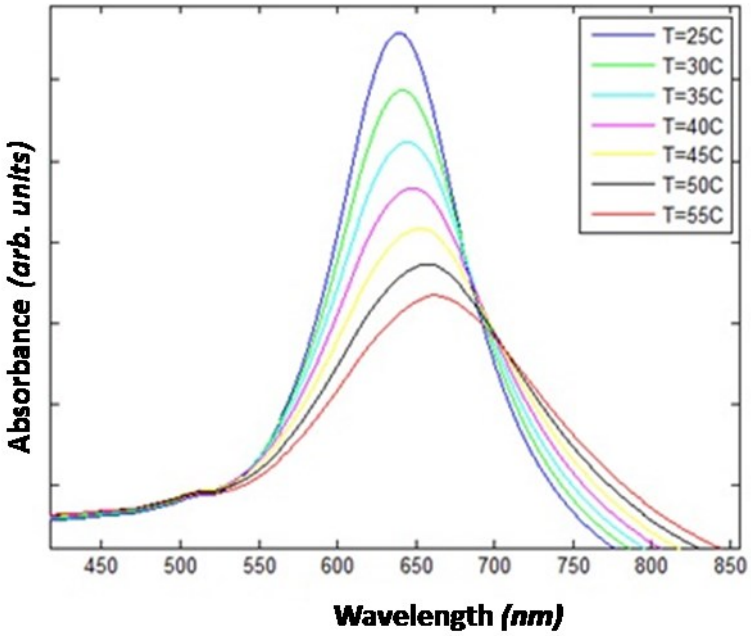

Figure 3.15. Effect of temperature variation on the absorbance of nanorods as modeled by a Gans dipole approximation.

Additional effects on the refractive index of the nanorods could be caused by changes in humidity or the deposition of additional compounds onto the fibers.

The selectivity of the sensor is an important concern. Other common atmospheric species are expected to change the index of refraction less than variation in temperature and relative humidity. These can be measured, corrected, and controlled. The exceptions are species which could physically coat the sensor, such as particulate matter, and species which could bond to the gold, such as certain sulfur compounds. Further testing, perhaps with coal flue gas, is necessary to ascertain what effect, if any, these compounds may have. Possible routes to accounting for the influence of non-mercury species include selective coatings, a reference sensor line, flue gas dilution, and post processing with temperature and humidity data.

3.4 Concluding remarks on fiber optic sensors

We have demonstrated a highly sensitive mercury vapor sensor that is straightforward to operate and relatively easy and inexpensive to fabricate. The method of deposition of nanorods on fiber optics is effective and adaptable to other similar systems. The sensor response is linear with mercury concentration, and it directly detected mercury down to 1 $\mu g/m^3$. The fiber optic cable provides a convenient and versatile platform for introducing the mercury gas stream to the gold nanoparticles. Nanoparticle decorated fiber optic cables can be distributed and fit to

near any geometry for the detection of mercury in locations that are difficult or hazardous for typical measurements. However, the more complex flow conditions over the fiber optic make analysis and optimization of the mass transfer difficult. Gold nanorods are sensitive to mercury and have been shown in this work to be regenerable with heat. They are typically larger than nanospheres, thus their higher sensitivity maybe counteracted by lower surface density and surface area to volume ratios. This novel sensing arrangement could provide useful mercury detection in areas that are underserved by current technology.

4. Detection of mercury in aqueous samples with gold nanoparticles

This chapter discusses the application of gold nanoparticle sensors to measure mercury in an aqueous environment. Utilizing the same gold nanoparticle technology as used previously in Chapters 2 and 3, mercury was detected below the EPA standard for drinking water. The modification of an established oxidation/reduction scheme for use with the sensor allows for the detection of ionic and organic mercury which would not be reactive with gold nanoparticles. This chapter ends with a discussion of some preliminary field tests and possible routes to improve sensor performance and extend the method to solid samples.

4.1 Introduction

4.1.1 Motivation

The measurement of mercury in water is an area of current concern and active research [240]. Currently the majority of anthropogenic mercury emissions are terrestrial; anti-dumping laws and water standards have reduced the direct release of mercury species to watercourses [241]. However, this does not diminish the importance of monitoring and studying mercury in aquatic environments. Legacy contamination will continue to impact mercury fluxes. Indeed, in some ecosystems, such as the San Francisco Bay, current mercury reserves dominate the transport. Despite decades of controls, concentrations have remained roughly constant over the last 40 years in the San Francisco Bay [242]. Additionally, the global nature of the mercury cycle means that atmospheric emissions a continent away can impact even remote environments. The consensus is that the bulk of mercury in the ocean is due to atmospheric deposition [243]. Essentially all of the anthropogenic mercury in the Arctic is from lower latitudes, though remoteness, measurement difficulty, and modeling complexity make the exact extend is difficult to establish; a situation that highlights the need for better detectors [244].

The majority of most human populations' exposure to mercury comes from the consumption of aquatic protein, and the United States population is no exception. Dietary preferences and contamination level means the mercury burden is dominated by the consumption of tuna [245]. Similarly, exposure in Spanish populations was dominated by tuna consumption [246]. However, mercury consumption in maritime Arctic regions such as Greenland or the Faroe islands tends to be dominated by exposure to marine mammals such as harp seals or pilot wales [247][18]. These examples highlight some of the variability in exposure regimes but also the importance aqueous environments play in the global mercury transport cycle impacting humans and other species. The majority of the exposure to infants and fetuses, whose exposure is under the most scrutiny because of suspected cognitive deficits, is probably through this marine vector as well.

4.1.2 Challenges of mercury measurement in aquatic environments

The importance of aqueous environments in the transport and fate of mercury provides the impetus to study this problem, while the variety and complexity of aqueous environments

creates challenges in its. While not diminishing the challenges of atmospheric measurements, there are simply many more variables which can affect mercury in aquatic environments: salinity, biological action, turbidity, currents, fluvial fluxes, as well as the variables common to both media: temperature, photochemical reactions, and fluxes to sediment. Global and regional transport models have made great strides in predicting the deposition and concentration of mercury [42][248]. Even with improved modeling and computational power, measurements are still necessary to validate models and provide boundary conditions. The great variety and size of the systems means that some are comparatively well researched while others are not. In addition, unaccounted point sources or legacy containments could increase concentrations beyond the range predicted by a model for a small body, which could adversely impact a local community.

One of the issues surrounding mercury detection in water is that of speciation. Mercury exists primarily in two forms in water: ionic mercury and methylmercury[25]. Mercury can also be found as dissolved gaseous mercury and bound in particles. The issue of speciation goes beyond simply complicating the direct determination of mercury in water, as the species are affected by different transport and fate factors in the environment. For example, carbon and chlorine levels in the water impact the conversion of ionic mercury to methylmercury, and methylmercury is typically of the most concern to fish consumers [243]. Determining the mercury species in various bodies of water could lead to a more robust understanding of the global and local mercury cycles. Beyond academic interest, better measurements and information could improve the choices that people make regarding the consumption of fish; fish concentration levels can vary not only with fish species but also with location [241][245]. Consumers are often presented with competing information concerning fish consumption[249].

Increased research concerning mercury in water is needed. A recent conference on the status of mercury in marine environments, Coast Marine Mercury Ecosystems Research Collaborate (September, 2010 and July, 2011), suggested areas where additional research could be beneficial [250]. Mason et al. [243] indicated regions that have been poorly sampled: Southern, Indian, and the South Pacific oceans, especially along the full depth of the water column. These measurements combined with real time, or near real time, sampling could influence policy decisions, indicate which control measures are impacting concentrations, and where future regulations would be most impactful. Lambert et al. suggested that better integration of water and air measurements, in addition to cross group communication, could yield information of use to policy makers[241]. There have been calls for a coordinated global monitoring system to tie together and validate disparate measurements of national and sub-national groups [251]. The calls culminated in the establishment of the Global Mercury Observation System, GMOS, [252]. Funded primarily by the European Commission, the project will collect data from over 40 ground stations run by the GMOS group and partner organizations along with ship and air craft

[25] Methylmercury most correctly refers to mono-methylmercury ,CH_3Hg; dimethylmercury, $(CH_3)_2Hg$ is also present in the ocean at detectable levels and is a potent toxin. Most analytical techniques cannot distinguish between the two forms [243]. As relative concentrations between mono- and dimethylmercury is not a primary focus of this work, the term 'methylmercury' will be used to refer to the sum of both species with the assumption that the majority portion is made up of mono-methylmercury. If further clarity is necessary, the prefixes will be attached.

based measurements. The aim is to validate global models and help inform policy. Simpler to operate, cheaper, and more robust measurement devices would aid in reaching goals and by extension influence policy towards mercury reduction.

4.1.3 Current measurement techniques

The measurement of mercury in water is complicated primarily by the issues mentioned above; speciation must be accounted for and other compounds in the water (or the water itself) must be handled in a manner so as to not interfere with the measurement. Speciation is a concern in air measurements, though usually to less of an extent, as over 95% of the mercury in air is elemental [251]. Contamination is an issue is both air and water measurements depending on the quality of the sample. Additionally there are water and gas handling issues particular to water measurements. Most transducer elements in mercury sensors do not function in water. The thin film resistance measurements, which are the bases for industrial measurements, are confounded by liquid water, and even water vapor condensing on them can cause significant errors [74][253]. The state of the art environmental systems based around Cold Vapor Atomic Fluorescence Spectroscopy, CVAFS, require a dry inert gas to operate. Usually argon or nitrogen are used so as to not quench the florescence signal from the mercury [69].

Water samples analyzed with CVAFS must be pre-treated. The most common method has been standardized in EPA Method 1631 (revision E) [73]. Samples are prepared by being collected in trace metal free bottles, as avoiding contamination from trace mercury during collection or analysis is an issue of grave concern. Meticulous care[26] is taken to prevent reporting contaminated results. The sample is preserved by adding either a strong acid or strong oxidizing agent. Just prior to analysis all forms of mercury in the sample are oxidized to ionic mercury. The ionic mercury is then reduced to elemental mercury. This elemental mercury is not stable in solution and is easily separated usually by bubbling a gas stream through the sample. The mercury impregnated gas stream is then fed into a CVAFS system for analysis. Briefly, the CVAFS adsorbs the mercury onto a gold trap and then heats the gold trap to release the mercury into an inert gas carrier stream. The inert gas passes through the atomic fluorescence spectrometer where the mercury absorbs and then readmits ultraviolet light. The intensity of the emission is proportional to the mercury concentration. A series of gold traps before the inlet of the CVAFS is sometimes used to reduce contamination and aid in collection[73].

There are variations on this method, such as EPA Method 245.7 [254] or EPA Method 1630, and additions which extend the method to solid and semi-solid samples [255]. While the exact reagents used and the range of desired sensitivities might be different in these other methods, the basic analysis steps remain the same; chemical pretreatment is utilized to adapt a water sample for analysis with a gas phase mercury sensor.

There are alternatives to chemical pretreatment, though they have not found widespread use nor have they been incorporated into official standards. Vil'pan et al. [256] used a two-step

[26] The EPA Method 1631 calls out several steps for reducing contamination and interference including sample processing in a class 100 clean room, metal free apparatus, acid washing of glassware, and proper sample collection techniques [73, p. 16]

vaporization/adsorption scheme to separate mercury from liquid samples. The system involved the heating of a sample until vaporization, the preferential adsorbance of mercury on a cooled trap, and finally the subsequent re-vaporization for analysis via atomic absorbance [257]. This technique avoids the use of reagent chemicals but requires careful tuning of the trap temperatures to avoid losing some mercury. Because of mercury loss, or other methodological restrictions, their system did not achieve the limit of detection possible with the more conventional chemical pretreatment [256]. Andersson et al. [258][258] designed a novel system based on liquid gas counter-flow and the equilibrium between the two phases for the detection of mercury. The system allows for continuous measurements of dissolved gaseous mercury at an air-water interface and has found some success measuring this component of mercury near the sea surface [259][243]. While providing valuable information about this important mechanism, the system is limited to elemental mercury and it also requires a CVAFS as the analytical heart of the device.

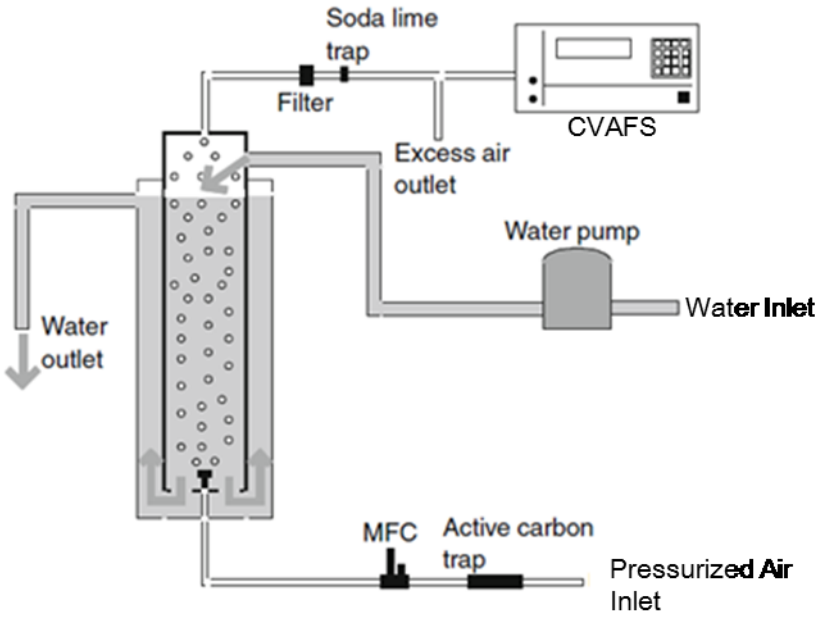

Figure 4.1. Example of continuous flow mercury analyzer for detection of dissolved gaseous elemental mercury. MFC is a mass flow controller, and CVAFS is a cold vapor atomic fluorescence spectrometer, in this case a Tekran 2537a. Adapted From [258].

4.2 Aqueous mercury detection utilizing gold nanoparticles

4.2.1 Experimental design

An impinging flow geometry, similar to the one described in Chapter 2, was used as the platform for this series of tests. This apparatus was chosen for a variety of reasons. The mass transfer of mercury to the surface is efficient and well characterized, and the open and modular nature of this platform gives a great deal of control over this mass transfer. This apparatus

allows for well controlled heating and regeneration of the sensor which shortens the time between tests; it also allows for relatively easy replacement of substrates themselves, if they are damaged during water testing. Finally, our experience with this sensor allowed for easier adaptation to water measurements. While this sensor platform proved successful for these initial water experiments, the techniques employed here could be applied to other sensor configurations , such as nanoparticles deposited on a fiber optic.

The nanoparticle sensor was fabricated in a similar manner to the description in Chapter 2. Briefly, 4-tert-butylthiophenol functionalized gold nanospheres suspended in toluene were purchased from Sigma-Aldrich. The deposition onto the quartz substrate was accomplished by Langmuir-Blodgettry, a procedure which allows control over the density of deposition by controlling the surface pressure of a film of nanoparticles suspended in chloroform, a non-polar solvent. The chloroform/nanoparticle layer floats on a trough of water and the surface pressure is controlled by a mechanical arm. The monolayer coverage was verified by examination of a silicon nitride grid by TEM which was dipped simultaneously with the substrates used as mercury sensors. The finished chips were cleaned by exposure to oxygen plasma for 10 minutes. This removed the organic surface coating, improving the sensitivity of the sensor. The set-up is depicted in Figure 4.2.

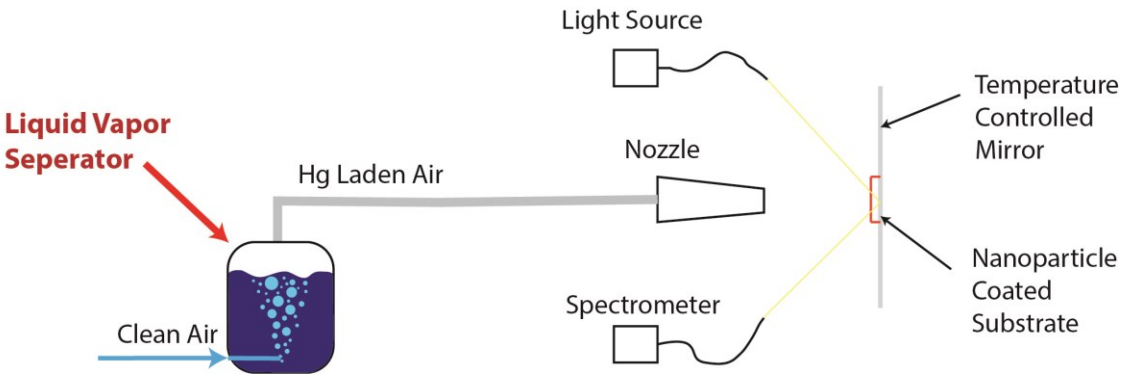

Figure 4.2. Diagram of experimental apparatus, not to scale.

The light source was a DH-BAL 2000 (Ocean Optics) equipped with both halogen and deuterium bulbs. This was coupled to 600 µm fiber optic cables terminating in a collimating lens to focus the light on the slide. The reflected light was coupled back into a second 600µm fiber optic cable via a second collimating lens. This fiber optic cable terminated at an Ocean Optics QR9000 spectrometer with a resolution of 0.8 nm over the 200 nm to 1000 nm range. The spectrometer was controlled and data collected using the Ocean Optics software package Spectra Suite.

A lab-built dehumidifier and filter cleaned and dried the house air. The air was passed through a liquid vapor separator, highlighted in Figure 4.2; this is a key step in the detection of mercury from aqueous media. In the course of the investigation two different configurations were tested: a Pyrex glass bubbler and a lab built disposable separator. These are described shortly. A mechanical separator is, however, not sufficient to separate ionic mercury as the mercury

preferentially partitions in water[27]. The same is true to a lesser extent for methylmercury. A chemical process is necessary to convert these species into elemental mercury which can be separated by bubbling. The chemical process used is described as follow:

1) Any residual mercury is oxidized to Hg^{2+} with bromine monochloride, a potent oxidizing agent

$$Hg(0)_{(aq)}+BrCl_{(aq)}\rightarrow Hg^{2+}{}_{(aq)}+Br_{(aq)}+Cl_{(aq)}$$

2) Hydroylamine hydrochloride is added to the mixture to remove any residual bromine monochloride, which can dissociate producing free halogens and damaging the gold nanoparticles.

$$NH_2OH\bullet HCl+3BrCl+2H_2O\rightarrow HNO_3+3HBr+4HCl$$

3) Ionic mercury, Hg^{2+}, is reduced with stannous chloride.

$$Hg^{2+}{}_{(aq)}+SnCl_{2(aq)}\rightarrow Hg(0)_{(aq)}+Cl_{2(aq)}+Sn^{4+}{}_{(aq)}$$

Addition of these chemicals in sequence and in sufficient quantities to convert all the mercury to the elemental species allows the mercury to be in the elemental form which is then transported to the gold nanoparticles and detected. The details of this sequence are presented in the next section.

[27] The exact solubility of ionic mercury in water depends on temperature, ionic strength, and the presence of other salt species. Mercury (II) chloride, a common mercury salt and the one tested here, the solubility at 298.15 K is 0.269 ± 0.003 mol/kg. For comparison, elemental mercury has a solubility six orders of magnitude lower ($(3.03 \pm 0.12)\times10^{-7}$ mol/kg at the same temperature [260].

4.2.2 Results

4.2.2.1 Initial proof of concept tests

The initial tests were conducted with a standard Pyrex glass bubbler, shown in Figure 4.3.

Figure 4.3 Example of liquid vapor separator with a Pyrex glass bubbler.

For the initial runs a standard solution of ionic mercury (1000±10 mg/L, Hatch) was used, which removed the need for the first two steps in the chemical process. The solution was diluted to the desired concentration before each test. Clean air was passed through the bubbler for approximately 30 min, allowing the LSPR peak to stabilize. Millipore, purified water (200 ml, 18MΩ) was added. The procedure was performed to determine the effect of water vapor on the LSPR peak position. The higher humidity will change the index of refraction surrounding the nanoparticles. The humidity change could mask shifts due to mercury. Water vapor, having a higher index of refraction then dry air, is expected to cause a red shift, while the mercury causes a blue shift. After the sensor reached an equilibrium state with the water vapor, stannous chloride was added at 10 times the amount of mercury to be added on a molar basis. Stannous chloride was added first to serve as a control and determine if it would be liberated from the water and change the LSPR peak of the sensor. Finally the mercury was added such that the final concentration would be at the desired level. This series of additions is shown in Figure 4.4 which displays the LSPR peak location. Figure 4.4 displays the gradual red shift of the LSPR peak as it asymptotically approaches a higher value after the addition of water. The

addition of stannous chloride does not influence this trend. Immediately after the introduction of mercury there is a rapid blue shift followed by a slow asymptotic shift back towards a higher wavelength, though still a lower wavelength then the initial value. The initial rapid blue shift is attributed to a high concentration of mercury causing a rapid blue shift upon adsorbing onto the nanoparticles. The slow red shift back may be caused by water vapor and additional species in the sample being liberated and raising the index of refraction.

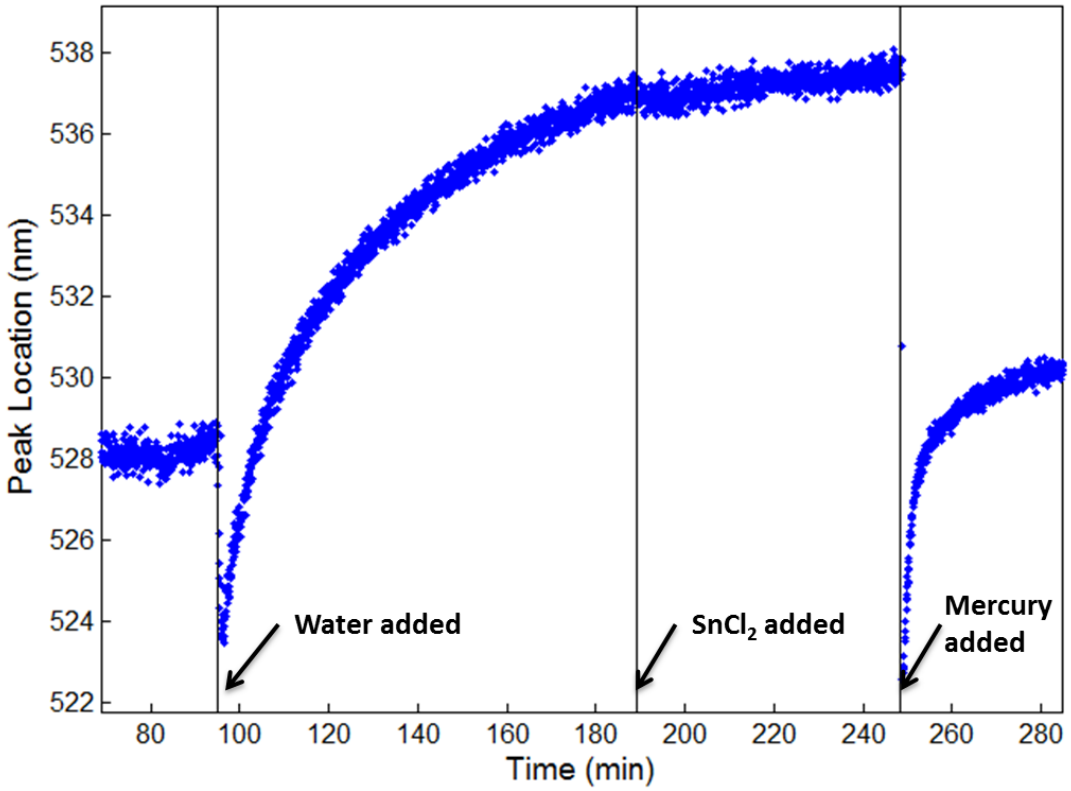

Figure 4.4. Change in LSPR peak during exposure procedure. Sample was exposure to 100 µg/L of mercury in a 200 ml volume.

Two lower concentrations were tested with the same total volume of 200 ml - 10 µg/L and 2 µg/L. The EPA drinking water standard is 2 µg/L [37]. The shift rate with time, the slope of the curve immediately after introduction of mercury (nm/min), was linearly proportional to the concentration and the total mass of mercury as shown in Figure 4.5.

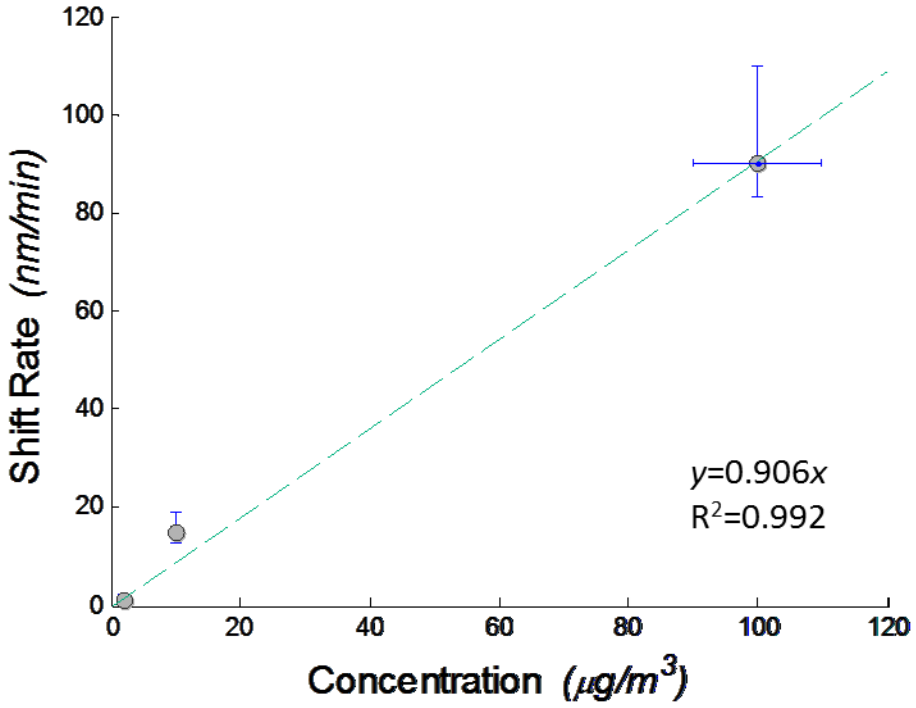

Figure 4.5. The relationship between the shift rate of the LSPR peak and the concentration of mercury in the sample. Least squares fit and R^2 are indicated. The data are for the initial runs where mercury was added last. Horizontal error bars are derived from uncertainty on the CavKit output. Vertical error bars are calculated from the standard deviation of the initial and final LSPR peak and the uncertainty of the time measurement. Details of this error calculation method are given in Chapter 3.

While adding the mercury last is a useful method for proving the validity of the method, it is not convenient for actual or field measurements. Adding mercury last dilutes the sample, raising the ultimate limit of detection. A revised method was developed which followed the full chemical redox procedure outlined previously. In this method the mercury standard was initially added to the sample volume, and the stannous chloride was added last. The LSPR peak of the sensor was allowed to equilibrate after the addition of the water and before the addition of the stannous chloride. Upon the addition of stannous chloride the LSPR peak blue shifted. The rate of this blue shift was found to be linearly proportional to concentration and in good agreement with the results from the previous 'Hg Last' method as indicated in Figure 4.6.

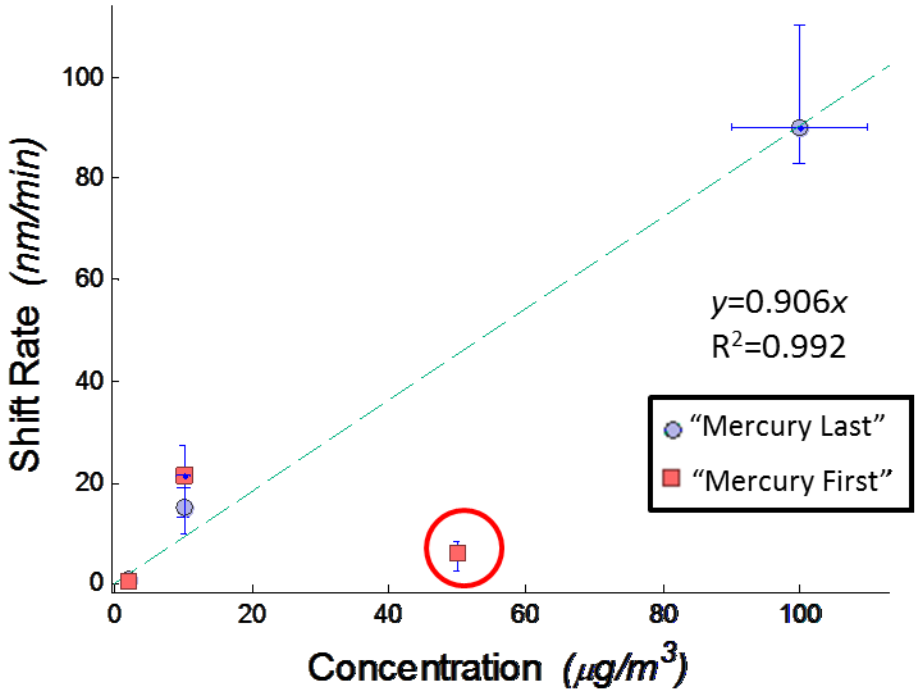

Figure 4.6. Comparison between the initial 'Mercury Last' method, and the revised method in which the stannous chloride was added last liberating the mercury. The highlighted point at 50 µg/L does not follow the trend. This deviation is attributed to contamination in the liquid vapor separator causing multiple reductions. Further details are given in the text.

The exception to the agreement with the trend was the last point tested at 50 µg/L. The response of this sensor was significantly slower than expected as if it was reading a much lower concentration of mercury. This result is attributed to contamination in the liquid vapor separator. Excess stannous chloride could have deposited on the walls of the separator which caused a rapid partial reduction and liberation of mercury upon the addition of mercury to the sample. The subsequent addition of stannous chloride liberated any residual mercury. The evidence for this interpretation is given in the trace of the peak location with time for the data set represented by the point highlighted in Figure 4.6 at 50 µg/L. This trace is shown in Figure 4.7.

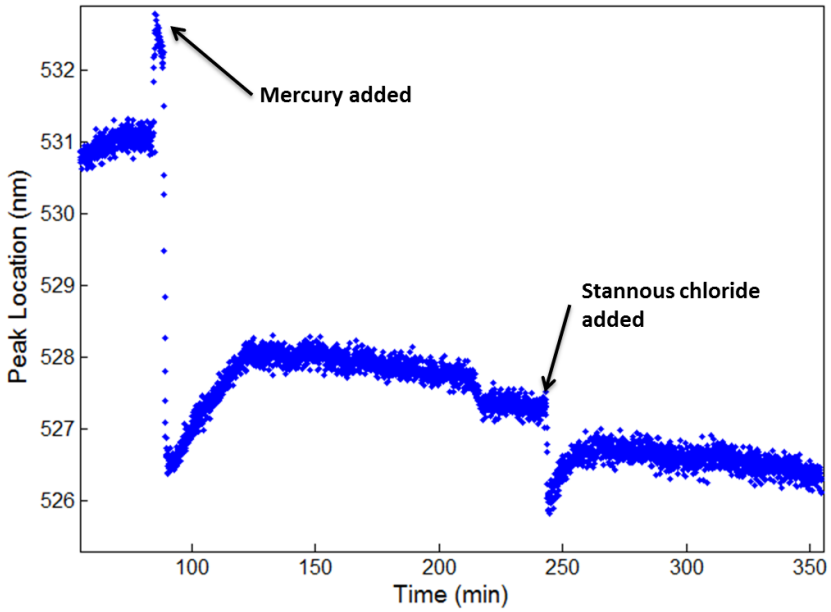

Figure 4.7. Trace of the LSPR peak location with time for highlighted test indicating a double blue shift upon each addition to the sample. The red shift immediately before the addition of mercury is attributed to changes in air flow caused by the addition of the mercury, as described in more detail in the text.

In addition to the double shifts shown in Figure 4.7, there is a small red shift immediately prior to the addition of the mercury, a shift attributed to changes in air flow as the laboratory bubbler needed to be physically opened to add mercury. Opening the bubbler creates an interruption in the constant air stream to the sensor and a somewhat unpredictable effect on the sensor response. The variability in the response is attributed to variations in the index of refraction associated with the changing air flow impacting the concentration of water vapor around the sensor. An unpredictable response is, of course, undesirable in a sensor especially if the relevant change follows immediately. Previously, the sensor was allowed to equalize after any disturbance, reducing the impact of any fluctuation.

To prevent carryover of stannous chloride after a run, a variety of cleaning protocols were attempted, including sequential washing with water, organic solvents, and dilute acids. They ultimately proved ineffective in solving the contamination issue. Contamination is a serious concern in all mercury measurements as evidenced by the details provided to address this issue in EPA method 1631 [73]. All of these reasons necessitated the abandoning of the configuration used for the proof of concept steps and replace the design with one which could plausibly be used for actual sample analysis.

4.2.2.2 Disposable separator tests step up

To overcome the difficulties with the prior system configuration a disposable liquid vapor separator was constructed from a pre-cleaned septum lidded glass jar. Certified trace metal free sample jars were purchased from VWR. The jars were modified to include a gas inlet and outlet, configured such that the path length of the gas through the sample fluid was maximized. The jars became lab built one-time-use bubblers. The jars had two additional advantages over traditional bubblers. First, the septum lid allows reagents to be added to the sample by syringe injection which does not interrupt the air flow. Second, the jars have a larger capacity, allowing for larger sample volumes and thus greater sensitivity[28]. The tubing immediately before the nozzle was reused though was flushed with a constant clean air flow between samples. An example of disposable sample jars and their position in a revised sample system is shown in Figure 4.8.

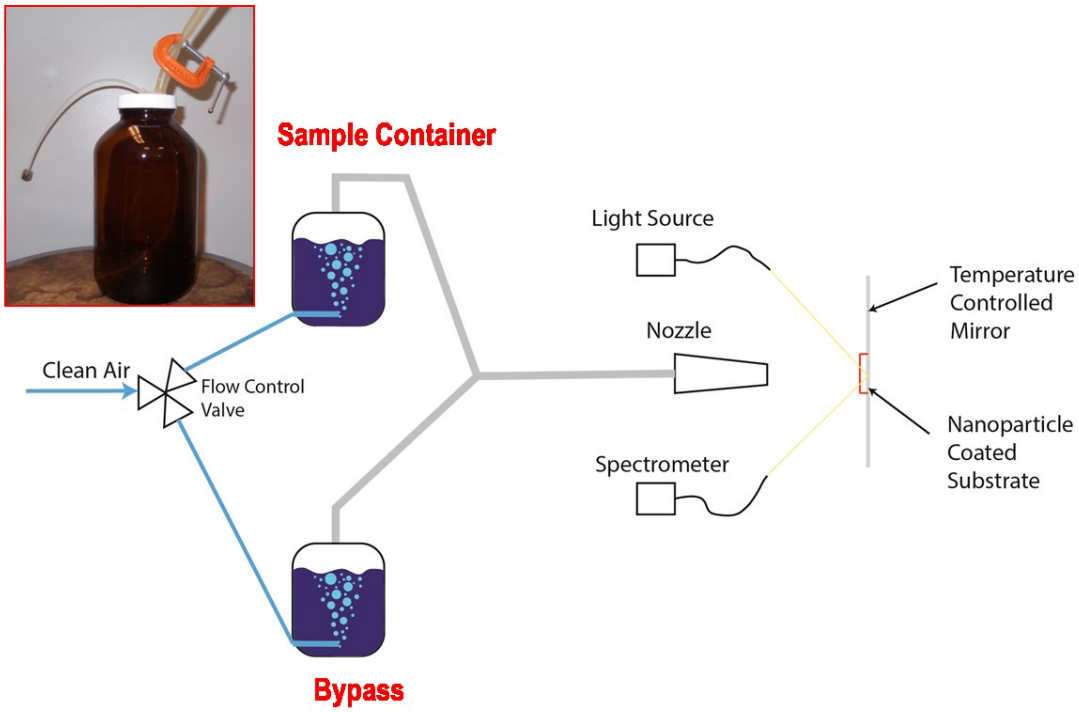

Figure 4.8. Revised flow system for disposable container liquid vapor separator configuration. The insert is an example of the lab built separator used for each run. This system also included a bypass for constant air flow, highlighted in red.

Besides the septum lids, air flow was maintained with the addition of a bypass line. The bypass, a clean identical jar filled with water, allowed the air flow to be continuous and with a

[28] The response of the sensor is proportional to the mass adsorbed. If the concentration is held constant, one way to increase the mercury mass flow past the sensor is to increase the volume. The gas phase sensors described in prior chapters benefit from what is in essence a limitless sample volume. The implications of limited sample volume on sensor performance and design are discussed in more detail in the latter sections of this chapter.

consistent humidity. The first two steps of the chemical process, oxidation with bromine monochloride and neutralization of halogens, could be completed in the sealed jar with all the air flow traveling through the bypass. The valve controlling flow would be actuated so that the flow passed through the sample and the sensor was allowed to equalize. Finally stannous chloride was added, reducing the mercury and liberating it for detection in the sensors. After each test the sample jar was disposed of.

4.2.2.3 Disposable separator results

Using the disposable container, sample concentrations of 0.5 µg/L, 2 µg/L, and 10 µg/L were tested. The focus of these tests was on lower concentrations bracketing the EPA drinking water standard to provide a more robust correlation around concentrations of interest. The results of these samples are shown in Figure 4.9.

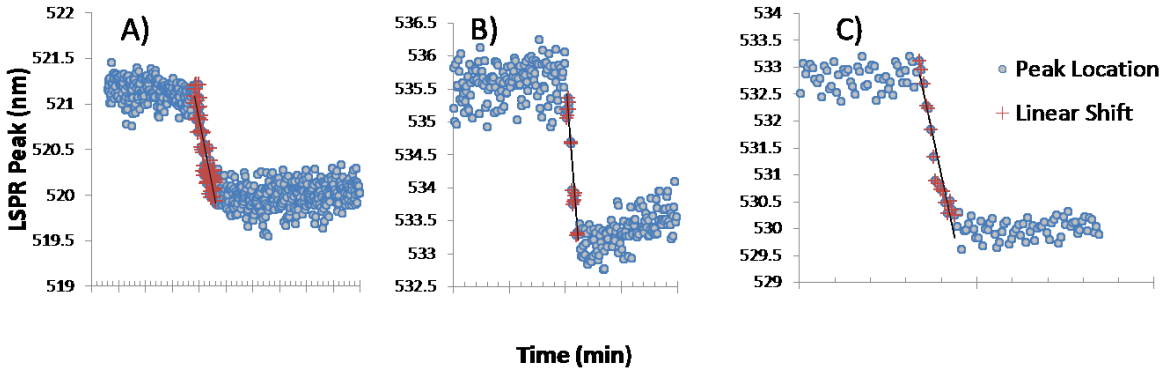

Figure 4.9. Trace of LSPR peak location with time for concentrations tested with the disposable flow set up. A), B), and C), corresponds to 0.5 µg/L, 2 µg/L, and 10 µg/L respectively.

The relationship between concentration and shift rate was again shown to be linear, shown in Figure 4.10.

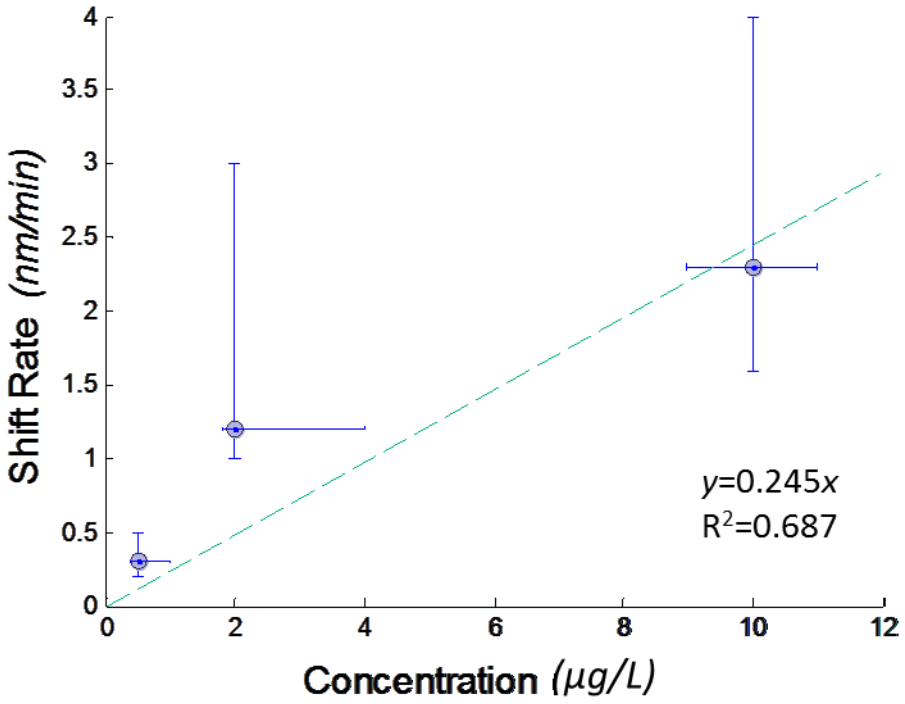

Figure 4.10. Linear relationship between concentration and shift rate for the disposable set up.

Each sample volume was 0.4L, thus the relationship would remain linear if the total mass of mercury is used as the independent, or x-axis, variable. The large volume did allow for a lower limit of detection, 0.5 µg/L which is one fourth the EPA limit.

A sample collected after the standard waste water treatment was procured from the Nevado Water Management District in California. The sample was tested in the same manner. No response was indicated. The sample was also tested in house by the water management district and shown to have a concentration of 15 ng/L. 15 ng/L is below the limit of detection based on the correlation developed. That concentration is expected to have a shift rate of 0.0036 nm/min, which would be masked by noise or thermal drift.

4.3 Discussion of aqueous mercury detection

The inability of the current design of the sensor to detect mercury at the low concentrations of interest to researchers and water managers highlights the need for improvement if nanoparticle based detection is to move outside the laboratory. The lower levels of detection, ng/L and pg/L, are only achieved in AFS systems by means of careful sample preparation and pre-concentration with a noble metal trap [73][22]. A similar system could be installed upstream of a gold nanoparticle transducer to trap, concentrated, and then thermally desorb mercury. This approach would negate one of the advantages of a nanoparticle system, though such a system is expected to still be simpler and cheaper to operate primarily by removing the need for an inert gas stream and the separate handling requirements of that stream.

4.3.1 Sensor improvement via mass transfer optimization

The higher limit of detection is partially related to the mass transfer being sub-optimal for this system. The geometry was originally designed for a vapor phase measurement where the sample volume is effectively unlimited. Unlimited sample volumes allowed the response time to be maximized at the expense of collection efficiency. Sample volume is not unlimited in these test, and in most aqueous measurements, thus it is vitally important to recover as much of the mercury as possible.

The collection efficiency, η_{col}, can be defined as the ratio of mercury adsorbed, $\dot{m}_{ad}$, onto the surface over the total amount of mercury which passes through the sensor, $\dot{m}_{tot}$:

$$\eta_{col} = \frac{\dot{m}_{ad}}{\dot{m}_{tot}} \qquad \text{(Equation 81)}$$

The mass adsorbed can be estimated from the diffusion coefficient, the substrate area, and the Sherwood number. The Sherwood number is a mass transfer Nusselt number and can be calculated from theory or empirical relationships. The details of calculating these values were presented in Chapter 2. The total mass flux is estimated from the concentration and the volumetric flow rate.

$$\eta_{col} = \frac{h_m A \Delta C}{\dot{\forall} C} \qquad \text{(Equation 82)}$$

$$h_m = \frac{Sh\, \mathfrak{D}}{L_{char}} \qquad \text{(Equation 83)}$$

where $h_m$is the mass transfer coefficient, A is the area of the sensor, ΔC is the concentration difference between the free stream and the sensor, $\dot{\forall}$ is the volumetric flow rate, Sh is the Sherwood number, $\mathfrak{D}$ is the diffusion coefficient, and L_{char} is the characteristic length, in this case the nozzle diameter. Assuming the concentration at the sensor surface is zero makes ΔC equal to the free stream concentration, and the collection efficiency becomes independent of concentration. There is some justification for this at early times as mercury will adsorb into the nanoparticles creating a depletion layer just above the sensor surface. This assumption means the calculated efficiency will be an upper bound. Values used for the calculation are given in Table 4-2

.

Table 4-1 Values used to calculate mass transfer efficiency.

Variable	Value	Units
Viscosity of Air[29] [230]	1.59×10^{-5}	m^2/s
Diffusion of Hg in Air [261]	0.14	cm^2/s
Density of Air [230]	1.16	kg/m^3
Nozzle Diameter	2	mm
Nozzle Height	25	mm
Substrate Area	20	mm^2
Flow Rate	10	LPM

Using these values yields a collection efficiency of just less than 1% (0.75%). It should be emphasized again that this is an upper bound both from the assumption about concentration and because the correlation assumes that all mercury transferred to the surface is adsorbed. All the mercury transferred to the surface will not be adsorbed, as the nanoparticles are in a sub-monolayer and the surface kinetics predicts less than complete collection (see Chapter 2). Even with this low mass transfer efficiency this method was able to directly detect mercury below the EPA standard which demonstrates the sensitivity of the nanoparticles.

The question is whether it possible to drastically improve the mass transfer efficiency of the system. If the mass transfer efficiency could be raised to 10%, the system could theoretically directly detect mercury at 5 ng/L. However, this level represents an order of magnitude improvement in efficiency, and at those low concentrations trace containments would be a larger concern.

[29] The actual nozzle arrangement is still in air as the mercury has been separated from the water by the gas stream at this point.

The first approach to improving the efficiency is to simply reduce the flow rate. Figure 4.11 shows that the collection efficiency is predicted to trend up with lower flow rates.

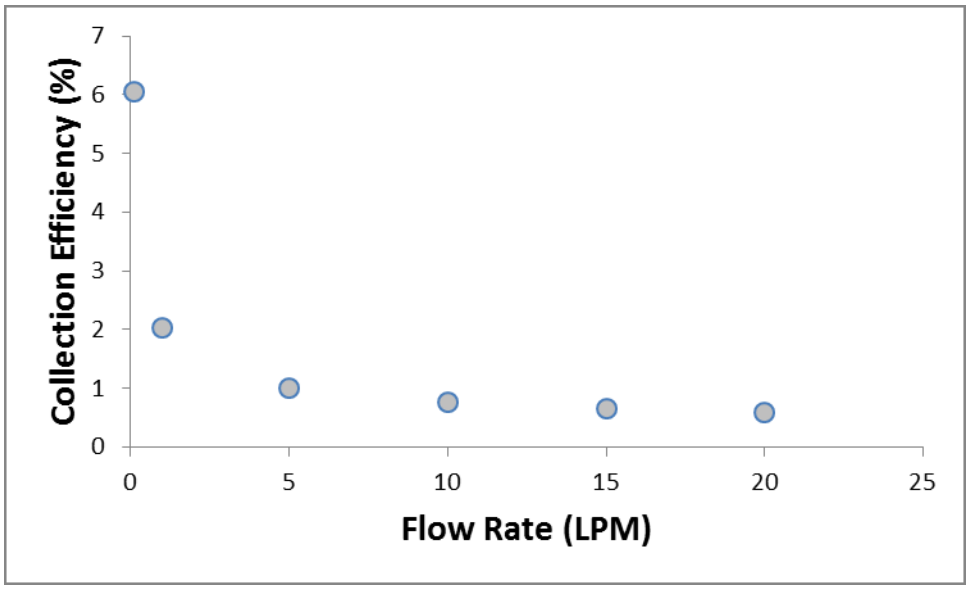

Figure 4.11 Dependence of collection efficiency on flow rate.

However, the flow rate cannot be set arbitrarily low. A creeping flow rate[30] would invalidate the correlation developed. Additionally, at low flow rates the time resolution of the sensor is poor, and mercury vapor liberated has more time to escape through poor seals or deposited on surfaces if the system is not properly maintained. Indeed, 1LPM is pushing the limit for the lower bounds of the Reynolds number limit for the correlation[31]. The geometry can be altered as well to maximize the efficiency. The geometry must remain reasonable and within the bounds of the correlation. Examining the effect of altering the geometry is shown in Figure 4.12.

[30] A creeping flow or Stokes flow is one in which the Reynolds number is much less than one. In this situation, the time scale of diffusive transport becomes comparable to the time scale of the convective transport, a small Peclet number, and the process could not be described by convective flow correlations [147]. The example of creeping flow is used more as thought experiment check on the validity of the results of the mass transfer efficiency calculations. In reality, the flow rate would be limited by the factors described in the text, time resolution, mercury losses, or other considerations, long before the Reynolds number entered the single digits.

[31] The correlation is valid between Reynolds numbers of 2,000 and 400,000 [147]. Details are given in Chapter 2.

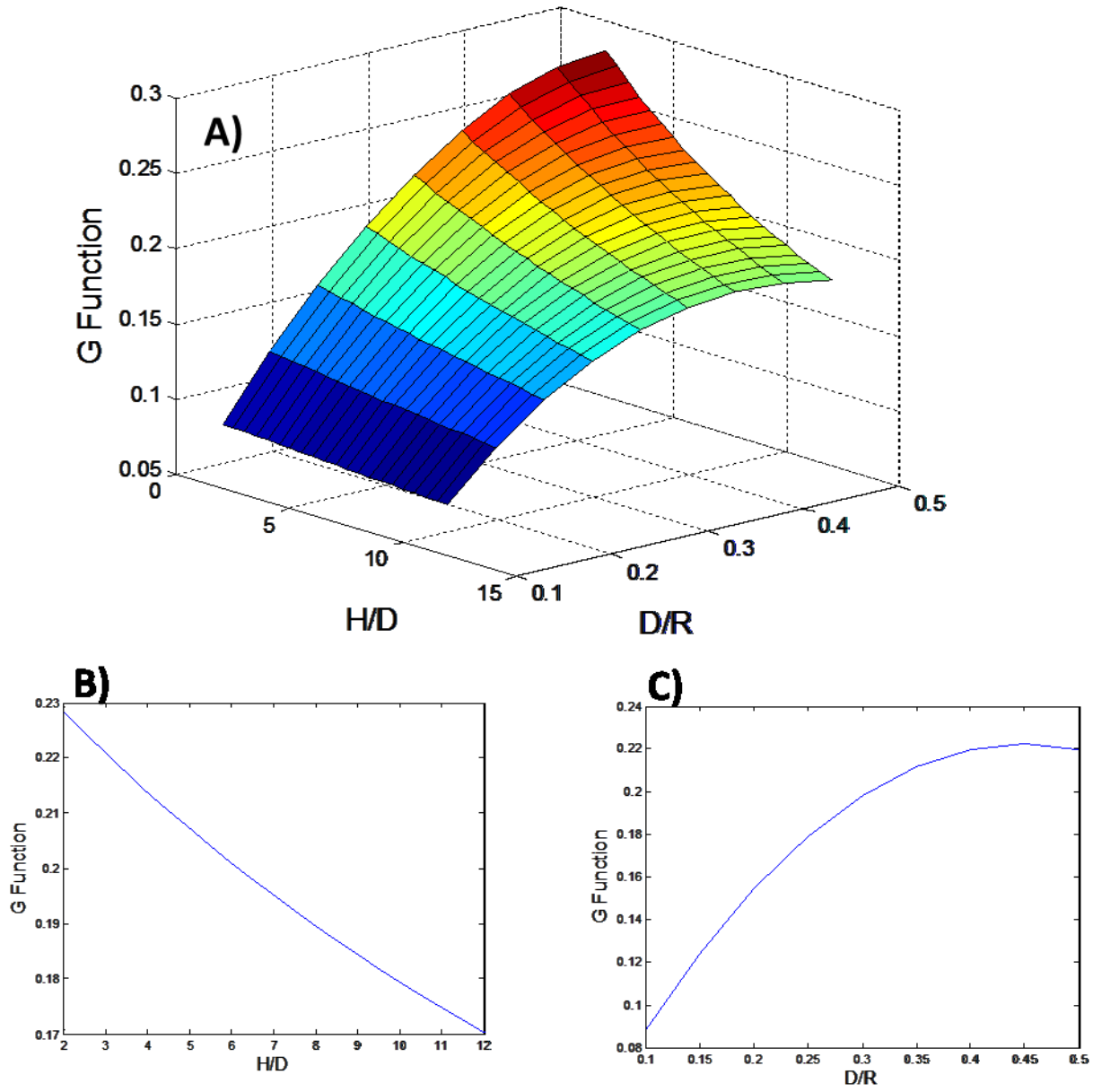

Figure 4.12 Examining the relationship between the geometric parameters, nozzle diameter, sensor area's radius, and height on the G function. The G function is the mass transfer correlation component dependent on the geometry. A) is the variation in the G function as both the ratio between height and diameter (H/D), and diameter and radius (D/R) change. B) is the trace of the G function as function of H/D at a fixed D/R of 0.3. C) is the trace of G function as a function of D/R at a fixed H/D of 6.5.

The mass transfer efficiency is more strongly dependent on the nozzle diameter with a maximum at around 0.4 times the radius of the sensor area. The efficiency is more weakly dependent on nozzle height. Efficiency increases as nozzle height becomes small compared to

nozzle diameter. Optimizing in this manner can yield more than an order of magnitude increase in collection efficiency to roughly 35% with the parameters as indicated in Table 4-2.

Table 4-2 Parameters for optimized mass collection efficiency for impinging flow set-up.

Variable	Value	Units
Nozzle Diameter	1	mm
Nozzle Height	2	mm
Sensor Area	20	mm^2
Volumetric Flow Rate	1	LPM

If a 35 fold increase in mass transfer is applied proportionally to lowering the limit of detection, the sensor could measure in the range of 15 ng/L. Several caveats are warranted for this analysis. First, it bears repeating that this is an upper bound of collection efficiency. Actually collection efficiency will likely be lower for the real sensor. Second, the parameters chosen in Table 4-2 are skirting the boundaries of the valid range of the correlation beyond which it may not predict the mass transfer correctly[32]. The trends are clear and agree with what one would intuit to be the optimal configuration for the system, i.e., a smaller nozzle closer to the sensor surface. Furthermore, the goal of this exercise was not to precisely predict the mass transfer rate of this sensor but to indicate the direction of design changes to increase sensor performance. Third and finally, the collection efficiency will be influenced by the active area of the sensor. Beyond optimizing the sticking coefficient and sensitivity of mercury adsorption on the gold nanoparticles, a larger area would trap more mercury possibly leading to a higher apparent collection efficiency. However, if that area is not active, in that the LSPR peak is not being monitored, this extra area will act as a sink, reducing the mercury which might contribute to a detectable LSPR change.

Gains in efficiency could be realized by altering the fluid properties, by increasing the diffusion coefficient, decreasing the viscosity, altering the carrier gas, or decreasing the pressure. Other geometries were investigated, namely laminar flow across a plate and a slotted, as opposed to a round, nozzle. These geometries were found to have a lower collection efficiency than a round nozzle impinging jet.

4.3.2 Sensor improvement via a continuous flow system

Another method for improving the performance would be to switch to a continuous flow system, removing some of the limitations on sample volume. Several groups [262][263] have reported automated on-line systems for sample processing and detection of aqueous mercury. While this increases the complexity of the system and requires careful calibration of the flow rate for the various reagents, a property calibrated and ruggedized design was used for in field measurements with good agreement to laboratory tests [263]. These systems employed a

[32] The correlation is valid for a height to nozzle diameter ratio between 2 and 12. And a sensor area radius to nozzle diameter ratio between 2.5 and 7.5 [147]. Details are given in Chapter 2.

CVAFS as the analytical heart of the device which could be replaced with a nanoparticle based sensor.

An intriguing possibility is to use a gold catalyst in place of the sequential oxidization-pacification-reduction scheme. This strategy would remove the need for additional hazardous chemicals and drastically simplify sample handling. While gold is commonly thought of as chemically inert, several works [264][265][266][267] have shown catalytic activity with gold. Typically the catalytic reaction is controlled via nano-scaling the gold, raising the temperature, or providing a favorable substrate. Several groups have shown gold to be able to evolve various species into elemental mercury [268][269].

Aeschliman and Norton [268] investigated the effect of temperature on a gold trap for the collection and pre-concentration of various species of mercury (elemental, ionic, and dimethylmercury). They found slight variations in the adsorption of mercury with temperature and a uniform release of mercury from the trap at around 523 K. All of the mercury released was elemental regardless of the species which was adsorbed by the trap. Species were introduced individually by means of a gas calibration standard. Extending this work Zierhut et al. [269] showed that gold surfaces would retain a variety of mercury species (elemental, ionic, and methylmercury) directly from solution in water. They attributed adsorption of the non-elemental mercury species to catalytic activity of nanostructured gold. The nanostructure of the gold was achieved by adsorbing then thermally desorbing elemental gold. Morphological investigations with an AFM indicated an increase in surface roughness for the nanostructured gold from a variation of less than 2 nm to a variation of between 15 nm and 50 nm. They also showed formation of gold islands, in agreement with Levlin et al.'s work [128]. The same group extended this work to create a reagent free automated flow system [270]. Nanostructured gold in a column is used to pre-concentrate mercury before analysis with a CVAFS. This system was validated with a standard and several field samples measuring mercury concentrations down to 5 ng/L.

4.3.3 Extension of results to solid samples

The third matrix of interest for mercury measurements is solids. These include sediment, biological samples, soils, waste sludge, geologic samples, coal, and others. Most measurements of mercury levels in solid matrixes are accomplished by a method similar to the one described in this section for aqueous samples with a preliminary step involving the digestion of the solid [255]. The solid is decomposed usually with an acid treatment as outlined in the standardized EPA Method 1631 Appendix A. Once digested the sample is processed through an oxidation-halogen pacification-reduction scheme and then quantified by means of a CVAFS. Alternative means of digestions have been investigated, such as microwave assisted acid bath [271][272] or thermal decomposition [273]. There is no reason why the actual mercury measurement could not be performed by a nanoparticle sensor as opposed to a CVAFS. Solid samples may present unique changes in terms of contamination and selectivity of the sensor. These are challenges which a CVAFS has to overcome as well. Indeed, a nanoparticle sensor may be more adaptable in overcoming these challenges as it does not require a particular gas, and protective coatings

could be applied to the particles. The nanoparticle sensor still retains its advantages in cost and simplicity.

4.4 Conclusions on aqueous mercury detection with gold nanoparticles

The work described in this section extends the capabilities of gold nanoparticle based sensors to aqueous environments. The sensors are able to directly measure concentrations below the EPA limit of 2 µg/L, within 10 minutes after the addition of mercury. Further work is needed to improve the reproducibility of the sensor and validate the correlation between sensor response and concentration. However, the results presented indicate that nanoparticle based aqueous mercury sensors have the potential to be an inexpensive and efficient alternative to established techniques.

A disposable sample treatment system is described which reduces contamination and improves performance. Possible means of improving sensor performance utilizing mass transfer relationships and novel catalysis based sample pretreatment are presented. Finally, the possibility of extending this methodology to solid samples is examined and several possible advantages of using a nanoparticle based sensor for solid measurements were elucidated.

5. Conclusion

Mercury pollution is an issue of pressing concern. Mercury is third on the Agency for Toxic Substance and Disease Registry's list of priority substance [274]. There are still unaddressed questions for policy makers, regulators, and researchers. Additional research is warranted in: the global transport of mercury [42][251][275], concentration levels in remote aquatic locations [243], speciation [276], methylation and bioaccumulation of mercury [242], concentrations in fish species [249][277], exposure assessment [40], and dose response [7][18][278]. Regulators in the United States are implementing rules to control mercury from fossil fuel combustion, the largest single source of anthropogenic mercury emissions [66]. Globally, negotiations are ongoing concerning treaties to limit emission; the most recent round has specifically called out artisanal mining as an area of concern [279][280].

Better measurement techniques would positively impact research, regulation, and policy around mercury. Robust, inexpensive and straightforward to operate sensors could be deployed more widely than current cold vapor atomic fluoresces spectroscopy based systems. Wider deployment of sensors could help address some of the remaining questions about mercury transport and concentration levels in remote locations. Improved sensors could influence regulation and policy, apart from new information that could be gleaned from research studies. Sensors which allow accurate speciation measurements could provide for more real-time monitoring of methylmercury levels in the wide variety of fish species consumed. Robust and easy to operate systems could be deployed in remote communities such as those engaged in artisanal mining. The work presented here has shown that noble metal nanoparticle based mercury sensors are a promising alternative to current systems. Additionally, some of the phenomenon and techniques developed here could be applied more broadly to related investigations.

Gold nanoparticle sensors are an ideal transducer for a mercury sensor. The localized surface plasmon resonance (LSPR) peak is extremely sensitive to changes in the composition of the particles; 1-2% mercury by mass on a nanorod, or 4.5 attograms, causes a roughly 4 nm shift in LSPR [281]. Mercury readily adsorbs onto the surface of gold nanoparticles causing a blue shift in the LSPR peak. Developments in recent years have increased the facility in and control of the synthesis and deposition of these nanoparticles, thus they can be reliably fabricated into a variety of sensor geometries.

The second chapter of this dissertation investigated some of the physical phenomena, specifically mass transport and adsorption kinetics, which underlie the response of gold nanoparticle based mercury sensors. The chapter gave a theoretical basis for the application of tools developed in the field of heat transfer to mass transfer problems of interest in gas phase sensors. These correlations were then utilized to improve sensor performance by implementing an impinging jet flow geometry which reduced response time. Utilizing an impinging jet sensor with gold nanospheres, the kinetics of mercury adsorption was investigated, finding that the adsorption is most closely modeled as a Langmuir type isotherm. Estimates for the adsorption and desorption constants were derived which may prove useful in the design of new sensors. To deconvolve the effects from mass transfer and adsorption kinetics a novel model based on

an analogous resistor- capacitor direct current circuit was developed. This model was applied to the experimental data of mercury adsorption on gold nanospheres with three different surface coatings, bare, 4-tert-butylthiophenol, and citrate/ polyethylenamine. For the bare and 4-tert-butylthiophenol coated particles the model yielded a flow rate dependent mass transfer resistance in good agreement with established correlations for impinging jet mass transfer. High variability and lack of data for the citrate/polyethyleneamine coated particles hampered validation of the results. However, in all cases the model provided an estimate for the forward adsorption constant which was independent of flow rate.

Derivation of the adsorption constants utilizing LSPR data is novel with only a few investigations having been conducted. The procedures and models developed here could be applied to other sorbate/sorbent systems. In particular the circuit approach to separating mass transfer effects and kinetics should be applied and tested with other systems. This approach could help validate that response is due to surface kinetics as opposed to mass transport limitations. Designers and researchers working with sensors could use the results of this model to improve the performance, as mass transfer effects are often overlooked as a means of sensor improvement. Mass transfer results were used in chapter 2 and chapter 4 to improve performance based on time response and collection efficiency of the sensors. Specific to the adsorption of mercury on gold nanoparticles, further work is needed on refining the model to extract thermodynamic and desorption constants, which could be accomplished with a similar experimental apparatus providing there is finer control over temperature.

Chapter 3 extended mercury sensing with gold nanoparticles to a fiber optic based system. Fiber optic cable has proven to be a versatile platform for a variety of sensing applications including plasmonic sensors for biological and chemical species [16][17]. A bent fiber optic cable was decorated with gold nanorods which have a sensitive and pronounced longitudinal LSPR peak; the fiber was bent to enhance the interaction of light with the nanorods. This sensor was able to directly detect mercury in air down to 1 $\mu g/m^3$ without any preconcentration. The sensor is regenerable and stable against small fluctuations in temperature (<1 K). Besides the high sensitivity of this system, the fiber optic sensor allows for measurements in locations which may have space constraints making traditional sensors impractical. The sensor is inexpensive, and the ubiquity of fiber optics in communications provides extensive peripherals that could be incorporated into sensor design.

Further work is necessary to translate this work into a working sensor capable of measurements in the ambient or at coal fired power plants. Ambient mercury concentrations are typically lower than the limit measured, on the order of ng/m^3 [52]. Additional work would be necessary to improve the limit of detection, perhaps with the inclusion of a preconcentration system or optimization of mass transfer, though the more complicated geometry of the fiber optic sensor and their delicacy when declad impose some limits on methods of mass flow optimization. The selectivity of the sensor needs to be investigated if they are to be deployed at coal fired power plants. The response of the sensor to the various

products of combustion should be recorded. Selective coatings or a reference line[33] could be added to a system in a coal fired power plant to reduce the confounding result of other species [282]. The regeneration of the sensor performed here was not quantified well, or repeated multiple times, thus additional work is warranted to solidify the best practices for this procedure. Additionally, the method employed, blowing clean dry hot air over the fiber optic, may not be the most practical. A heating element incorporated into the body of the sensor may prove more efficient and easier to control. From an applications standpoint, it may be warranted to investigate areas of the mercury cycle which are under served by current measurement techniques and which may be better served with fiber optic sensors. This effort would help clarify the design challenges which need to be addressed.

The nanoparticle fiber optic sensor is a versatile platform and the methods presented here for fabrication and attachment of gold nanorods could be applied to other systems. The computationally straightforward investigations of the response of noble metal nanorods and nanospheres presented here could provide a guide for selecting the nanoparticle most suited for a specific application.

Chapter 4 provided proof of concept that noble metal nanoparticle could be used for the detection of aqueous mercury. The detection of mercury in water is an important concern and an area of active research [243]. Mercury transport to humans is complex, but aquatic environments are a key component in exposures from seafood [240]. Improved measurements of mercury in water, that include speciation, would be a valuable resource to researchers, regulators, policy makers, and consumers. Current detection methods are based around CVAFS a costly and complicated system. The work here showed that established protocols for the chemical oxidation, reduction and liberation of mercury could be combined with a nanoparticle transducer. A disposable liquid vapor separator was developed which prevented erroneous responses from reagent build up. The disposable separator also ameliorates some of the concern for contamination as each separator is certified trace metal free before the introduction of the sample. The response of the sensor was linear with concentration and provided detection below the EPA's drinking water limit 2 µg/L [37].

The results described here are promising for the use of nanoparticles as an inexpensive, robust, regenerable, and sensitive transducer for aqueous mercury detection. However, more work is need. These are initial results and further work is necessary to validate the correlation and determine the repeatability of the response. Chapter 3 also discussed methods for improving the performance of the sensor using the mass transfer relationships for this geometry to maximize the efficiency of mercury collection. These methods should be implemented in the next phase of testing, preferably with more robust temperature control on the gold nanoparticle film. Initial results with a field sample were promising, though the concentration was below the limit of detection. Further testing is warranted to determine the effect, if any, of other possible species in field samples. Other procedures to separate the mercury, for example

[33] A reference line is an identical sensor which is only exposed to clean air or limited number of species (i.e. air scrubbed of mercury). The response of the reference sensor can be used to calibrate the response of the actual mercury sensor in order to remove error from the other species.

thermal- or catalysis-based, should be evaluated for inclusion with a nanoparticle sensor, as they may prove more efficient and straightforward. A different procedure would also remove the need for the hazardous chemicals used in the oxidation/reduction process, and it may also allow for continuous monitoring.

Modification of the sample processing procedure may allow for determination of the speciation of mercury in the sample. Omitting a step could selectively remove only the elemental, ionic, or methylated mercury present. Further modification could extend the capabilities of this system to measurements in solids such as soil or fish tissue. Existing sample preparation techniques are very similar to procedure presented here with the inclusion of a preliminary step to digest the solid sample [255]. The results presented here provide the initial proof that a gold nanoparticle sensor could provide aqueous measurements and suggest that capabilities could be extend to other samples phases.

The results presented in this dissertation elucidate some of the fundamental phenomena underlying the operations of gold nanoparticle mercury sensors. This work then extended the capabilities of gold nanoparticle mercury sensors to novel systems: fiber optic systems that directly detect mercury in the range of coal fired power plant flue gas, and aqueous systems with detection limits below the EPA standard. Relationships derived, here based on fundamental principles of mass transfer and surface kinetics, suggest the means through which further improvement could be made, not just to mercury sensors but to a wide range of gas phase sensors. The LSPR response analysis tools developed could be used to study a variety of adsorption based system. Plasmonic mercury sensors can help protect the health of people around the globe. The techniques and results here can be extended beyond mercury detection to improve sensors in a variety of fields.

References

[1] L. J. Goldwater, *Mercury A History of Quicksilver*. Baltimore, Maryland: York Press, 1972.

[2] The United Nations Environment Programme, *The Global Atmospheric Mercury Assessment: Sources, Emissions and Transport.* Geneva, Switzerland, 2008.

[3] S. A. Counter, "Boston.com / News / Boston Globe / Health / Science / Whitening skin can be deadly." [Online]. Available: http://www.boston.com/news/globe/health_science/articles/2003/12/16/whitening_skin_can_be_deadly/. [Accessed: 18-Nov-2011].

[4] D. Mapes, "Suffering for beauty has ancient roots - Health - msnbc.com." [Online]. Available: http://www.msnbc.msn.com/id/22546056/ns/health/t/suffering-beauty-has-ancient-roots/#.TsXnUfIXuP0. [Accessed: 18-Nov-2011].

[5] China Ministry of Culture, "Qin Shihuang." [Online]. Available: http://www.chinaculture.org/gb/en_aboutchina/2003-09/24/content_22854.htm. [Accessed: 18-Nov-2011].

[6] T. W. Clarkson, "The Toxicology of Mercury," *Crit. Rev. Clin. Lab. Sci.*, vol. 34, no. 4, pp. 369–403, Jan. 1997.

[7] P. Grandjean, H. Satoh, K. Murata, and K. Eto, "Adverse Effects of Methylmercury: Environmental Health Research Implications," *Environ. Health Perspect.*, vol. 118, pp. 1137–1145, Aug. 2010.

[8] D. Hunter, R. R. Bomford, and D. S. Russell, "Poisoning by methyl mercury compounds," *QJM*, vol. 9, no. 3, pp. 193–226, 1940.

[9] M. Harada, "Minamata Disease: Methylmercury Poisoning in Japan Caused by Environmental Pollution," *Crit. Rev. Toxicol.*, vol. 25, pp. 1–24, Jan. 1995.

[10] F. Bakir, S. F. Damluji, L. Amin-Zaki, M. Murtadha, A. Khalidi, N. Y. Al-Rawi, S. Tikriti, H. I. Dhahir, T. W. Clarkson, J. C. Smith, and R. A. Doherty, "Methylmercury Poisoning in Iraq," *Science*, vol. 181, pp. 230–241, Jul. 1973.

[11] H. RUSTAM and T. HAMDI, "METHYL MERCURY POISONING IN IRAQ A NEUROLOGICAL STUDY," *Brain*, vol. 97, no. 1, pp. 499 –510, Jan. 1974.

[12] M. Aschner and J. L. Aschner, "Mercury neurotoxicity: mechanisms of blood-brain barrier transport," *Neurosci. Biobehav. Rev.*, vol. 14, no. 2, pp. 169–176, 1990.

[13] B. H. Choi, "The effects of methylmercury on the developing brain," *Prog. Neurobiol.*, vol. 32, no. 6, pp. 447–470, 1989.

[14] D. Rice and S. Barone, "Critical periods of vulnerability for the developing nervous system: evidence from humans and animal models.," *Environ. Health Perspect.*, vol. 108, no. Suppl 3, pp. 511–533, Jun. 2000.

[15] S. A. Counter and L. H. Buchanan, "Mercury exposure in children: a review," *Toxicol. Appl. Pharmacol.*, vol. 198, no. 2, pp. 209–230, 2004.

[16] K. S. Crump, T. Kjellström, A. M. Shipp, A. Silvers, and A. Stewart, "Influence of prenatal mercury exposure upon scholastic and psychological test performance: benchmark analysis of a New Zealand cohort," *Risk Anal.*, vol. 18, no. 6, pp. 701–713, 1998.

[17] N. R. C. (US). B. on E. Studies and N. R. C. (US). C. on the T. E. of Methylmercury, *Toxicological effects of methylmercury*. Natl Academy Pr, 2000.

[18] P. Grandjean, P. Weihe, R. F. White, and F. Debes, "Cognitive Performance of Children Prenatally Exposed to 'Safe' Levels of Methylmercury," *Environ. Res.*, vol. 77, no. 2, pp. 165–172, May 1998.

[19] G. J. Myers, P. W. Davidson, C. Cox, C. F. Shamlaye, D. Palumbo, E. Cernichiari, J. Sloane-Reeves, G. E. Wilding, J. Kost, L.-S. Huang, and T. W. Clarkson, "Prenatal methylmercury exposure from ocean fish consumption in the Seychelles child development study," *The Lancet*, vol. 361, no. 9370, pp. 1686–1692, May 2003.

[20] P. Grandjean and R. F. White, “Effects of methylmercury exposure on neurodevelopment,” *Jama J. Am. Med. Assoc.*, vol. 281, no. 10, pp. 896–897, 1999.
[21] N. V. C. Ralston, C. R. Ralston, J. L. Blackwell, and L. J. Raymond, “Dietary and tissue selenium in relation to methylmercury toxicity,” *Neurotoxicology*, vol. 29, no. 5, pp. 802–811, 2008.
[22] M. L. A. Cuvin-Aralar and R. W. Furness, “Mercury and selenium interaction: A review,” *Ecotoxicol. Environ. Saf.*, vol. 21, no. 3, pp. 348–364, Jun. 1991.
[23] A. L. Choi, E. Budtz-Jørgensen, P. J. Jørgensen, U. Steuerwald, F. Debes, P. Weihe, and P. Grandjean, “Selenium as a potential protective factor against mercury developmental neurotoxicity,” *Environ. Res.*, vol. 107, no. 1, pp. 45–52, May 2008.
[24] G. E. Mckeown-Eyssen, J. RUEDY, and A. NEIMS, “Methyl mercury exposure in northern Quebec: II. Neurologic findings in children,” *Am. J. Epidemiol.*, vol. 118, no. 4, pp. 470–479, 1983.
[25] D. O. Marsh, M. D. Turner, J. C. Smith, P. Allen, and N. Richdale, “Fetal methylmercury study in a Peruvian fish-eating population.,” *Neurotoxicology*, vol. 16, no. 4, p. 717, 1995.
[26] G. J. Myers, P. W. Davidson, C. Cox, C. Shamlaye, E. Cernichiari, and T. W. Clarkson, “Twenty-seven years studying the human neurotoxicity of methylmercury exposure,” *Environ. Res.*, vol. 83, no. 3, pp. 275–285, 2000.
[27] K. Murata, P. Weihe, A. Renzoni, F. Debes, R. Vasconcelos, F. Zino, S. Araki, P. J. JØrgensen, R. F. White, and P. Grandjean, “Delayed evoked potentials in children exposed to methylmercury from seafood.,” *Neurotoxicol. Teratol.*, vol. 21, no. 4, p. 343, 1999.
[28] K. Murata, P. Weihe, S. Araki, E. Budtz-JØrgensen, and P. Grandjean, “Evoked potentials in Faroese children prenatally exposed to methylmercury.,” *Neurotoxicol. Teratol.*, vol. 21, no. 4, p. 471, 1999.
[29] S. Cordier, M. Garel, L. Mandereau, H. Morcel, P. Doineau, S. Gosme-Seguret, D. Josse, R. White, and C. Amiel-Tison, “Neurodevelopmental investigations among methylmercury-exposed children in French Guiana,” *Environ. Res.*, vol. 89, no. 1, pp. 1–11, 2002.
[30] E. Oken, R. O. Wright, K. P. Kleinman, D. Bellinger, C. J. Amarasiriwardena, H. Hu, J. W. Rich-Edwards, and M. W. Gillman, “Maternal Fish Consumption, Hair Mercury, and Infant Cognition in a U.S. Cohort,” *Environ. Health Perspect.*, vol. 113, no. 10, pp. 1376–1380, Oct. 2005.
[31] P. Grandjean, “Mercury risks: controversy or just uncertainty?,” *Public Health Rep.*, vol. 114, no. 6, p. 512, 1999.
[32] N. Agrwal, “Economic Analysis of Toxic Substances Control Act Section 403: Lead-Based Paint Hazard Standards.” Ecnomic and Policy Analyssi Branch, EPA, 21-Dec-2000.
[33] D. S. Salkever, “Updated Estimates of Earnings Benefits from Reduced Exposure of Children to Environmental Lead,” *Environ. Res.*, vol. 70, no. 1, pp. 1–6, Jul. 1995.
[34] K. Sundseth, J. M. Pacyna, E. G. Pacyna, J. Munthe, M. Belhaj, and S. Astrom, “Economic benefits from decreased mercury emissions: Projections for 2020,” *J. Clean. Prod.*, vol. 18, no. 4, pp. 386–394, 2010.
[35] U. E. O. N. I. R. I. S. (IRIS), “Methylmercury (MeHg) (CASRN 22967-92-6) | IRIS | US EPA.” [Online]. Available: http://www.epa.gov/iris/subst/0073.htm. [Accessed: 13-Jan-2013].
[36] “CDC - Mercury - NIOSH Workplace Safety and Health Topic.” [Online]. Available: http://www.cdc.gov/niosh/topics/mercury/. [Accessed: 14-Jan-2013].
[37] O. US EPA, “Basic Information about Mercury (inorganic) in Drinking Water.” [Online]. Available: http://water.epa.gov/drink/contaminants/basicinformation/mercury.cfm. [Accessed: 31-Jan-2013].
[38] World Health Organization, *Air Quality Guidelines*. World Health Organization, 2000.

[39] K. R. Mahaffey, R. P. Clickner, and C. C. Bodurow, “Blood organic mercury and dietary mercury intake: National Health and Nutrition Examination Survey, 1999 and 2000.,” *Environ. Health Perspect.*, vol. 112, no. 5, p. 562, 2004.

[40] K. R. Mahaffey, R. P. Clickner, and R. A. Jeffries, “Adult women’s blood mercury concentrations vary regionally in the United States: association with patterns of fish consumption (NHANES 1999–2004),” *Environ. Health Perspect.*, vol. 117, no. 1, p. 47, 2009.

[41] C. G. Lyketsos, “Should pregnant women avoid eating fish? Lessons from the Seychelles,” *The Lancet*, vol. 361, no. 9370, pp. 1667–1668, May 2003.

[42] UNEP, “Global Atmospheric Mercury Assessment: Sources, Emissions and Transport.” [Online]. Available: http://www.unep.org/hazardoussubstances/Mercury/MercuryPublications/GlobalAtmosphericMercuryAssessmentSourcesEm/tabid/3618/language/en-US/Default.aspx. [Accessed: 12-Nov-2011].

[43] O. Malm, “Gold mining as a source of mercury exposure in the Brazilian Amazon,” *Environ. Res.*, vol. 77, no. 2, pp. 73–78, 1998.

[44] “WHO | Mercury,” *WHO*. [Online]. Available: http://www.who.int/ipcs/assessment/public_health/mercury/en/index.html. [Accessed: 14-Jan-2013].

[45] F. Sprovieri, N. Pirrone, R. P. Mason, and M. Andersson, “Spatial coverage and temporal trends of over-water, air-surface exchange, surface and deep sea water mercury measurements,” in in *Mercury Fate and Transport in the Global Atmosphere*, R. Mason and N. Pirrone, Eds. Springer US, 2009, pp. 323–380.

[46] B. Hall, “The gas phase oxidation of elemental mercury by ozone,” *Water. Air. Soil Pollut.*, vol. 80, no. 1, pp. 301–315, 1995.

[47] F. Slemr, G. Schuster, and W. Seiler, “Distribution, speciation, and budget of atmospheric mercury,” *J. Atmospheric Chem.*, vol. 3, no. 4, pp. 407–434, 1985.

[48] W. Seiler, C. Eberling, and F. Slemr, “Global distribution of gaseous mercury in the troposphere,” *Pure Appl. Geophys.*, vol. 118, no. 2, pp. 964–974, 1980.

[49] D. Jaffe, E. Prestbo, P. Swartzendruber, P. Weiss-Penzias, S. Kato, A. Takami, S. Hatakeyama, and Y. Kajii, “Export of atmospheric mercury from Asia,” *Atmos. Environ.*, vol. 39, no. 17, pp. 3029–3038, 2005.

[50] P. Weiss-Penzias, D. A. Jaffe, P. Swartzendruber, J. B. Dennison, D. Chand, W. Hafner, and E. Prestbo, “Observations of Asian air pollution in the free troposphere at Mount Bachelor Observatory during the spring of 2004,” *J. Geophys. Res.*, vol. 111, no. D10, p. D10304, 2006.

[51] P. Weiss-Penzias, D. Jaffe, P. Swartzendruber, W. Hafner, D. Chand, and E. Prestbo, “Quantifying Asian and biomass burning sources of mercury using the Hg/CO ratio in pollution plumes observed at the Mount Bachelor Observatory,” *Atmos. Environ.*, vol. 41, no. 21, pp. 4366–4379, 2007.

[52] D. Jaffe and S. Strode, “Sources, fate and transport of atmospheric mercury from Asia,” *Environ. Chem.*, vol. 5, no. 2, pp. 121–126, 2008.

[53] R. P. Mason, J. R. Reinfelder, and F. M. M. Morel, “Uptake, toxicity, and trophic transfer of mercury in a coastal diatom,” *Environ. Sci. Technol.*, vol. 30, no. 6, pp. 1835–1845, 1996.

[54] R. P. Mason, K. R. Rolfhus, and W. F. Fitzgerald, “Mercury in the North Atlantic,” *Mar. Chem.*, vol. 61, no. 1, pp. 37–53, 1998.

[55] G. A. Gill and W. F. Fitzgerald, “Mercury sampling of open ocean waters at the picomolar level,” *Deep Sea Res. Part Ocean. Res. Pap.*, vol. 32, no. 3, pp. 287–297, 1985.

[56] C. for F. S. and A. Nutrition, “Methylmercury - Mercury Concentrations in Fish: FDA Monitoring Program.” [Online]. Available: http://www.fda.gov/Food/FoodSafety/Product-SpecificInformation/Seafood/FoodbornePathogensContaminants/Methylmercury/ucm191007.htm. [Accessed: 15-Jan-2013].

[57] R. A. Bodaly, J. W. M. Rudd, R. J. P. Fudge, and C. A. Kelly, “Mercury concentrations in fish related to size of remote Canadian Shield lakes,” *Can. J. Fish. Aquat. Sci.*, vol. 50, no. 5, pp. 980–987, 1993.

[58] G. Cabana, A. Tremblay, J. Kalff, and J. B. Rasmussen, “Pelagic food chain structure in Ontario lakes: a determinant of mercury levels in lake trout (Salvelinus namaycush),” *Can. J. Fish. Aquat. Sci.*, vol. 51, no. 2, pp. 381–389, 1994.

[59] D. J. Spry and J. G. Wiener, “Metal bioavailability and toxicity to fish in low-alkalinity lakes: a critical review,” *Environ. Pollut.*, vol. 71, no. 2, pp. 243–304, 1991.

[60] R. P. Mason, J. R. Reinfelder, and F. M. M. Morel, “Bioaccumulation of mercury and methylmercury,” *Water. Air. Soil Pollut.*, vol. 80, no. 1–4, pp. 915–921, Feb. 1995.

[61] R. M. Swiderski, *Quicksilver a Hisotry of the Use, Lore and Effects of Mercury*. Jefferson North Carolina: McFarland and Company, 2008.

[62] W. Thomas, “Through the Looking Glass: A Reflection on Current Mercury Regulation,” *Columbia J. Environ. Law*, vol. 29, p. 145, 2004.

[63] “Laws and Regulations | Mercury | US EPA.” [Online]. Available: http://www.epa.gov/hg/regs.htm. [Accessed: 19-Nov-2011].

[64] “UN treaty to limit mercury emissions signed by 140 countries - World - CBC News.” [Online]. Available: http://www.cbc.ca/news/world/story/2013/01/19/mercury-levels-un.html. [Accessed: 02-Feb-2013].

[65] Edison Electric Insitute, “Mercury Regulations.” 2013.

[66] O. US EPA, “Mercury and Air Toxics Standards (MATS) for Power Plants.” [Online]. Available: http://www.epa.gov/airquality/powerplanttoxics/powerplants.html. [Accessed: 25-Nov-2012].

[67] “Fish Consumption Advisories | Mercury | US EPA.” [Online]. Available: http://www.epa.gov/hg/advisories.htm. [Accessed: 18-Jan-2013].

[68] N. B. French, S. J. Priebe, W. J. Haas, and Jr., “Product Reviews: State-of-the-Art Mercury CEMs,” *Anal. Chem.*, vol. 71, no. 13, p. 470A–475A, Jul. 1999.

[69] N. Bloom and W. F. Fitzgerald, “Determination of volatile mercury species at the picogram level by low-temperature gas chromatography with cold-vapour atomic fluorescence detection,” *Anal. Chim. Acta*, vol. 208, pp. 151–161, 1988.

[70] S. K. Pandey and K.-H. Kim, “Experimental bias involved in the collection of gaseous elemental mercury by the gold amalgam method,” *Environ. Eng. Sci.*, vol. 25, no. 2, pp. 255–263, Mar. 2008.

[71] N. S. Bloom and E. A. Crecelius, “Determination of mercury in seawater at sub-nanogram per liter levels,” *Mar. Chem.*, vol. 14, no. 1, pp. 49–59, Nov. 1983.

[72] N. Ferrua, S. Cerutti, J. A. Salonia, R. A. Olsina, and L. D. Martinez, “On-line preconcentration and determination of mercury in biological and environmental samples by cold vapor-atomic absorption spectrometry,” *J. Hazard. Mater.*, vol. 141, no. 3, pp. 693–699, 2007.

[73] O. US EPA, “Method 1631: Measurement of Mercury in Water.” [Online]. Available: http://water.epa.gov/scitech/methods/cwa/metals/mercury/index.cfm. [Accessed: 30-Jan-2013].

[74] J. Mcnerney, R. Hanson, and P. Buseck, “Mercury Detection by Means of Thin Gold Films,” *Science*, vol. 178, no. 4061, p. 611–&, 1972.

[75] J. Drelich, C. L. White, and Z. Xu, “Laboratory Tests on Mercury Emission Monitoring with Resonating Gold-coated Silicon Cantilevers,” *Environ. Sci. Technol.*, vol. 42, no. 6, pp. 2072–2078, Mar. 2008.

[76] T. Thundat, E. A. Wachter, S. L. Sharp, and R. J. Warmack, “Detection of mercury vapor using resonating microcantilevers,” *Appl. Phys. Lett.*, vol. 66, no. 13, p. 1695, 1995.
[77] J. J. Caron, R. B. Haskell, P. Benoit, and J. F. Vetelino, “A surface acoustic wave mercury vapor sensor,” *Ieee Trans. Ultrason. Ferroelectr. Freq. Control*, vol. 45, no. 5, pp. 1393–1398, Sep. 1998.
[78] E. M. Nolan and S. J. Lippard, “A ‘Turn-On’ fluorescent sensor for the selective detection of mercuric ion in aqueous media,” *J. Am. Chem. Soc.*, vol. 125, no. 47, pp. 14270–14271, 2003.
[79] E. M. Nolan and S. J. Lippard, “Tools and tactics for the optical detection of mercuric ion,” *ChemInform*, vol. 39, no. 50, p. no–no, 2008.
[80] G. K. Darbha, A. Ray, and P. C. Ray, “Gold Nanoparticle-Based Miniaturized Nanomaterial Surface Energy Transfer Probe for Rapid and Ultrasensitive Detection of Mercury in Soil, Water, and Fish,” *Acs Nano*, vol. 1, no. 3, pp. 208–214, Oct. 2007.
[81] M. C. Daniel and D. Astruc, “Gold nanoparticles: assembly, supramolecular chemistry, quantum-size-related properties, and applications toward biology, catalysis, and nanotechnology,” *Chem. Rev.-Columb.*, vol. 104, no. 1, p. 293, 2004.
[82] A. Moores and F. Goettmann, “The plasmon band in noble metal nanoparticles: an introduction to theory and applications,” *New J Chem*, vol. 30, no. 8, pp. 1121–1132, 2006.
[83] D. J. Barber and I. C. Freestone, “An investigation of the origin of the colour of the Lycurgus Cup by analytical transmission electron microscopy,” *Archaeometry*, vol. 32, no. 1, pp. 33–45, 1990.
[84] G. L. Hornyak, C. J. Patrissi, E. B. Oberhauser, C. R. Martin, J.-C. Valmalette, L. Lemaire, J. Dutta, and H. Hofmann, “Effective medium theory characterization of Au/Ag nanoalloy-porous alumina composites,” *Nanostructured Mater.*, vol. 9, no. 1–8, pp. 571–574, 1997.
[85] M. Faraday, “The Bakerian Lecture: Experimental Relations of Gold (and Other Metals) to Light,” *Philos. Trans. R. Soc. Lond.*, vol. 147, pp. 145–181, Jan. 1857.
[86] C. F. Bohren and D. F. Huffman, *Absorption and Scattering of Light by Small Particles*. New York: Wiley, 1983.
[87] S. Eustis and M. A. El-Sayed, “Why gold nanoparticles are more precious than pretty gold: Noble metal surface plasmon resonance and its enhancement of the radiative and nonradiative properties of nanocrystals of different shapes,” *Chem. Soc. Rev.*, vol. 35, no. 3, pp. 209–217, 2006.
[88] L. M. Liz-Marzán, “Nanometals,” *reactions*, vol. 17, p. 18, 2004.
[89] G. Mie, “A contribution to the optics of turbid media, especially colloidal metallic suspensions,” in *Annales de Physique*, 1908, vol. 25, pp. 377–445.
[90] R. Gans, “Über die Form ultramikroskopischer Silberteilchen,” *Ann. Phys.*, vol. 352, no. 10, pp. 270–284, 1915.
[91] S. Link, M. B. Mohamed, and M. A. El-Sayed, “Simulation of the Optical Absorption Spectra of Gold Nanorods as a Function of Their Aspect Ratio and the Effect of the Medium Dielectric Constant,” *J. Phys. Chem. B*, vol. 103, no. 16, pp. 3073–3077, Apr. 1999.
[92] J. Turkevich, P. C. Stevenson, and J. Hillier, “A study of the nucleation and growth processes in the synthesis of colloidal gold,” *Discuss Faraday Soc*, vol. 11, pp. 55–75, 1951.
[93] G. Frens, “Controlled nucleation for the regulation of the particle size in monodisperse gold suspensions,” *Nature*, vol. 241, no. 105, pp. 20–22, 1973.
[94] N. R. Jana, L. Gearheart, and C. J. Murphy, “Wet chemical synthesis of high aspect ratio cylindrical gold nanorods,” *J. Phys. Chem. B*, vol. 105, no. 19, pp. 4065–4067, 2001.
[95] N. R. Jana, L. Gearheart, and C. J. Murphy, “Seed-mediated growth approach for shape-controlled synthesis of spheroidal and rod-like gold nanoparticles using a surfactant template,” *Adv. Mater.*, vol. 13, no. 18, pp. 1389–1393, 2001.

[96] C. J. Murphy and N. R. Jana, “Controlling the aspect ratio of inorganic nanorods and nanowires,” *Adv. Mater.*, vol. 14, no. 1, p. 80, 2002.
[97] R. Becker, B. Liedberg, and P. O. Käll, “CTAB promoted synthesis of Au nanorods–Temperature effects and stability considerations,” *J. Colloid Interface Sci.*, vol. 343, no. 1, pp. 25–30, 2010.
[98] J. Gao, C. M. Bender, and C. J. Murphy, “Dependence of the gold nanorod aspect ratio on the nature of the directing surfactant in aqueous solution,” *Langmuir*, vol. 19, no. 21, pp. 9065–9070, 2003.
[99] X. Kou, S. Zhang, Z. Yang, C. K. Tsung, G. D. Stucky, L. Sun, J. Wang, and C. Yan, “Glutathione-and cysteine-induced transverse overgrowth on gold nanorods,” *J. Am. Chem. Soc.*, vol. 129, no. 20, pp. 6402–6404, 2007.
[100] C. Wang, T. Wang, Z. Ma, and Z. Su, “pH-tuned synthesis of gold nanostructures from gold nanorods with different aspect ratios,” *Nanotechnology*, vol. 16, no. 11, p. 2555, 2005.
[101] H. J. Park, C. S. Ah, W. J. Kim, I. S. Choi, K. P. Lee, and W. S. Yun, “Temperature-induced control of aspect ratio of gold nanorods,” *J. Vac. Sci. Technol. Vac. Surfaces Films*, vol. 24, no. 4, pp. 1323–1326, 2006.
[102] B. Nikoobakht and M. A. El-Sayed, “Preparation and growth mechanism of gold nanorods (NRs) using seed-mediated growth method,” *Chem. Mater.*, vol. 15, no. 10, pp. 1957–1962, 2003.
[103] L. M. Liz-Marzán, M. Giersig, and P. Mulvaney, “Synthesis of nanosized gold-silica core-shell particles,” *Langmuir*, vol. 12, no. 18, pp. 4329–4335, 1996.
[104] L. M. Liz-Marzán, M. Giersig, and P. Mulvaney, “Homogeneous silica coating of vitreophobic colloids,” *Chem. Commun.*, no. 6, pp. 731–732, 1996.
[105] Y. Jin, X. Kang, Y. Song, B. Zhang, G. Cheng, and S. Dong, “Controlled nucleation and growth of surface-confined gold nanoparticles on a (3-aminopropyl) trimethoxysilane-modified glass slide: a strategy for SPR substrates,” *Anal. Chem.*, vol. 73, no. 13, pp. 2843–2849, 2001.
[106] F. Frederix, J. M. Friedt, K. H. Choi, W. Laureyn, A. Campitelli, D. Mondelaers, G. Maes, and G. Borghs, “Biosensing based on light absorption of nanoscaled gold and silver particles,” *Anal. Chem.*, vol. 75, no. 24, pp. 6894–6900, 2003.
[107] P. K. Jain, I. H. El-Sayed, and M. A. El-Sayed, “Au nanoparticles target cancer,” *Nano Today*, vol. 2, no. 1, pp. 18–29, 2007.
[108] I. H. El-Sayed, X. Huang, and M. A. El-Sayed, “Surface plasmon resonance scattering and absorption of anti-EGFR antibody conjugated gold nanoparticles in cancer diagnostics: applications in oral cancer,” *Nano Lett.*, vol. 5, no. 5, pp. 829–834, 2005.
[109] J. R. Lakowicz, C. D. Geddes, I. Gryczynski, J. Malicka, Z. Gryczynski, K. Aslan, J. Lukomska, E. Matveeva, J. Zhang, and R. Badugu, “Advances in surface-enhanced fluorescence,” *J. Fluoresc.*, vol. 14, no. 4, pp. 425–441, 2004.
[110] K. G. Thomas and P. V. Kamat, “Chromophore-functionalized gold nanoparticles,” *Accounts Chem. Res.*, vol. 36, no. 12, pp. 888–898, 2003.
[111] J. Zheng, C. Zhang, and R. M. Dickson, “Highly fluorescent, water-soluble, size-tunable gold quantum dots,” *Phys. Rev. Lett.*, vol. 93, no. 7, p. 77402, 2004.
[112] B. Liedberg, C. Nylander, and I. Lunström, “Surface plasmon resonance for gas detection and biosensing,” *Sensors Actuators*, vol. 4, pp. 299–304, 1983.
[113] B. Liedberg, C. Nylander, and I. Lundström, “Biosensing with surface plasmon resonance—how it all started,” *Biosens. Bioelectron.*, vol. 10, no. 8, pp. i–ix, 1995.
[114] C. Nylander, B. Liedberg, and T. Lind, “Gas detection by means of surface plasmon resonance,” *Sensors Actuators*, vol. 3, pp. 79–88, 1983.
[115] J. Homola, S. S. Yee, and G. Gauglitz, “Surface plasmon resonance sensors: review,” *Sensors Actuators B Chem.*, vol. 54, no. 1, pp. 3–15, 1999.

[116] D. A. Stuart, J. M. Yuen, N. Shah, O. Lyandres, C. R. Yonzon, M. R. Glucksberg, J. T. Walsh, and R. P. Van Duyne, “In vivo glucose measurement by surface-enhanced Raman spectroscopy,” *Anal. Chem.*, vol. 78, no. 20, pp. 7211–7215, 2006.
[117] E. Petryayeva and U. J. Krull, “Localized surface plasmon resonance: nanostructures, bioassays and biosensing--a review,” *Anal. Chim. Acta*, vol. 706, no. 1, pp. 8–24, Nov. 2011.
[118] G. H. Chan, J. Zhao, E. M. Hicks, G. C. Schatz, and R. P. Van Duyne, “Plasmonic properties of copper nanoparticles fabricated by nanosphere lithography,” *Nano Lett.*, vol. 7, no. 7, pp. 1947–1952, 2007.
[119] J. N. Anker, W. P. Hall, O. Lyandres, N. C. Shah, J. Zhao, and R. P. Van Duyne, “Biosensing with plasmonic nanosensors,” *Nat. Mater.*, vol. 7, no. 6, pp. 442–453, 2008.
[120] R. R. Ford and J. Pritchard, “Work functions of gold and silver films. Surface potentials of mercury and xenon,” *Trans. Faraday Soc.*, vol. 67, no. 0, pp. 216–221, Jan. 1971.
[121] R. W. Joyner and M. W. Roberts, “Auger electron spectroscopy studies of clean polycrystalline gold and of the adsorption of mercury on gold,” *J. Chem. Soc. Faraday Trans. 1 Phys. Chem. Condens. Phases*, vol. 69, pp. 1242–1250, 1973.
[122] F. Slemr, W. Seiler, C. Eberling, and P. Roggendorf, “The determination of total gaseous mercury in air at background levels,” *Anal. Chim. Acta*, vol. 110, no. 1, pp. 35–47, Oct. 1979.
[123] T. T. Mercer, “Adsorption of mercury vapor by gold and silver,” *Anal. Chem.*, vol. 51, no. 7, pp. 1026–1030, Jun. 1979.
[124] R. Dumarey, R. Dams, and J. Hoste, “Comparison of the collection and desorption efficiency of activated charcoal, silver, and gold for the determination of vapor-phase atmospheric mercury,” *Anal. Chem.*, vol. 57, no. 13, pp. 2638–2643, 1985.
[125] X. M. Yang, K. Tonami, L. A. Nagahara, K. Hashimoto, Y. Wei, and A. Fujishima, “In-situ observation of the electrochemical Hg/Au amalgam process on an Au electrode surface by atomic force microscopy,” *Surf. Sci.*, vol. 319, no. 1–2, pp. L17–L22, Nov. 1994.
[126] C. Battistoni, E. Bemporad, A. Galdikas, S. Kačiulis, G. Mattogno, S. Mickevičius, and V. Olevano, “Interaction of mercury vapour with thin films of gold,” *Appl. Surf. Sci.*, vol. 103, no. 2, pp. 107–111, Oct. 1996.
[127] R. Nowakowski, T. Kobiela, Z. Wolfram, and R. Duś, “Atomic force microscopy of AuHg alloy formation on thin Au films,” *Appl. Surf. Sci.*, vol. 115, no. 3, pp. 217–231, Jul. 1997.
[128] M. Levlin, E. Ikävalko, and T. Laitinen, “Adsorption of mercury on gold and silver surfaces,” *Fresenius J. Anal. Chem.*, vol. 365, no. 7, pp. 577–586, 1999.
[129] T. Kobiela, B. Nowakowski, and R. Duś, “The influence of gas phase composition on the process of Au–Hg amalgam formation,” *Appl. Surf. Sci.*, vol. 206, no. 1, pp. 78–89, 2003.
[130] J. S. Lee, M. S. Han, and C. A. Mirkin, “Colorimetric Detection of Mercuric Ion (Hg2+) in Aqueous Media using DNA-Functionalized Gold Nanoparticles,” *Angew. Chem.*, vol. 119, no. 22, pp. 4171–4174, 2007.
[131] J. Liu and Y. Lu, “Rational Design of ‘Turn-On’ Allosteric DNAzyme Catalytic Beacons for Aqueous Mercury Ions with Ultrahigh Sensitivity and Selectivity,” *Angew. Chem.*, vol. 119, no. 40, pp. 7731–7734, 2007.
[132] D. Li, A. Wieckowska, and I. Willner, “Optical Analysis of Hg2+ Ions by Oligonucleotide–Gold-Nanoparticle Hybrids and DNA-Based Machines,” *Angew. Chem.*, vol. 120, no. 21, pp. 3991–3995, 2008.
[133] L. Wang, J. Zhang, X. Wang, Q. Huang, D. Pan, S. Song, and C. Fan, “Gold nanoparticlebased optical probes for target-responsive DNA structures,” *Gold Bull.*, vol. 41, no. 1, pp. 37–41, 2008.

[134] T. Morris and G. Szulczewski, “Evaluating the role of coinage metal films in the detection of mercury vapor by surface plasmon resonance spectroscopy,” *Langmuir*, vol. 18, no. 15, pp. 5823–5829, 2002.
[135] T. Morris, H. Copeland, E. McLinden, S. Wilson, and G. Szulczewski, “The effects of mercury adsorption on the optical response of size-selected gold and silver nanoparticles,” *Langmuir*, vol. 18, no. 20, pp. 7261–7264, 2002.
[136] T. Morris, K. Kloepper, S. Wilson, and G. Szulczewski, “A spectroscopic study of mercury vapor adsorption on gold nanoparticle films,” *J. Colloid Interface Sci.*, vol. 254, no. 1, pp. 49–55, 2002.
[137] M. Rex, F. E. Hernandez, and A. D. Campiglia, “Pushing the Limits of Mercury Sensors with Gold Nanorods,” *Anal Chem*, vol. 78, no. 2, pp. 445–451, 2005.
[138] J. Z. James, D. Lucas, and C. P. Koshland, “Gold Nanoparticle Films As Sensitive and Reusable Elemental Mercury Sensors,” *Environ. Sci. Technol.*, vol. 46, no. 17, pp. 9557–9562, Sep. 2012.
[139] U. Ackelid and L. G. Petersson, “How a limited mass transfer in the gas phase may affect the steady-state response of a Pd-MOS hydrogen sensor,” *Sensors Actuators B Chem.*, vol. 3, no. 2, pp. 139–146, 1991.
[140] M. Johansson, L.-G. Ekedahl, and I. Lundström, “The influence of mass transport processes on the response to gas mixtures of field-effect devices with large-area catalytic metal gates,” *J. Appl. Phys.*, vol. 86, no. 1, pp. 657–663, Jul. 1999.
[141] A. M. Lezzi, G. P. Beretta, E. Comini, G. Faglia, G. Galli, and G. Sberveglieri, “Influence of gaseous species transport on the response of solid state gas sensors within enclosures,” *Sensors Actuators B Chem.*, vol. 78, no. 1–3, pp. 144–150, 2001.
[142] Y. Zhu, J. Shi, Z. Zhang, C. Zhang, and X. Zhang, “Development of a Gas Sensor Utilizing Chemiluminescence on Nanosized Titanium Dioxide,” *Anal. Chem.*, vol. 74, no. 1, pp. 120–124, Jan. 2002.
[143] P. E. Sheehan and L. J. Whitman, “Detection limits for nanoscale biosensors,” *Nano Lett.*, vol. 5, no. 4, pp. 803–807, 2005.
[144] D. R. Kim and X. Zheng, “Numerical characterization and optimization of the microfluidics for nanowire biosensors,” *Nano Lett.*, vol. 8, no. 10, pp. 3233–3237, 2008.
[145] N. S. Lynn, H. Šípová, P. Adam, and J. Homola, “Enhancement of affinity-based biosensors: effect of sensing chamber geometry on sensitivity,” *Lab. Chip*, vol. 13, no. 7, p. 1413, 2013.
[146] T. M. Squires, R. J. Messinger, and S. R. Manalis, “Making it stick: convection, reaction and diffusion in surface-based biosensors,” *Nat. Biotechnol.*, vol. 26, no. 4, pp. 417–426, 2008.
[147] F. P. Incropera and D. P. DeWitt, *Fundamentals of Heat and Mass Transfer*, 5th ed. John Wiley & Sons, 2002.
[148] W. Kays, M. Crawford, and B. Weigand, *Convective Heat and Mass Transfer*, 4th ed. Boston: McGraw Hill, 2005.
[149] W. Mangler, “NATIONAL ADVISORY COMMITTEE FOR AERONAUTICS I.”
[150] H. Martin, “Heat and Mass Transfer between Impinging Gas Jets and Solid Surfaces,” in in *Advances in Heat Transfer*, vol. Volume 13, James P. Hartnett and Thomas F. Irvine, Ed. Elsevier, 1977, pp. 1–60.
[151] A. Dabrowski, “Adsorption–from theory to practice.,” *Adv. Colloid Interface Sci.*, vol. 93, no. 1–3, p. 135, 2001.
[152] I. Langmuir, “THE CONSTITUTION AND FUNDAMENTAL PROPERTIES OF SOLIDS AND LIQUIDS. PART I. SOLIDS.,” *J. Am. Chem. Soc.*, vol. 38, no. 11, pp. 2221–2295, Nov. 1916.
[153] Y. S. Ho, J. C. Y. Ng, and G. McKay, “Kinetics of pollutant sorption by biosorbents: review,” *Sep. Purif. Rev.*, vol. 29, no. 2, pp. 189–232, 2000.

[154] R. Aveyard and D. A. Haydon, *An Introduction to the Principles of Surface Chemistry*. Cambridge: Cambridge University Press, 1973.
[155] D. S. Karpovich and G. J. Blanchard, "Direct Measurement of the Adsorption Kinetics of Alkanethiolate Self-Assembled Monolayers on a Microcrystalline Gold Surface," *Langmuir*, vol. 10, no. 9, pp. 3315–3322, 1994.
[156] C. Nguyen and D. . Do, "The Dubinin–Radushkevich equation and the underlying microscopic adsorption description," *Carbon*, vol. 39, no. 9, pp. 1327–1336, Aug. 2001.
[157] S. Chowdhury, R. Mishra, P. Saha, and P. Kushwaha, "Adsorption thermodynamics, kinetics and isosteric heat of adsorption of malachite green onto chemically modified rice husk," *Desalination*, vol. 265, no. 1, pp. 159–168, 2011.
[158] S. Lagergren, "About the theory of so-called adsorption of soluble substances," *K. Sven. Vetenskapsakademiens Handl.*, vol. 24, no. 4, pp. 1–39, 1898.
[159] H. Yuh-Shan, "Citation review of Lagergren kinetic rate equation on adsorption reactions," *Scientometrics*, vol. 59, no. 1, pp. 171–177, 2004.
[160] S. Azizian, "Kinetic models of sorption: a theoretical analysis," *J. Colloid Interface Sci.*, vol. 276, no. 1, pp. 47–52, Aug. 2004.
[161] A. W. Marczewski, "Analysis of kinetic Langmuir model. Part I: Integrated kinetic Langmuir equation (IKL): a new complete analytical solution of the Langmuir rate equation," *Langmuir*, vol. 26, no. 19, pp. 15229–15238, 2010.
[162] Y. S. Ho and G. McKay, "Pseudo-second order model for sorption processes," *Process Biochem.*, vol. 34, no. 5, pp. 451–465, 1999.
[163] Y. S. Ho and G. McKay, "The kinetics of sorption of divalent metal ions onto sphagnum moss peat," *Water Res.*, vol. 34, no. 3, pp. 735–742, 2000.
[164] Y. S. Ho, D. A. J. Wase, and C. F. Forster, "Kinetic studies of competitive heavy metal adsorption by sphagnum moss peat," *Environ. Technol.*, vol. 17, no. 1, pp. 71–77, 1996.
[165] D. C. Sharma and C. F. Forster, "A preliminary examination into the adsorption of hexavalent chromium using low-cost adsorbents," *Bioresour. Technol.*, vol. 47, no. 3, pp. 257–264, 1994.
[166] D. C. Sharma and C. F. Forster, "Removal of hexavalent chromium using sphagnum moss peat," *Water Res.*, vol. 27, no. 7, pp. 1201–1208, 1993.
[167] S. . Elovich and G. . Zhabrova, *Zhurnal Fiz. Khimii*, vol. 13, p. 325, 1936.
[168] D. L. Sparks, *Environmental soil chemistry*. Academic Press, 2003.
[169] M. J. D. Low, "Kinetics of Chemisorption of Gases on Solids.," *Chem. Rev.*, vol. 60, no. 3, pp. 267–312, 1960.
[170] M. Mohapatra, S. Khatun, and S. Anand, "Kinetics and thermodynamics of lead (II) adsorption on lateritic nickel ores of Indian origin," *Chem. Eng. J.*, vol. 155, no. 1, pp. 184–190, 2009.
[171] S. S. Gupta and K. G. Bhattacharyya, "Adsorption of Ni (II) on clays," *J. Colloid Interface Sci.*, vol. 295, no. 1, pp. 21–32, 2006.
[172] J. Gao, Q. Zhang, K. Su, R. Chen, and Y. Peng, "Biosorption of Acid Yellow 17 from aqueous solution by non-living aerobic granular sludge," *J. Hazard. Mater.*, vol. 174, no. 1, pp. 215–225, 2010.
[173] T. S. Anirudhan and P. G. Radhakrishnan, "Thermodynamics and kinetics of adsorption of Cu (II) from aqueous solutions onto a new cation exchanger derived from tamarind fruit shell," *J. Chem. Thermodyn.*, vol. 40, no. 4, pp. 702–709, 2008.
[174] Y. S. Ho and G. McKay, "Sorption of dye from aqueous solution by peat," *Chem. Eng. J.*, vol. 70, no. 2, pp. 115–124, 1998.
[175] C. W. Cheung, J. F. Porter, and G. McKay, "Sorption kinetic analysis for the removal of cadmium ions from effluents using bone char," *Water Res.*, vol. 35, no. 3, pp. 605–612, 2001.

[176] G. E. Boyd, A. W. Adamson, and L. S. Myers Jr, “The Exchange Adsorption of Ions from Aqueous Solutions by Organic Zeolites. II. Kinetics1,” *J. Am. Chem. Soc.*, vol. 69, no. 11, pp. 2836–2848, 1947.
[177] W. J. Weber and J. C. Morris, “Kinetics of adsorption on carbon from solution,” *J Sanit Eng Div Am Soc Civ Eng*, vol. 89, no. 17, pp. 31–60, 1963.
[178] V. J. P. Poots, G. McKay, and J. J. Healy, “The removal of acid dye from effluent using natural adsorbents—I peat,” *Water Res.*, vol. 10, no. 12, pp. 1061–1066, 1976.
[179] T. Morris, J. Sun, and G. Szulczewski, “Measurement of the chemical and morphological changes that occur on gold surfaces following thermal desorption and acid dissolution of adsorbed mercury,” *Anal. Chim. Acta*, vol. 496, no. 1–2, pp. 279–287, Oct. 2003.
[180] Y. M. Sabri, S. J. Ippolito, J. Tardio, and S. K. Bhargava, “Study of Surface Morphology Effects on Hg Sorption–Desorption Kinetics on Gold Thin-Films,” *J. Phys. Chem. C*, vol. 116, no. 3, pp. 2483–2492, 2012.
[181] P. Kisliuk, “The sticking probabilities of gases chemisorbed on the surfaces of solids,” *J. Phys. Chem. Solids*, vol. 3, no. 1, pp. 95–101, 1957.
[182] D. Eck, C. A. Helm, N. J. Wagner, and K. A. Vaynberg, “Plasmon Resonance Measurements of the Adsorption and Adsorption Kinetics of a Biopolymer onto Gold Nanocolloids,” *Langmuir*, vol. 17, no. 4, pp. 957–960, 2001.
[183] I. U. Vakarelski, R. Maenosono, J. W. Kwek, and K. Higashitani, “Thermal modification of layer-by-layer assembled gold nanoparticle films,” *Colloids Surfaces Physicochem. Eng. Asp.*, vol. 340, no. 1–3, pp. 193–198, May 2009.
[184] Cole-Parmer, “Rotameters: Variable Area Flowmeters Tech Info.” 2012.
[185] M. Levlin, H. E. M. Niemi, P. Hautojärvi, E. Ikävalko, and T. Laitinen, “Mercury adsorption on gold surfaces employed in the sampling and determination of vaporous mercury: a scanning tunneling microscopy study,” *Fresenius J. Anal. Chem.*, vol. 355, no. 1, pp. 2–9, 1996.
[186] A. Kwan, J. Dudley, and E. Lantz, “Who really discovered Snell’s law?,” *Phys. World*, vol. 15, no. 4, p. 64, 2002.
[187] R. J. Bates, *Optical Switching and Networking Handbook*. New York: McGraw-Hill.
[188] J. Hecht, *City of light: the story of fiber optics*. Oxford University Press on Demand, 2004.
[189] K. T. V. Grattan and T. Sun, “Fiber optic sensor technology: an overview,” *Sensors Actuators Phys.*, vol. 82, no. 1–3, pp. 40–61, May 2000.
[190] A. D. Kersey, “A Review of Recent Developments in Fiber Optic Sensor Technology,” *Opt. Fiber Technol.*, vol. 2, no. 3, pp. 291–317, Jul. 1996.
[191] F. Villuendas and J. Pelayo, “Optical fibre device for chemical seming based on surface plasmon excitridon,” *Sensors Actuators Phys.*, vol. 23, no. 1, pp. 1142–1145, 1990.
[192] L. De Maria, M. Martinelli, and G. Vegetti, “Fiber-optic sensor based on surface plasmon interrogation,” *Sensors Actuators B Chem.*, vol. 12, no. 3, pp. 221–223, 1993.
[193] R. C. Jorgenson and S. S. Yee, “A fiber-optic chemical sensor based on surface plasmon resonance,” *Sensors Actuators B Chem.*, vol. 12, no. 3, pp. 213–220, 1993.
[194] R. Alonso, F. Villuendas, J. Tornos, and J. Pelayo, “New ‘in-line’ optical-fibre sensor based on surface plasmon excitation,” *Sensors Actuators Phys.*, vol. 37–38, pp. 187–192, Jun. 1993.
[195] K. Kurihara, H. Ohkawa, Y. Iwasaki, O. Niwa, T. Tobita, and K. Suzuki, “Fiber-optic conical microsensors for surface plasmon resonance using chemically etched single-mode fiber,” *Anal. Chim. Acta*, vol. 523, no. 2, pp. 165–170, Oct. 2004.
[196] Ó. Esteban, M. Cruz-Navarrete, A. González-Cano, and E. Bernabeu, “Measurement of the Degree of Salinity of Water with a Fiber-Optic Sensor,” *Appl. Opt.*, vol. 38, no. 25, pp. 5267–5271, Sep. 1999.

[197] S. Chand and B. D. Gupta, “Surface plasmon resonance based fiber-optic sensor for the detection of pesticide,” *Sensors Actuators B Chem.*, vol. 123, no. 2, pp. 661–666, 2007.
[198] A. Abdelghani, J. M. Chovelon, N. Jaffrezic-Renault, C. Ronot-Trioli, C. Veillas, and H. Gagnaire, “Surface plasmon resonance fibre-optic sensor for gas detection,” *Sensors Actuators B Chem.*, vol. 39, no. 1, pp. 407–410, 1997.
[199] R. Ince and R. Narayanaswamy, “Analysis of the performance of interferometry, surface plasmon resonance and luminescence as biosensors and chemosensors,” *Anal. Chim. Acta*, vol. 569, no. 1–2, pp. 1–20, May 2006.
[200] R. Slavík, J. Homola, J. \vCtyrokỳ, and E. Brynda, “Novel spectral fiber optic sensor based on surface plasmon resonance,” *Sensors Actuators B Chem.*, vol. 74, no. 1, pp. 106–111, 2001.
[201] R. Slavık, J. Homola, and E. Brynda, “A miniature fiber optic surface plasmon resonance sensor for fast detection of staphylococcal enterotoxin B,” *Biosens. Bioelectron.*, vol. 17, no. 6, pp. 591–595, 2002.
[202] J.-F. Masson, L. Obando, S. Beaudoin, and K. Booksh, “Sensitive and real-time fiber-optic-based surface plasmon resonance sensors for myoglobin and cardiac troponin I,” *Talanta*, vol. 62, no. 5, pp. 865–870, Apr. 2004.
[203] A. Leung, P. M. Shankar, and R. Mutharasan, “A review of fiber-optic biosensors,” *Sensors Actuators B Chem.*, vol. 125, no. 2, pp. 688–703, 2007.
[204] I. Stemmler, A. Brecht, and G. Gauglitz, “Compact surface plasmon resonance-transducers with spectral readout for biosensing applications,” *Sensors Actuators B Chem.*, vol. 54, no. 1–2, pp. 98–105, Jan. 1999.
[205] S.-F. Cheng and L.-K. Chau, “Colloidal Gold-Modified Optical Fiber for Chemical and Biochemical Sensing,” *Anal. Chem.*, vol. 75, no. 1, pp. 16–21, Jan. 2003.
[206] C. H. Chen, T. C. Tsao, W. Y. Li, W. C. Shen, C. W. Cheng, J. L. Tang, C. P. Jen, L. K. Chau, and W. T. Wu, “Novel U-shape gold nanoparticles-modified optical fiber for localized plasmon resonance chemical sensing,” *Microsyst. Technol.*, vol. 16, no. 7, pp. 1207–1214, 2010.
[207] T.-J. Lin, K.-T. Huang, and C.-Y. Liu, “Determination of organophosphorous pesticides by a novel biosensor based on localized surface plasmon resonance,” *Biosens. Bioelectron.*, vol. 22, no. 4, pp. 513–518, Oct. 2006.
[208] A. K. Sharma and B. D. Gupta, “Fiber optic sensor based on surface plasmon resonance with nanoparticle films,” *Photonics Nanostructures - Fundam. Appl.*, vol. 3, no. 1, pp. 30–37, Aug. 2005.
[209] C.-S. Cheng, Y.-Q. Chen, and C.-J. Lu, “Organic vapour sensing using localized surface plasmon resonance spectrum of metallic nanoparticles self assemble monolayer,” *Talanta*, vol. 73, no. 2, pp. 358–365, Sep. 2007.
[210] M. D. Malinsky, K. L. Kelly, G. C. Schatz, and R. P. Van Duyne, “Chain Length Dependence and Sensing Capabilities of the Localized Surface Plasmon Resonance of Silver Nanoparticles Chemically Modified with Alkanethiol Self-Assembled Monolayers,” *J. Am. Chem. Soc.*, vol. 123, no. 7, pp. 1471–1482, Feb. 2001.
[211] A. K. Sharma and B. D. Gupta, “Comparison of performance parameters of conventional and nano-plasmonic fiber optic sensors,” *Plasmonics*, vol. 2, no. 2, pp. 51–54, 2007.
[212] F. Kim, S. Kwan, J. Akana, and P. Yang, “Langmuir-Blodgett nanorod assembly,” *J. Am. Chem. Soc.*, vol. 123, no. 18, pp. 4360–4361, 2001.
[213] P. Wang, L. Zhang, Y. Xia, L. Tong, X. Xu, and Y. Ying, “Polymer nanofibers embedded with aligned gold nanorods: a new platform for plasmonic studies and optical sensing,” *Nano Lett.*, vol. 12, no. 6, pp. 3145–3150, 2012.

[214] D. J. Sirbuly, A. Tao, M. Law, R. Fan, and P. Yang, “Multifunctional nanowire evanescent wave optical sensors,” *Adv. Mater.*, vol. 19, no. 1, pp. 61–66, 2007.
[215] G. Chen, *Nanoscale Energy Transport and Conversion*. Oxford University Press, 2005.
[216] D. Littlejohn, D. Lucas, and L. Han, “Bent silica fiber evanescent absorption sensors for near-infrared spectroscopy,” *Appl. Spectrosc.*, vol. 53, no. 7, pp. 845–849, 1999.
[217] B. D. Gupta, H. Dodeja, and A. K. Tomar, “Fibre-optic evanescent field absorption sensor based on a U-shaped probe,” *Opt. Quantum Electron.*, vol. 28, no. 11, pp. 1629–1639, 1996.
[218] A. W. Snyder and J. D. Love, *Optial Waveguide Theory*. Chapman and Hall, 1983.
[219] G. Ghosh, M. Endo, and T. Iwasaki, “Temperature-dependent Sellmeier coefficients and chromatic dispersions for some optical fiber glasses,” *Light. Technol. J.*, vol. 12, no. 8, pp. 1338–1342, 1994.
[220] D. Monzón-Hernández, J. Villatoro, D. Talavera, and D. Luna-Moreno, “Optical-fiber surface-plasmon resonance sensor with multiple resonance peaks,” *Appl. Opt.*, vol. 43, no. 6, pp. 1216–1220, 2004.
[221] Y.-C. Kim, W. Peng, S. Banerji, and K. S. Booksh, “Tapered fiber optic surface plasmon resonance sensor for analyses of vapor and liquid phases,” *Opt. Lett.*, vol. 30, no. 17, pp. 2218–2220, 2005.
[222] S. Link and M. A. El-Sayed, “Size and temperature dependence of the plasmon absorption of colloidal gold nanoparticles,” *J. Phys. Chem. B*, vol. 103, no. 21, pp. 4212–4217, 1999.
[223] S. Link and M. A. El-Sayed, “Spectral properties and relaxation dynamics of surface plasmon electronic oscillations in gold and silver nanodots and nanorods,” *J. Phys. Chem. B*, vol. 103, no. 40, pp. 8410–8426, 1999.
[224] P. B. Johnson and R. W. Christy, “Optical Constants of the Noble Metals,” *Phys. Rev. B*, vol. 6, no. 12, pp. 4370–4379, Dec. 1972.
[225] P. Mulvaney, “Surface Plasmon Spectroscopy of Nanosized Metal Particles,” *Langmuir*, vol. 12, no. 3, pp. 788–800, 1996.
[226] S. K. Srivastava and B. D. Gupta, “Simulation of a localized surface-plasmon-resonance-based fiber optic temperature sensor,” *J. Opt. Soc. Am. -Opt. Image Sci. Vis.*, vol. 27, no. 7, pp. 1743–1749, Jul. 2010.
[227] W. Chemnasiry and F. E. Hernandez, “Gold nanorod-based mercury sensor using functionalized glass substrates,” *Sensors Actuators B Chem.*, vol. 173, pp. 322–328, 2012.
[228] E. C. Heider, K. Trieu, A. F. T. Moore, and A. D. Campiglia, “Portable mercury sensor for tap water using surface plasmon resonance of immobilized gold nanorods,” *Talanta*, vol. 99, pp. 180–185, 2012.
[229] K. M. Mayer and J. H. Hafner, “Localized Surface Plasmon Resonance Sensors,” *Chem. Rev.*, vol. 111, no. 6, pp. 3828–3857, Jun. 2011.
[230] D. R. Lide, *CRC handbook of chemistry and physics*. CRC press, 2012.
[231] F. J. García de Abajo, “Nonlocal effects in the plasmons of strongly interacting nanoparticles, dimers, and waveguides,” *J. Phys. Chem. C*, vol. 112, no. 46, pp. 17983–17987, 2008.
[232] I. Romero, J. Aizpurua, G. W. Bryant, and F. J. de Abajo, “Plasmons in nearly touching metallic nanoparticles: singular response in the limit of touching dimers,” *Arxiv Prepr. Arxiv07080876*, 2007.
[233] P. K. Jain, W. Huang, and M. A. El-Sayed, “On the Universal Scaling Behavior of the Distance Decay of Plasmon Coupling in Metal Nanoparticle Pairs: A Plasmon Ruler Equation,” *Nano Lett.*, vol. 7, no. 7, pp. 2080–2088, Jul. 2007.
[234] K. Scallan, D. Lucas, and C. Koshland, “A Novel UV-Vis Spectroscopic Method to Detect Elemental Mercury Using Gold Nanoparticles,” *Epidemiology*, vol. 17, no. 6, p. S493, 2006.

[235] T. Morris, H. Copeland, E. McLinden, S. Wilson, and G. Szulczewski, “The Effects of Mercury Adsorption on the Optical Response of Size-Selected Gold and Silver Nanoparticles,” *Langmuir*, vol. 18, no. 20, pp. 7261–7264, 2002.
[236] T. Morris and G. Szulczewski, “Evaluating the Role of Coinage Metal Films in the Detection of Mercury Vapor by Surface Plasmon Resonance Spectroscopy,” *Langmuir*, vol. 18, no. 15, pp. 5823–5829, 2002.
[237] I. E. Sendroiu, S. F. L. Mertens, and D. J. Schiffrin, “Plasmon interactions between gold nanoparticles in aqueous solution with controlled spatial separation,” *Phys Chem Chem Phys*, vol. 8, no. 12, pp. 1430–1436, 2006.
[238] P. E. Ciddor, “Refractive index of air: new equations for the visible and near infrared,” *Appl. Opt.*, vol. 35, no. 9, pp. 1566–1573, 1996.
[239] G. Ghosh, M. Endo, and T. Iwasaki, “Temperature-dependent Sellmeier coefficients and chromatic dispersions for some optical fiber glasses,” *Light. Technol. J.*, vol. 12, no. 8, pp. 1338–1342, 1994.
[240] C. Y. Chen, C. T. Driscoll, K. F. Lambert, R. P. Mason, L. R. Rardin, N. Serrell, and E. M. Sunderland, “Marine mercury fate: From sources to seafood consumers,” *Environ. Res.*, vol. 119, pp. 1–2, Nov. 2012.
[241] K. F. Lambert, D. C. Evers, K. A. Warner, S. L. King, and N. E. Selin, “Integrating mercury science and policy in the marine context: Challenges and opportunities,” *Environ. Res.*, vol. 119, pp. 132–142, Nov. 2012.
[242] J. A. Davis, R. E. Looker, D. Yee, M. Marvin-Di Pasquale, J. L. Grenier, C. M. Austin, L. J. McKee, B. K. Greenfield, R. Brodberg, and J. D. Blum, “Reducing methylmercury accumulation in the food webs of San Francisco Bay and its local watersheds,” *Environ. Res.*, vol. 119, pp. 3–26, Nov. 2012.
[243] R. P. Mason, A. L. Choi, W. F. Fitzgerald, C. R. Hammerschmidt, C. H. Lamborg, A. L. Soerensen, and E. M. Sunderland, “Mercury biogeochemical cycling in the ocean and policy implications,” *Environ. Res.*, vol. 119, pp. 101–117, Nov. 2012.
[244] J. L. Kirk, I. Lehnherr, M. Andersson, B. M. Braune, L. Chan, A. P. Dastoor, D. Durnford, A. L. Gleason, L. L. Loseto, A. Steffen, and V. L. St. Louis, “Mercury in Arctic marine ecosystems: Sources, pathways and exposure,” *Environ. Res.*, vol. 119, pp. 64–87, Nov. 2012.
[245] E. M. Sunderland, “Mercury exposure from domestic and imported estuarine and marine fish in the US seafood market,” *Environ. Health Perspect.*, vol. 115, no. 2, p. 235, 2007.
[246] I. Sahuquillo, M. J. Lagarda, M. D. Silvestre, and R. Farré, “Methylmercury determination in fish and seafood products and estimated daily intake for the Spanish population,” *Food Addit. Contam.*, vol. 24, no. 8, pp. 869–876, 2007.
[247] P. Johansen, D. Muir, G. Asmund, and F. Riget, “Human exposure to contaminants in the traditional Greenland diet,” *Sci. Total Environ.*, vol. 331, no. 1–3, pp. 189–206, Sep. 2004.
[248] L. Jaeglé, S. A. Strode, N. E. Selin, and D. J. Jacob, “The Geos-Chem model,” in in *Mercury Fate and Transport in the Global Atmosphere*, R. Mason and N. Pirrone, Eds. Springer US, 2009, pp. 533–545.
[249] E. Oken, A. L. Choi, M. R. Karagas, K. Mariën, C. M. Rheinberger, R. Schoeny, E. Sunderland, and S. Korrick, “Which Fish Should I Eat? Perspectives Influencing Fish Consumption Choices,” *Environ. Health Perspect.*, vol. 120, no. 6, pp. 790–798, Jun. 2012.
[250] C. Chen, “Methylmercury Effects and Exposures: Who Is at Risk?,” *Environ. Health Perspect.*, vol. 120, no. 6, pp. a224–a225, Jun. 2012.
[251] G. J. Keeler, N. Pirrone, R. Bullock, and S. Sillman, “The need for a coordinated global Hg monitoring network for global and regional models validation,” in in *Mercury Fate and Transport in the Global Atmosphere*, R. Mason and N. Pirrone, Eds. Springer US, 2009, pp. 391–424.

[252] “Global Mercury Observation System.” Insstitue of Atmospheric Pollution Research.
[253] Arizona Instruments, “Jerome 431-X Mercury Vapor Analyzer Operation Manual.” Arizona Instruments LLC, Sep-2000.
[254] W. A. Telliard and M. Andersson, “Method 245.7 Mercury in Water by Cold Vapor Atomic Fluorescence Spectrometry.” US EPA Office of Science and Technology, Feb-2005.
[255] “Appendix to Method 1631 Total Mercury in Tissue, Sludge, Sediment, and Soil by Acid Digestion and BrCl Oxidation.” US EPA Office of Science and Technology.
[256] Y. A. Vil’pan, I. L. Grinshtein, A. A. Akatov, and S. Gucer, “Direct atomic absorption determination of mercury in drinking water and urine using a two-step electrothermal atomizer,” *J. Anal. Chem.*, vol. 60, no. 1, pp. 38–44, 2005.
[257] I. L. Grinshtein, Y. A. Vilpan, A. V. Saraev, and L. A. Vasilieva, “Direct atomic absorption determination of cadmium and lead in strongly interfering matrices by double vaporization with a two-step electrothermal atomizer,” *Spectrochim. Acta Part B-At. Spectrosc.*, vol. 56, no. 3, pp. 261–274, Mar. 2001.
[258] M. E. Andersson, K. G\aardfeldt, and I. Wängberg, “A description of an automatic continuous equilibrium system for the measurement of dissolved gaseous mercury,” *Anal. Bioanal. Chem.*, vol. 391, no. 6, pp. 2277–2282, 2008.
[259] M. E. Andersson, J. Sommar, K. Gårdfeldt, and S. Jutterström, “Air–sea exchange of volatile mercury in the North Atlantic Ocean,” *Mar. Chem.*, vol. 125, no. 1–4, pp. 1–7, Jul. 2011.
[260] H. L. Clever, S. A. Johnson, and M. E. Derrick, “The Solubility of Mercury and Some Sparingly Soluble Mercury Salts in Water and Aqueous Electrolyte Solutions,” *J. Phys. Chem. Ref. Data*, vol. 14, no. 3, pp. 631–680, Jul. 1985.
[261] G. A. Lugg, “Diffusion coefficients of some organic and other vapors in air,” *Anal. Chem.*, vol. 40, no. 7, pp. 1072–1077, 1968.
[262] K. Leopold, L. Harwardt, M. Schuster, and G. Schlemmer, “A new fully automated on-line digestion system for ultra trace analysis of mercury in natural waters by means of FI-CV-AFS,” *Talanta*, vol. 76, no. 2, pp. 382–388, Jul. 2008.
[263] L. Sun, S. Lin, L. Feng, and D. Yuan, “An automatic Flow System of Rapid on-Line Digestion and Pre-Concentration for In-Field Determination of Trace Total Mercury in Seawater,” *Anal. Lett.*, vol. 45, no. 10, pp. 1321–1331, 2012.
[264] R. S. Yolles, B. J. Wood, and H. Wise, “Hydrogenation of alkenes on gold,” *J. Catal.*, vol. 21, no. 1, pp. 66–69, 1971.
[265] A. Sanchez, S. Abbet, U. Heiz, W.-D. Schneider, H. Häkkinen, R. N. Barnett, and U. Landman, “When gold is not noble: Nanoscale gold catalysts,” *J. Phys. Chem. A*, vol. 103, no. 48, pp. 9573–9578, 1999.
[266] T. Hayashi, K. Tanaka, and M. Haruta, “Selective Vapor-Phase Epoxidation of Propylene over Au/TiO< sub> 2</sub> Catalysts in the Presence of Oxygen and Hydrogen,” *J. Catal.*, vol. 178, no. 2, pp. 566–575, 1998.
[267] M. D. Hughes, Y.-J. Xu, P. Jenkins, P. McMorn, P. Landon, D. I. Enache, A. F. Carley, G. A. Attard, G. J. Hutchings, F. King, E. H. Stitt, P. Johnston, K. Griffin, and C. J. Kiely, “Tunable gold catalysts for selective hydrocarbon oxidation under mild conditions,” *Nature*, vol. 437, no. 7062, pp. 1132–1135, Oct. 2005.
[268] D. B. Aeschliman and G. A. Norton, “Collection and thermal evolution behaviors of different mercury species captured with gold,” *Environ. Sci. Technol.*, vol. 33, no. 13, pp. 2278–2283, 1999.
[269] A. Zierhut, K. Leopold, L. Harwardt, P. Worsfold, and M. Schuster, “Activated gold surfaces for the direct preconcentration of mercury species from natural waters,” *J. Anal. At. Spectrom.*, vol. 24, no. 6, pp. 767–774, 2009.

[270] A. Zierhut, K. Leopold, L. Harwardt, and M. Schuster, “Analysis of total dissolved mercury in waters after on-line preconcentration on an active gold column,” *Talanta*, vol. 81, no. 4–5, pp. 1529–1535, Jun. 2010.
[271] R. Knight, S. J. Haswell, S. W. Lindow, and J. Batty, “Determination of mercury in hair by coupled CVAA-ICP-MS,” *J Anal Spectrom*, vol. 14, no. 2, pp. 127–129, 1999.
[272] G. Leng, L. Feng, S.-B. Li, S. Qian, and D.-Z. Dan, “Determination of Mercury (Hg) in Sediment by a Sequential Injection (SI) System With Cold Vapor Generation Atomic Fluorescence Spectrometry (CVAFS) Detection After a Rapid and Mild Microwave-Assisted Digestion,” *Environ. Forensics*, vol. 14, no. 1, pp. 9–15, 2013.
[273] D. A. Duford, J. P. Lafleur, R. Lam, C. D. Skinner, and E. D. Salin, “Induction heating-electrothermal vaporization for direct mercury determination in a single human hair by atomic fluorescence and atomic absorption spectrometry,” *J. Anal. At. Spectrom.*, vol. 22, no. 3, pp. 326–329, 2007.
[274] “ATSDR – Priority List of Hazardous Substances.” [Online]. Available: http://www.atsdr.cdc.gov/SPL/index.html. [Accessed: 24-Apr-2013].
[275] A. J. Hynes, D. L. Donohoue, M. E. Goodsite, and I. M. Hedgecock, “Our current understanding of major chemical and physical processes affecting mercury dynamics in the atmosphere and at the air-water/terrestrial interfaces,” in in *Mercury Fate and Transport in the Global Atmosphere*, R. Mason and N. Pirrone, Eds. Springer US, 2009, pp. 427–457.
[276] P. A. Ariya, K. Peterson, G. Snider, and M. Amyot, “Mercury chemical transformations in the gas, aqueous and heterogeneous phases: state-of-the-art science and uncertainties,” in in *Mercury Fate and Transport in the Global Atmosphere*, R. Mason and N. Pirrone, Eds. Springer US, 2009, pp. 459–501.
[277] R. Harris, C. Pollman, D. Hutchinson, W. Landing, D. Axelrad, S. L. Morey, D. Dukhovskoy, and K. Vijayaraghavan, “A screening model analysis of mercury sources, fate and bioaccumulation in the Gulf of Mexico,” *Environ. Res.*, vol. 119, pp. 53–63, Nov. 2012.
[278] P. Grandjean and K. T. Herz, “Methylmercury and Brain Development: Imprecision and Underestimation of Developmental Neurotoxicity in Humans,” *Mt. Sinai J. Med. J. Transl. Pers. Med.*, vol. 78, no. 1, pp. 107–118, 2011.
[279] United Nations Environmental Program, “Report of the intergovernmental negotiating committee to prepare a global legally binding instrument on mercury on the work of its fifth session,” Geneva, Switzerland, Mar. 2013.
[280] N. Nuttall, “Minamata Convention Agreed by Nations.” United Nations Enviromental Program, 19-Jan-2013.
[281] J. Z. James, D. Lucas, and C. P. Koshland, “Elemental mercury vapor interaction with individual gold nanorods,” *Analyst*, 2013.
[282] V. M. Mirsky, M. Vasjari, I. Novotny, V. Rehacek, V. Tvarozek, and O. S. Wolfbeis, “Self-assembled monolayers as selective filters for chemical sensors,” *Nanotechnology*, vol. 13, no. 2, p. 175, 2002.

Appendix A Spectral shifts of fiber optic sensors

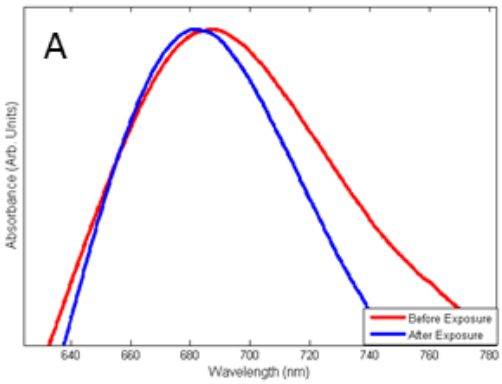

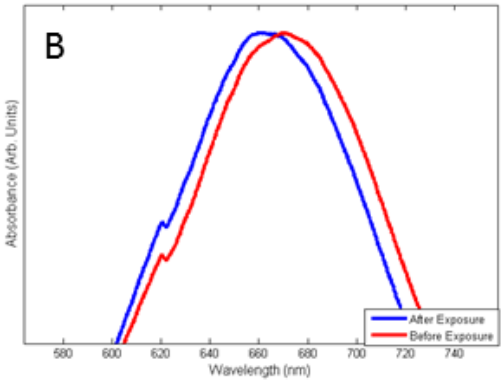

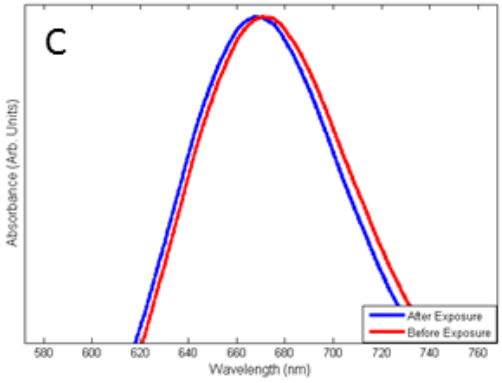

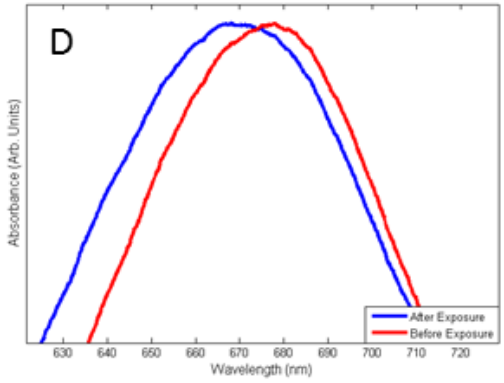

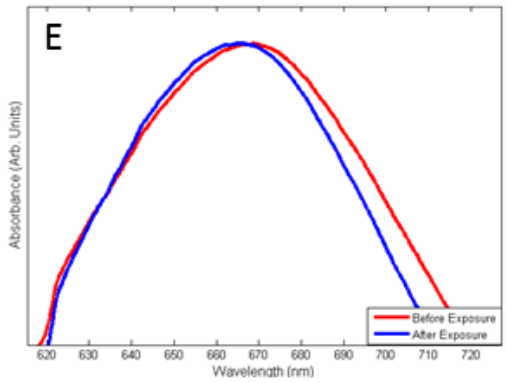

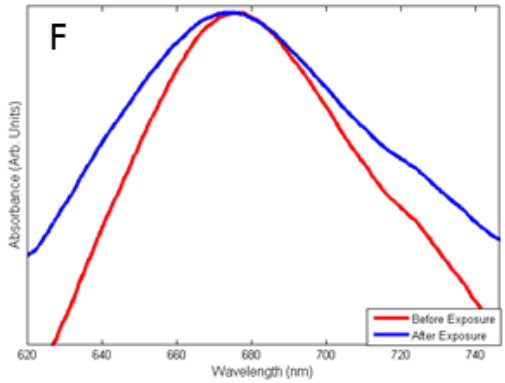

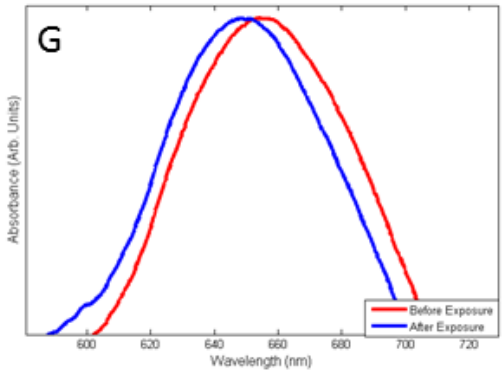

A) Sensor 1 exposed to 2µg/m^3
B) Sensor 2 exposed to 8µg/m^3
C) Sensor 3 exposed to 1µg/m^3
D) Sensor 4 exposed to 80µg/m^3
E) Sensor 5 exposed to 26µg/m^3
F) Sensor 6 exposed to 27µg/m^3
G) Sensor 7 exposed to 54µg/m^3

Appendix B Matlab functions for processing absorbance data and fitting kinetic/diffusion models

Appendix B.1 Absorbance Processing Program

Using Spectra Suite File Data

```
fstart='lbl2x10nm00000.txt';        % Initial File Name
filesend=5864;                      % Last File Number

spectra_out=[50:1000:6500, 6500];   %Spectra files to output

peak_estimate=545;                  % Estimate of the peak

%B is an empty matrix to input files into, srt and stop remove header and
%footer from spectra files
B=zeros(1,filesend+1);
lB=B;
clocktime=B;
 %new spec
srt=20;
stp=1000;

% old spec
%srt=1000;
%stp=3500;

%pick out which position to change.
decimal_loc=strfind(fstart,'.');
zeroes_locs=strfind(fstart,'0');
ones_loc=decimal_loc-1;
tens_loc=decimal_loc-2;
hundred_loc=decimal_loc-3;
thous_loc=decimal_loc-4;
thous_check=any(thous_loc==zeroes_locs);
xthous_loc=decimal_loc-5;
xthous_check=any(xthous_loc==zeroes_locs);


for fnumber=0:filesend
    %determining the portion of the file number to sub in
```

```
    xx=mod(fnumber,10000);
    x=mod(fnumber,1000);
    y=mod(x,100);
    z=mod(y,10);
    x5=(fnumber-xx)/10000;
    x4=(xx-x)/1000;
    x3=(x-y)/100;
    x2=(y-z)/10;
    x1=z;

    %this is subbing in
            fname=fstart;
            if xthous_check
                fname(xthous_loc)=int2str(x5);
            end
            if thous_check
            fname(thous_loc)=int2str(x4);
            end
            fname(hundred_loc)=int2str(x3);
            fname(tens_loc)=int2str(x2);
            fname(ones_loc)=int2str(x1);




rang=[srt 0 stp 1];
A=dlmread(fname,'\t',rang);


            %TURNING A into a X AND Y matricies
%NOTES on pulling data from "A" matrix
%This seems to be where the most trouble is had in the program.
%Of particular concern are maxiuma that are higher then the Longitudinal
%Peak.

% For the QR 9000 spectrometer
Amax_estimate=(peak_estimate-200.76)/.8;
pHWHM=55;

%For the H 4500 spectrometer
%Amax_estimate=(peak_estimate-458.06)/.26;
%pHWHM=200;
```

```
Amaxin=round(Amax_estimate);

%

X=A(Amaxin-pHWHM:Amaxin+pHWHM,1);
Y=A(Amaxin-pHWHM:Amaxin+pHWHM,2);
%applying a 6th order scaled polynomial as a check
%[P,s,mu]=polyfit(X,Y,6);
%Ypoly=polyval(P,X,s,mu);

%[~, peakindex]=max(Ypoly);
%lorenze fit
[Yprime,para,~,~]=lorentzfit(X,Y,[],[],'3c');
Ypoly=Yprime;
%The following section of the code outputs the raw spectrum and the
%polyfit at times selected
abcx=fnumber==spectra_out;
if any(abcx)
    figure
    plot(A(:,1),A(:,2),X,Ypoly,[para(2) para(2)],[0,2],'k');
    xlabel('Wavelength')
    ylabel('Absorbance')
    legend('Orginal Spectrum','Scaled Polyfit')
    test_label=int2str(fnumber);
    len=length(test_label);
    abcx='Spectrum and Fit at 00000 ';
    abcx((25+1-len):25)=test_label;
    title(abcx);
end


%B(1,fnumber+1)=X(peakindex);
lB(1,fnumber+1)=para(2);
B(1,fnumber+1)=max(Ypoly);
%finding time
fid=fopen(fname);
AA=fscanf(fid,'%[^P]');
hours=str2double(AA(80:81));
minute=str2double(AA(83:84));
sec=str2double(AA(86:87));
```

```
fclose all;

clocktime(1,fnumber+1)=hours/24+minute/(24*60)+sec/(24*60*60);


end
time=(clocktime-clocktime(1)).*(24*60);


figure
%plot(time,B,'x',time, lB,'r')
plot(time,lB)
xlabel('Time (min)')
ylabel('Peak Location (nm)')
```

Deals with temperature data from usb thermocouple

```
TempFileName='SimpleT.txt';

    time_diff=0;  %put this in decimal minutes




AA=importdata(TempFileName);

TempTime=(AA(:,1)-AA(1,1)).*60.*24+time_diff;
Temp=AA(:,2);
ptime=time;
peaks=lB;
figure
[AX, h1, h2]=plotyy(ptime,peaks,TempTime,Temp);

xlabel('Time','FontSize', 14)
set(get(AX(1),'Ylabel'),'String','Peak Position','Fontsize',14)
set(get(AX(2),'Ylabel'),'String','Temperature','Fontsize',14,'color','r')
set(AX(2),'ycolor','r')
set(h2,'LineStyle','none','Marker','.')
set(h2,'color','r')
set(h1,'LineStyle','none','Marker','x')
set(h1,'color','b')
```

```
Fits Langmuir isotherm to exposure data

%collect points around each Hg event
Fstr=3980;
Fhg=4574;
Fend=5860;
Conc=20;   %in ug/m3
peaks=lB;
%get the vectors for those points
Tx=time(Fhg:Fend);

InitialVal=mean(peaks(Fstr:Fhg));
FinalVal=mean(peaks((Fend-20):Fend));
Py=(peaks(Fhg:Fend)-InitialVal)./(FinalVal-InitialVal);

[Lresults, ~]=langmuirFit(Tx,Py);


ka=(Lresults.a*Lresults.b)/Conc     % adsorption constant
kd=Lresults.b-Lresults.a*Lresults.b  % desorption constant
```

Sips Isotherm

```
[Sresults,~]=sipsFit(Tx,Py,Conc)
```

Kinetic models

first order model

```
[FKresults,~]=Lfirstorder(Tx,Py);
%values
[SKresults, ~]=PsecondOfit(Tx,Py,Conc);
% Elovich
[Eresults,~]=Elovich(Tx,Py);
%nth Order
[Nthresults,~]=NthOrder(Tx,Py);
```

Diffusion Models

```
%film diffusion
[FDresults,~]=IdiffFit(Tx,Py);
%double esponential
[DEresults,~]=Dexp(Tx,Py);
```

Plots the Langmuir Fit back on the whole data set

```
figure
h1=line(time, lB);
h2=line( time(Fhg:Fend), (FinalVal-
InitialVal)*feval(Lresults,time(Fhg:Fend))+InitialVal);
h3=line(time(Fstr:Fhg),InitialVal.*ones(Fhg-Fstr+1));
set(h1,'LineStyle','none','Marker','x')
set(h2,'color',[1 0 0], 'LineWidth', 3)
set(h3,'color','r','Linewidth',2)

xlabel('Time (min)')
ylabel('Peak Location (nm)')
legend('Measured Peaks','Langmuir Isotherm')
%
```

This portion of the code deals finding the shift rate during the linear shift portion

```
figure
plot(time,peaks,'.')

hold
%using a 2nm shift from the initial value
iv=mean(peaks(Fstr:Fhg));
ivL1=iv-2;

satI=find(peaks(Fhg:Fend)<ivL1,1,'first')+Fhg;

C2nm=polyfit(time(Fhg:satI),peaks(Fhg:satI),1);

h1=line(time(Fhg:satI+30), polyval(C2nm,time(Fhg:satI+30)));
set(h1,'color',[1 0 0 ])
```

Based on a x% change from the Langmuir fit

```
%x=.8;

%satI=find(exp(Lresults.b.*(time-Lresults.c))<x,1,'first');



%CL=polyfit(time(Fhg:satI),B(Fhg:satI),1)
%h2=line(time(Fhg:satI), polyval(C1nm,time(Fhg:satI)));
%set(h2,'color',[0 1 0 ])

CL=-Lresults.a*Lresults.b*(InitialVal-FinalVal);
Io=InitialVal-CL*time(Fhg);
h2=line(time(Fhg:satI+30),CL.*time(Fhg:satI+30)+Io);

set(h2,'color',[0 1 0 ])
```

Finishing the plots

```
xlabel('Time (min)')
ylabel('Peak Location (nm)')
str1=sprintf('Measured Peaks');
str2=sprintf('Line 2nm Shift C=%g', C2nm(1));
str3=sprintf('Line from of Langmuir fit C=%g',  CL(1));

legend(str1,str2,str3)

hold
```

Published with MATLAB® R2012b

Appendix B.2 Function to apply a Langmuir Fit

```
function [fitresult, gof] = langmuirFit(x1, y1)

%CREATEFIT(X1,Y1)
%  Create a fit.
%
%  Data for 'untitled fit 1' fit:
%      X Input : x1
%      Y Output: y1
```

```
%  Output:
%      fitresult : a fit object representing the fit.
%      gof : structure with goodness-of fit info.
%
%  See also FIT, CFIT, SFIT.

%  Auto-generated by MATLAB on 21-Aug-2012 18:17:22
```

```
 [xData, yData] = prepareCurveData( x1, y1 );
cg=x1(1);
% Set up fittype and options.
ft = fittype( 'a*(1-exp(-b*(x-c)))', 'independent', 'x', 'dependent', 'y' );
opts = fitoptions( ft );
opts.Display = 'Off';
opts.Lower = [0 0 cg-1.5];
opts.StartPoint = [0.2 0.0318328463774207 cg];
opts.Upper = [1 10 cg+1.5];

% Fit model to data.
[fitresult, gof] = fit( xData, yData, ft, opts );

% Plot fit with data.
figure( 'Name', 'untitled fit 1' );
h = plot( fitresult, xData, yData );
LangEq = sprintf('Langmuir Isotherm:\n%g*(1-exp(-%2.4f*(t-%2.2f))',...
    [fitresult.a fitresult.b fitresult.c]);
LEG=legend( h, 'Peaks', LangEq, 'Location', 'NorthEast' );
set(LEG,'FontSize',10)
% Label axes
xlabel( 'Time (min)' );
ylabel( '%Shift' );


uistri=sprintf('R^2=%g', gof.rsquare);
uicontrol('Style','text','Position',[400 80 100 15],...
          'String',uistri);

grid on
```

Appendix B.3 Function for Sips/Freundlich Isotherm Fit

```
function [fitresult, gof] = sipsFit(X, Y, conc)

%CREATEFIT(X,Y)
%  Create a fit.
%
%  Data for 'Sips (Freundlich/Langmuir)' fit:
%      X Input : X
%      Y Output: Y
%  Output:
%      fitresult : a fit object representing the fit.
%      gof : structure with goodness-of fit info.
%
%  See also FIT, CFIT, SFIT.

%  Auto-generated by MATLAB on 08-Oct-2012 21:43:53

 [xData, yData] = prepareCurveData( X, Y );
cg=X(1);
% Set up fittype and options.
fitstring=sprintf('ka*%g^n/(ka*%g^n+kd)*(1-exp(-(ka*%g^n+kd)*(x-
xo)))',conc,conc,conc);
ft = fittype( fitstring, 'independent', 'x', 'dependent', 'y' );
opts = fitoptions( ft );
opts.Display = 'Off';
opts.Lower = [ 0 0 0 cg-1];
opts.StartPoint = [ 0.445586200710899 0.646313010111265 0.709364830858073
cg];
opts.Upper = [ Inf Inf Inf cg+1];

% Fit model to data.
[fitresult, gof] = fit( xData, yData, ft, opts );

% Plot fit with data.
figure( 'Name', 'Sips (Freundlich/Langmuir)' );
h = plot( fitresult, xData, yData );
LangEq = sprintf('Sips Isotherm: \n ka=%g \n kd=%g \n n=%g',...
    fitresult.ka, fitresult.kd, fitresult.n);
LEG=legend( h, 'Peaks', LangEq, 'Location', 'NorthEast' );
set(LEG,'FontSize',10)
```

```
% Label axes
xlabel( 'Time (min)' );
ylabel( '%Shift' );


uistri=sprintf('R^2=%g', gof.rsquare);
uicontrol('Style','text','Position',[400 80 100 15],...
          'String',uistri);
```

Published with MATLAB® R2012b

Appendix B.4 Function for First Order Fit

```
function [fitresult, gof] = Lfirstorder(X, Y)
```

```
%CREATEFIT(X,Y)
%  Create a fit.
%
%  Data for 'Lagergren 1st order' fit:
%      X Input : X
%      Y Output: Y
%  Output:
%      fitresult : a fit object representing the fit.
%      gof : structure with goodness-of fit info.
%
%  See also FIT, CFIT, SFIT.

%  Auto-generated by MATLAB on 09-Oct-2012 11:12:36
```

```
 [xData, yData] = prepareCurveData( X, Y );

% Set up fittype and options.
cg=X(1);
ft = fittype( '1-exp(k*(x-xo))', 'independent', 'x', 'dependent', 'y' );
opts = fitoptions( ft );
opts.Display = 'Off';
opts.Lower = [-Inf cg-1];
opts.StartPoint = [0.622055131485066 cg];
opts.Upper = [Inf cg+1];

% Fit model to data.
```

```
[fitresult, gof] = fit( xData, yData, ft, opts );

% Plot fit with data.
figure( 'Name', 'Lagergren 1st order' );
h = plot( fitresult, xData, yData );
LangEq = sprintf('First Order:\n1-exp(%g*(t-to)',fitresult.k);
legend( h, 'Y vs. X', LangEq, 'Location', 'NorthEast' );
% Label axes
xlabel( 'X' );
ylabel( 'Y' );
grid on

uistri=sprintf('R^2=%g', gof.rsquare);
uicontrol('Style','text','Position',[400 80 100 15],...
          'String',uistri);
```

Published with MATLAB® R2012b

Appendix B.5 Second Order Fit Function

```
function [fitresult, gof] = PsecondOfit(X, Y, conc)

%CREATEFIT(X,Y)
%  Create a fit.
%
%  Data for 'Psuedo Psuedo 2nd Order' fit:
%      X Input : X
%      Y Output: Y
%  Output:
%      fitresult : a fit object representing the fit.
%      gof : structure with goodness-of fit info.
%
%  See also FIT, CFIT, SFIT.

%  Auto-generated by MATLAB on 10-Oct-2012 20:26:10

[xData, yData] = prepareCurveData( X, Y );
cg=X(1);
% Set up fittype and options.
fitstring=sprintf('1-1/(1+ka*%g^n*(x-to))',conc);
ft = fittype(fitstring , 'independent', 'x', 'dependent', 'y' );
opts = fitoptions( ft );
opts.Display = 'Off';
```

```
opts.Lower = [-Inf, 0,cg-1];
opts.StartPoint = [0.513249539867053 .5 cg];
opts.Upper = [Inf Inf cg+1];

% Fit model to data.
[fitresult, gof] = fit( xData, yData, ft, opts );

% Plot fit with data.
figure( 'Name', 'Psuedo Psuedo 2nd Order' );
h = plot( fitresult, xData, yData );
LangEq = sprintf('Psuedo 2nd Order:\n 1-1/(1+%g*%g^(%g)*(t-
%g))',fitresult.ka,conc,fitresult.n,fitresult.to);
legend( h, 'Peaks', LangEq, 'Location', 'NorthEast' );
% Label axes
xlabel( 'X' );
ylabel( 'Y' );
grid on

uistri=sprintf('R^2=%g', gof.rsquare);
uicontrol('Style','text','Position',[400 80 100 15],...
          'String',uistri);
```

Published with MATLAB® R2012b

Appendix B.6 Nth Order Fit

```
function [fitresult, gof] = NthOrder(Tx, Py)

%CREATEFIT(TX,PY)
%  Create a fit.
%
%  Data for 'Nth Order' fit:
%      X Input : Tx
%      Y Output: Py
%  Output:
%      fitresult : a fit object representing the fit.
%      gof : structure with goodness-of fit info.
%
%  See also FIT, CFIT, SFIT.

%  Auto-generated by MATLAB on 14-Oct-2012 21:28:31
```

```
 [xData, yData] = prepareCurveData( Tx, Py );
cg=Tx(1);
% Set up fittype and options.
ft = fittype( '1-1/((n-1)*k*(x-to)+1)^(1/n)', 'independent', 'x',
'dependent', 'y' );
opts = fitoptions( ft );
opts.Display = 'Off';
opts.Lower = [0 1 cg-3];
opts.StartPoint = [0.649115474956452 1.5 cg-1];
opts.Upper = [Inf Inf cg-.01];

% Fit model to data.
[fitresult, gof] = fit( xData, yData, ft, opts );

% Plot fit with data.
figure( 'Name', 'Nth Order' );
h = plot( fitresult, xData, yData );
langEq=sprintf('%gth Order: \n 1-1/[(%g-1)*%g*(t-%g)+1]^(^1^/^n^)',...
    fitresult.n,fitresult.n,fitresult.k,fitresult.to);
legend( h, 'Peaks', langEq, 'Location', 'NorthEast' );
% Label axes
xlabel( 'Tx' );
ylabel( 'Py' );
grid on

uistri=sprintf('R^2=%g', gof.rsquare);
uicontrol('Style','text','Position',[400 80 100 15],...
          'String',uistri);
```

Published with MATLAB® R2012b

Appendix B.7 Film Diffusion Fit Function

```
function [fitresult, gof] = IdiffFit(Tx, Py)

%CREATEFIT(TX,PY)
%  Create a fit.
%
%  Data for 'Film Diff' fit:
%      X Input : Tx
%      Y Output: Py
%  Output:
```

```
%      fitresult : a fit object representing the fit.
%      gof : structure with goodness-of fit info.
%
%  See also FIT, CFIT, SFIT.

%  Auto-generated by MATLAB on 14-Oct-2012 15:38:07
```

```
 [xData, yData] = prepareCurveData( Tx, Py );

% Set up fittype and options.
cg=Tx(1);
ft = fittype( 'k*(x-xo)^.5', 'independent', 'x', 'dependent', 'y' );
opts = fitoptions( ft );
opts.Display = 'Off';
opts.Lower = [0 cg-3];
opts.StartPoint = [0.0844358455109103 cg-2];
opts.Upper = [Inf cg-.1];

% Fit model to data.
[fitresult, gof] = fit( xData, yData, ft, opts );

% Plot fit with data.
figure( 'Name', 'Film Diff' );
h = plot( fitresult, xData, yData );
LangEq = sprintf('Film Diffusion:\n %g*sqrt(t-%g)',fitresult.k,fitresult.xo);
legend( h, 'Peaks', LangEq, 'Location', 'NorthEast' );
% Label axes
xlabel( 'Tx' );
ylabel( 'Py' );
grid on

uistri=sprintf('R^2=%g', gof.rsquare);
uicontrol('Style','text','Position',[400 80 100 15],...
          'String',uistri);
```

Published with MATLAB® R2012b

Appendix B.8 Double Exponential Fit Function

```
function [fitresult, gof] = Dexp(Tx, Py)
```

```
%CREATEFIT(TX,PY)
%  Create a fit.
%
%  Data for 'Double Exp' fit:
%      X Input : Tx
%      Y Output: Py
%  Output:
%      fitresult : a fit object representing the fit.
%      gof : structure with goodness-of fit info.
%
%  See also FIT, CFIT, SFIT.

%  Auto-generated by MATLAB on 14-Oct-2012 21:07:51
```

```
 [xData, yData] = prepareCurveData( Tx, Py );
cg=Tx(1);
% Set up fittype and options.
ft = fittype( '1-A*exp(-k1*(x-to))-B*exp(-k2*(x-to))', 'independent', 'x',
'dependent', 'y' );
opts = fitoptions( ft );
opts.Display = 'Off';
opts.Lower = [0 0 0 0 cg-1];
opts.StartPoint = [0.123318934835166 0.183907788282417 0.239952525664903
0.41726706908437 cg];
opts.Upper = [Inf Inf Inf Inf cg+2];

% Fit model to data.
[fitresult, gof] = fit( xData, yData, ft, opts );

% Plot fit with data.
figure( 'Name', 'Double Exp' );
h = plot( fitresult, xData, yData );
LangEq=sprintf('DoubleExponential: \n 1-%g*exp[-%g(x-%g)]-%g*exp[-%g(x-
%g)]',...

fitresult.A,fitresult.k1,fitresult.to,fitresult.B,fitresult.k2,fitresult.to);
legend( h, 'Peaks', LangEq, 'Location', 'NorthEast' );
% Label axes
xlabel( 'Tx' );
ylabel( 'Py' );
grid on
```

```
uistri=sprintf('R^2=%g', gof.rsquare);
uicontrol('Style','text','Position',[400 80 100 15],...
          'String',uistri);
```

Published with MATLAB® R2012b

Appendix B.9 Elovich Model

```
function [fitresult, gof] = Elovich(Tx, Py)
```

```
%CREATEFIT(TX,PY)
%  Create a fit.
%
%  Data for 'Elovich' fit:
%      X Input : Tx
%      Y Output: Py
%  Output:
%      fitresult : a fit object representing the fit.
%      gof : structure with goodness-of fit info.
%
%  See also FIT, CFIT, SFIT.

%  Auto-generated by MATLAB on 14-Oct-2012 15:34:47
```

```
 [xData, yData] = prepareCurveData( Tx, Py );
cg=Tx(1);
% Set up fittype and options.
ft = fittype( '1/B*log(A*B)+1/B*log(x-xo)', 'independent', 'x', 'dependent',
'y' );
opts = fitoptions( ft );
opts.Display = 'Off';
opts.Lower = [0 0 cg-3];
opts.StartPoint = [0.528533135506213 0.165648729499781 cg-2];
opts.Upper = [Inf Inf cg-.1];

% Fit model to data.
[fitresult, gof] = fit( xData, yData, ft, opts );

% Plot fit with data.
figure( 'Name', 'Elovich' );
LangEq = sprintf('Elovich:\n 1/%g*ln(%g*%g)+1/%g*ln(1/(t-%g))',...
    fitresult.B,fitresult.A,fitresult.B,fitresult.B, fitresult.xo);
```

```
h = plot( fitresult, xData, yData );
legend( h, 'Peaks', LangEq, 'Location', 'NorthEast' );
% Label axes
xlabel( 'Tx' );
ylabel( 'Py' );
grid on


uistri=sprintf('R^2=%g', gof.rsquare);
uicontrol('Style','text','Position',[400 80 100 15],...
          'String',uistri);
```

Published with MATLAB® R2012b

Appendix B.10 Elovich Model Fit Function

```
function [fitresult, gof] = Elovich(Tx, Py)

%CREATEFIT(TX,PY)
%  Create a fit.
%
%  Data for 'Elovich' fit:
%      X Input : Tx
%      Y Output: Py
%  Output:
%      fitresult : a fit object representing the fit.
%      gof : structure with goodness-of fit info.
%
%  See also FIT, CFIT, SFIT.

%  Auto-generated by MATLAB on 14-Oct-2012 15:34:47

 [xData, yData] = prepareCurveData( Tx, Py );
cg=Tx(1);
% Set up fittype and options.
ft = fittype( '1/B*log(A*B)+1/B*log(x-xo)', 'independent', 'x', 'dependent',
'y' );
opts = fitoptions( ft );
opts.Display = 'Off';
opts.Lower = [0 0 cg-3];
opts.StartPoint = [0.528533135506213 0.165648729499781 cg-2];
opts.Upper = [Inf Inf cg-.1];
```

```
% Fit model to data.
[fitresult, gof] = fit( xData, yData, ft, opts );

% Plot fit with data.
figure( 'Name', 'Elovich' );
LangEq = sprintf('Elovich:\n 1/%g*ln(%g*%g)+1/%g*ln(1/(t-%g))',...
    fitresult.B,fitresult.A,fitresult.B,fitresult.B, fitresult.xo);
h = plot( fitresult, xData, yData );
legend( h, 'Peaks', LangEq, 'Location', 'NorthEast' );
% Label axes
xlabel( 'Tx' );
ylabel( 'Py' );
grid on


uistri=sprintf('R^2=%g', gof.rsquare);
uicontrol('Style','text','Position',[400 80 100 15],...
          'String',uistri);
```

Published with MATLAB® R2012b

Appendix B.11 Lorentz (Cauchy Distribution) Function Fit

```
function [fitresult, gof] = LorenzFit(X, Y)

%CREATEFIT(X,Y)
%  Create a fit.
%
%  Data for 'Lorenzian Fit' fit:
%      X Input : X
%      Y Output: Y
%  Output:
%      fitresult : a fit object representing the fit.
%      gof : structure with goodness-of fit info.
%
%  See also FIT, CFIT, SFIT.

%  Auto-generated by MATLAB on 01-Oct-2012 14:17:37

 [xData, yData] = prepareCurveData( X, Y );

% Set up fittype and options.
ft = fittype( 'a+b/(1+(x-c)^2/d)', 'independent', 'x', 'dependent', 'y' );
```

```
opts = fitoptions( ft );
opts.Display = 'Off';
opts.Lower = [0 0 500 -Inf];
opts.Robust = 'Bisquare';
opts.StartPoint = [0.4456 0.6463 527 0.754686681982361];
opts.Upper = [0.06 10 600 Inf];

% Fit model to data.
[fitresult, gof] = fit( xData, yData, ft, opts );

% Plot fit with data.
%figure( 'Name', 'Lorenzian Fit' );
%h = plot( fitresult, xData, yData );
%legend( h, 'Y vs. X', 'Lorenzian Fit', 'Location', 'NorthEast' );
% Label axes
%xlabel( 'X' );
%ylabel( 'Y' );
%grid on.
```

Published with MATLAB® R2012b

Appendix C Matlab Functions for the Modeling of Optical Absorbance using Mie and Gans Dipole Approximations

Appendix C.1 Mie Dipole Approximation

```
function [ ext ] = Mie_DP_NS( Y,r,T,Hg )
%Calculates the aprox of the absorbance for a nanosphere from Dipole Mie
%aprox.
%   input is the wavelenth Y and radius of the particle r and T the
%   temperature in Centigrad
%   output is the extention cross section
%  makes use of a nested function for the medium dielectric and matrial
dielectirc

c=3e8;

    %em=Ciddor_n(Y,T,101325,0,450);
    em=3.3;
```

```
    [e11,e12]=Gold_index(Y);

    [e21,e22]=Drude_Gold_index(Y,T,r);

    [e13,e23]=Merc_index(Y);

    G=.7;
    H=.9;

    e01=e11*G+e21*(1-G);
    e02=(e12)*H+e22*(1-H);

    e1=e01*(1-Hg)+e13*Hg;
    e2=e02*(1-Hg)+e23*Hg;

    V=4/3*(r/10^9)^3;

    % this section adds a little peiece to account for volumeteric
    % expansion
    vec=4.26E-5;        %aprox volume expansion coefficient
    V=(1+vec*(T-25))*V;


    w=2*pi*c/(Y/10^9);

    ext=9*(w/c)*em^1.5*V*(e2)/((e1+2*em)^2+e2^2);



end
```

Published with MATLAB® R2012b

Appendix C.2 Gans Dipole Approximation

```
function [ ext ] = GANS_DP_NR( Y, D, L ,Hg)
%Calculates the aprox of the absorbance for a nanorod from Dipole Gans
%aprox.
%   input is the wavelenth Y and Diameter and Length of the particle
%   output is the extention cross section
%  makes use of a nested function for the medium dielectric and matrial
```

```
dielectirc

T=25;
RH=0;


r=D/2;
N=5E17;  % very rough estimate of # of particles per m3
waveL=Y/10^9;


    %nair=Ciddor_n(Y,T,101325,RH,450);
    %eair=nair^2;
    %nFO=FO_index(Y,T);
    %eFO=nFO^2;
    %nliq=Liquid_n(Y,T,2);
    %em=.5*eFO+.5*eair;
    em=3.3;
   % em=Emedium(Y,T,D/2,f);

   [e11,e21]=Drude_Gold_index(Y,T,L);
   [e12,e22]=Gold_index(Y);

   [e13,e23]=Merc_index(Y);

   e01=[(e12+e11)/2,e12,e12];
   e02=[(e21+e22)/2,e22,e22];

   e1=e01*(1-Hg)+e13*Hg;
   e2=e02*(1-Hg)+e23*Hg;


    V=4/3*(r/10^9)^3+(L/10^9)*pi*(r/10^9)^2;

        % this section adds a little peiece to account for volumeteric
        % expansion
        %vec=4.26E-5;        %aprox volume expansion coefficient
        %V=(1+vec*(T-25))*V;



    ep=sqrt(1-(D/L)^2);
```

```
    Pa=(1-ep^2)/ep^2*(1/(2*ep)*log((1+ep)/(1-ep))-1);
    Pb=(1-Pa)/2;
    Pc=Pb;

    P=[Pa Pb  Pc];

    for n=1:3
        ext1(n)=2*pi*N*V*em^1.5/(3*waveL)*(((1/P(n)^2)*e2(n))/((e1(n)+(1-
P(n))/P(n)*em)^2+e2(n)^2));
    end
    ext=ext1(1)+ext1(2)+ext1(3);







end
```

Published with MATLAB® R2012b

Appendix C.3 Index of Refraction for Gold

```
function [ e1,e2 ] = Gold_index( Y )
%computes the dielectric functions of gold based on wavelength
%   Linear interpolation based on data from:Handbook of Optical Constants
(HOC)
%   Vol. 1 1985 and Vol 11 1991   E.D. Palik Ed.  Academic Pressic Inc.
London


% Input  is the wavelength of light in nm
% Ouput is the real and imaginary part of the dielectric function e1 and e2


%n=dlmread('optical properties of gold.txt','\t',[3 2 46 2]);
%k=dlmread('optical properties of gold.txt','\t',[3 3 46 3]);
%waveL=dlmread('optical properties of gold.txt','\t',[3 1 46 1]);

% Using data from Johnson and Christy
```

```
n=dlmread('Johnson and Christy optical properties of gold.txt','\t',[1 2 49
2]);
k=dlmread('Johnson and Christy optical properties of gold.txt','\t',[1 3 49
3]);
waveL=dlmread('Johnson and Christy optical properties of gold.txt','\t',[1 1
49 1]);

ni=interp1(waveL,n,Y);
ki=interp1(waveL,k,Y);

e1=ni^2-ki^2;
e2=2*ni*ki;



end
```

Published with MATLAB® R2012b

Appendix C.4 Index of Refraction of Air using Ciddor Model

```
function [ n ] = Ciddor_n( y, T, P, RH, CO2 )

%Calculates the exact air index of refaction based on the Ciddor Equation
%as described in emtoobox.nist.gov/Wavelength/Documentation and
%refrencing Philip E. Ciddor, "Refractive index of air: new equations for the
visible and near infrared," Appl. Opt. 35, 1566-1573 (1996)
%   INPUT
%    Temp in C breaks down for T<0   may be suspect for T>100
%    Pressure in Pa
%    RH   relative humididty
%    CO2   mole fraction of CO2 in PPM or umol/mol usually 450
%    y    wavelength in nm



% Constants for equation

w0=295.235;
w1=2.6422;
```

```
w2=-0.03238;
w3=0.004028;

k0=238.0185;
k1=5792105;
k2=57.362;
k3=167917;

a0=1.58123e-6;
a1=-2.9331e-10;
a2=1.1043e-10;

b0=5.707e-6;
b1=-2.051e-8;

c0=1.9898e-4;
c1=-2.376e-6;

d=1.83e-11;
e=-0.765e-8;

Pr1=101325;
Tr1=288.15;

Za=0.9995922115;

pvs=0.00985938;

R=8.314472;
Mv=0.018015;

S=1/(y/1000)^2;     %  converts the wavelength to micrometers and then S

T_k=T+273.15;

%Initial Result

ras=(10^-8)*((k1/(k0-S))+(k3/(k2-S)));
rvs=(1.022e-8)*(w0+w1*S+w2*S^2+w3*S^3);

%Accounting for CO2
```

```
Ma=0.0289635+(1.2011e-8)*(CO2-400);

raxs=ras*(1+(5.34e-7)*(CO2-450));

%Calculate the vapor mole fraction from RH%
```

```
%Table of constants for corrilation to RH
K1=1.16705214528E+03;
K2=-7.24213167032E+05;
K3=-1.70738469401E+01;
K4=1.20208247025E+04;
K5=-3.23255503223E+06;
K6=1.49151086135E+01;
K7=-4.82326573616E+03;
K8=4.05113405421E+05;
K9=-2.38555575678E-01;
K10=6.50175348448E+02;

omega=T_k+K9/(T_k-K10);
A=omega^2+K1*omega+K2;
B=K3*omega^2+K4*omega+K5;
C=K6*omega^2+K7*omega+K8;
X=-B+sqrt(B^2-4*A*C);

Psv=(10^6)*(2*C/X)^4;



alpha=1.00062;
beta=3.14e-8;
gamma=5.60e-7;

fpt=alpha+beta*P+gamma*T^2;
xv=(RH/100)*fpt*Psv/P;
```

```
%The influence of tempeature compressibility and density



Zm=1-(P/T_k)*(a0+a1*T+a2*T^2+(b0-b1*T)*xv+(c0+c1*T)^2)+((P/T)^2)*(d+e*xv^2);

paxs=Pr1*Ma/(Za*R*Tr1);
pv=xv*P*Mv/(Zm*R*T_k);
```

```
pa=(1-xv)*P*Ma/(Zm*R*T_k);

n=1+(pa/paxs)*raxs+(pv/pvs)*rvs;

end
```

Published with MATLAB® R2012b

Appendix C.5 Mercury Index of Refraction

```
function [ e1, e2 ] = Merc_index( Y )
%Computes the complex dilectirc of mercury
%  Utilizes data from 'Optical Properties of selected elements' J.H. Weaver
%  and H.P.R Frederikse  CRC Handbook 2012

%Y is wavelength in nm conversts to electron volts
eV=1240/Y;

n=dlmread('Mercury Data CRC.txt',' ',[0 1 83 1]);
k=dlmread('Mercury Data CRC.txt',' ',[0 2 83 2]);
eVolts=dlmread('Mercury Data CRC.txt',' ',[0 0 83 0]);

ni=interp1(eVolts,n,eV);
ki=interp1(eVolts,k,eV);

e1=ni^2-ki^2;
e2=2*ni*ki;

end
```

Published with MATLAB® R2012b

Appendix C.6 Index of Refraction for Silicon Dioxide

```
function [ n  ] = FO_index( Y,T)
%Finds the index of refraction of SiO2 based on wavelength and temp
%   Based on Sellmeier Equation
%   Information from Ghosh C and Endo M 'Temperature Dependent Sellmeier
%   Coefficients and Chromatic Dispersons' Journal of Lightwave Technoloigy
```

```
%   Vol 12 no 8  Aug 1994
%  Input is temperature in C and Wavelength in nm
%

y=Y/1000;    %convert to um

n2_1=(1.31552+0.690754E-5*T);
n2_2=((0.788404+0.235835E-4*T)*y^2)/(y^2-(0.0110199+.584758E-6*T));
n2_3=(0.91316+.548368E-6*T)*y^2/(y^2-100);
n2=n2_1+n2_2+n2_3;

n=sqrt(n2);


end
```

Published with MATLAB® R2012b

Appendix C.7 Drude Approximation for Size Confined Nanoparticles

```
function [ e1,e2 ] = Drude_Gold_index( Y, T ,R)
%Calculates the dielectric functions of gold based on the Drude Model
%   Some constants taken from Gupta et. al 2011

c=3E8; %speed of light
y=Y/10^9;
R=R/10^9;

w=2*pi*c/y ; %converting to angular frequency

T=T+273.15;
% Calculating the plasmon frequency
wpbulk=1.3659E16;  % bulk plasmon frequency

wpo=wpbulk/sqrt(3);    %frequency for small particles

alpha=1.42E-5;      %linear expansion coefficenct gold

T0=25+273.15;             %refrence temp of the bulk plasmon I think

wp=wpo/sqrt(1+3*alpha*(T-T0))*sqrt(3);
```

```
%Calculating the collision frequency

    Td=185;   %Debye temp   k
    o0=7.5757E7;   %conductivity  S/m
    gamma=.55;      % fermi scattering probbabiliy
    del=.77;        %fractional umklapp scattering
    kb=1.38e-23;        %boltzmann constant
    h=6.625E-34;        %Plank Constant
    Ef=8.86E-19;            %Fermi Energy  in J  =5.53eV
        %not sure about this
        me=9.10938E-31;   %mass of electron in kg
        pf=sqrt(2*Ef*me);
        vf=pf/me;

    e0=8.85418782E-12;      %permittivity of free space

    %fraction from electron/electron Lawerence Model
    wce=1/6*pi^4*gamma*del/h/Ef*((kb*T)^2+(h*w/4/pi^2)^2);

    %fraction from the electron phonon scattering Holstein model

    wcpc=wpbulk^2*e0/o0;   %constants out front
    numint=@(z) z.^4./(2.71828.^z-1);
    wcpn=1/10+(T/Td)^5*quadl(numint,0,T/Td);
    devint=@(z) z.^5./((2.71828.^z-1).*(1-2.71828.^(-z)));
    wcpd=quadl(devint,0,1);

    wcp=wcpc*wcpn/wcpd;

    % bulk collison frequency

    wcb=wcp+wce;

    %accounting for size effects
    wc=(wcb+vf/(R));

e1=1-wp^2/(w^2+wc^2);
e2=(wp^2*wc)/(w*(wc^2+w^2));

ext=1-wp^2/(w^2+1i*wc*w);
```

```
e1=real(ext);
e2=imag(ext);
end
```

Published with MATLAB® R2012b

Appendix D Mass transfer correlation Matlab functions

Appendix D.1 Impinging jet efficiency

```
function [ nu ] = Jet_eff( D,L,V )
%Calculates impinging jet efficiency
% Input is
% D     diamter mm
% L     height mm
% V     volumetric flow rate LPM

% Calculates the mass transfer coefficient (Based on Womac function)
Sh=Womac(D,L,V);

Df=1.4E-1;  % Diffusion coefficient of mercury in air cm2/s

hm=Sh*(Df/100000)/(D/1000);

nu=hm*(L/1000)^2/(V/60000)*100;


end
```

Published with MATLAB® R2012b

Appendix D.2 Martin Correlation

```
function [ G ] = imp_jet2v(DR,HD )
%Calculates the 'G' portion of the impinging flow corrilation
%   Does not check validity but 2<H/D<12 2.5<r/d<7.5

G=DR*(1-1.1*DR)/(1+0.1*(HD-6)*DR);

end
```

Published with MATLAB® R2012b

Appendix D.3 Womac Correlation

```
function [ Sh ] = Womac( D,L,V )
%Calculates the Sherwood Number for Air using Womac et al. correlation
%   Input is:
%       D   Diamter of jet  mm
%       L   Side Length     mm
%       V   Volumeteric Flow rate LPM
%Corrilation is valid for Height between 1.5D and 4D

%Constants
mu=1.59E-5; % m2/s vicousity of air
Dhg=1.4E-1;   % cm2/s diffusvity of mercury in air


Sc=mu/(Dhg/100^2);  %Schmidt number

%Flow Velocity
v=(V/60000)/(pi*(D/1000)^2/4);

%Reynolds number
ReD=v*(D/1000)/mu;

Ls=0.5*((.70711*L-1.9*D)+(0.5*L-1.9*D));

ReL=v*(Ls/1000)/mu;

Ar=pi*(1.9*D)^2/L^2;

C1=.785;
C2=.0257;

if Ar>1
   Ar=1;
end
if Ls<0
   C2=0;
end

Sh=(C1*ReD^.5*(L/D)*Ar+C2*ReL^.8*(L/Ls)*(1-Ar))*Sc^0.4;
end
```

Published with MATLAB® R2012b